NASA CR-2069

SPECTROSCOPIC MEASUREMENTS OF WATER VAPOR PLASMAS AT HIGH RESOLUTION — THE OPTICAL TRANSITION PROBABILITIES FOR OH($A^2\Sigma$ - $X^2\Pi$)

by Lothar Klein

Prepared by
GREYRAD CORPORATION
Princeton, N.J.
for Lewis Research Center
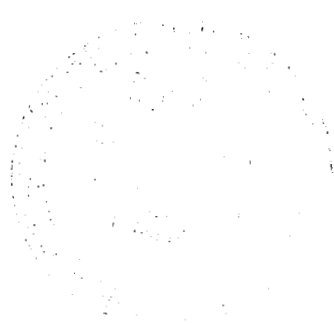
NATIONAL AERONAUTICS AND SPACE ADMINISTRATION • WASHINGTON, D. C. • AUGUST 1972

1. Report No. CR-2069	2. Government Accession No.	3. Recipient's C 0061207
4. Title and Subtitle SPECTROSCOPIC MEASUREMENTS OF WATER VAPOR PLASMAS AT HIGH RESOLUTION - THE OPTICAL TRANSITION PROBABILITIES FOR OH(A^{2}Σ - X^{2}Π)		5. Report Date August 1972
		6. Performing Organization Code
7. Author(s) Lothar Klein		8. Performing Organization Report No. None
9. Performing Organization Name and Address Greyrad Corporation Princeton, New Jersey		10. Work Unit No.
		11. Contract or Grant No. NAS 3-13424
12. Sponsoring Agency Name and Address National Aeronautics and Space Administration Washington, D.C. 20546		13. Type of Report and Period Covered Contractor Report
		14. Sponsoring Agency Code

15. Supplementary Notes

Project Manager, Erwin A. Lezberg, Physics and Chemistry Division, NASA Lewis Research Center, Cleveland, Ohio

16. Abstract

Emission and absorption spectra of water-vapor plasmas generated in a wall-stabilized arc at atmospheric pressure and 4 A current, and at 0.03 atm and 15 to 50 A, were measured at high spatial and spectral resolution. The gas temperature was determined from the shape of Doppler-broadened rotational lines of OH since the measured resolving power of the spectrometer was 400,000. The observed non-equilibrium population distributions over the energy levels of atoms are interpreted in terms of a theoretical state model for diffusion-controlled arc plasmas. Excellent correlation is achieved between the measured and the predicted occupation of the hydrogen energy levels. It is shown that the population distribution over the non-predissociating rotational-vibrational levels of the A^{2}Σ state of OH is close to an equilibrium distribution at the gas temperature, although the total density of this state is much higher than its equilibrium density. The reduced intensities of the rotational lines originating in these levels yielded Boltzmann plots that were strictly linear, but the slope did not correspond to the measured gas temperature. This is attributed to an exponential dependence of the transition moment on the rotational energy term. Appropriate correction factors were calculated and compared with theoretical predictions.

17. Key Words (Suggested by Author(s)) Hydroxyl ultraviolet bands; Transition probabilities; Line strengths; Spectroscopic temperature measurements; Non-equilibrium arc plasmas; Plasma spectroscopy	18. Distribution Statement Unclassified - unlimited		
19. Security Classif. (of this report) Unclassified	20. Security Classif. (of this page) Unclassified	21. No. of Pages 150	22. Price* $3.00

* For sale by the National Technical Information Service, Springfield, Virginia 22151

FOREWORD

The material presented in this report was included in the doctoral dissertation submitted by the author to the National University of Buenos Aires. His present address is the Plasma Spectrum Corporation, 287 Schenck Avenue, Great Neck, New York 11021.

The high-resolution plasma spectrometer was built in collaboration with H. J. Babrov, now at Indiana University at South Bend, while he and the author were with the Control Instrument Division of the Warner & Swasey Company. The grating drive was designed by W. L. Ronai and S. A. Dolin.

TABLE OF CONTENTS Page

SUMMARY

High-order spectroscopy has been applied to quantitative measurements of the spectra of water-vapor plasmas generated in a wall-stabilized arc. Because of the high spectral and spatial resolution achieved in end-on measurements, the emission and absorption coefficients pertaining to homogeneous arc regions were obtained directly from measured line spectra, leading to the occupation of the upper and the lower state for the transition. The electron density was derived from the profile of the Stark-broadened Balmer lines. The gas temperature was determined from the half-width of a Doppler-broadened rotational line of OH. The measured resolving power of the spectrometer was of the order of 400,000 in these measurements.

Significant departures from local thermodynamic equilibrium (LTE) were observed in a water-vapor arc at reduced pressure, and also in the peripheral zone of a low-current arc at atmospheric pressure with water vapor in an argon matrix. The "distribution temperature" characterizing the population distribution over highly excited energy levels of atoms is not only much lower than the electron temperature, but also substantially lower than the gas temperature. The noted departures from LTE occur because of the lack of equipartition of kinetic energy between the electrons and the heavy particles in the plasma, and because of diffusion of ground state neutrals from the arc periphery into the arc center and ambipolar diffusion of electrons and ions in the opposite direction. Based on these mechanisms, the various interaction processes in a hydrogen plasma are analyzed quantitatively on the microscopic level, and it is shown that the occupation of the excited energy states is predominantly determined by step-wise excitation induced by electron collision. Excellent agreement is obtained between the predicted and the measured number densities of the excited states of hydrogen in the water-vapor plasma at reduced pressure.

Ionization of atoms and dissociation of molecules such as OH occur by similar processes in the plasma, although the latter is dominated by heavy particle collision, and the relevant temperature is then the gas temperature. A close analogy exists between the population distribution over the auto-ionizing levels of oxygen and the predissociating levels of OH. The lower rotational-vibrational levels of the $A^2\Sigma$ excited electronic state of OH are effectively uncoupled from the dissociated state because of the step-wise excitation mechanism in conjunction with

the near-equality of the transition rates. The relative population distribution over these levels is therefore close to an equilibrium distribution at the gas temperature, even when the total density of the $A^2\Sigma$ state is orders of magnitude higher than its equilibrium density.

The reduced intensities of the non-predissociating rotational lines belonging to the various bands of the OH ($A^2\Sigma$ - $X^2\Pi$) system yielded Boltzmann plots that were strictly linear, although the slope did not correspond to the measured gas temperature. This is attributed to an exponential dependence of the transition moment on the rotational energy term. Appropiate correction factors were calculated and compared with theoretical predictions.

1. INTRODUCTION

The use of quantitative spectroscopy as a diagnostic tool in many areas of current interest has been obstructed by the paucity of accurate data on transition probabilities especially for molecular lines and by the lack of appropiate state models to characterize plasmas in absence of local thermodynamic equilibrium (LTE). The plasmas obtained in stabilized arcs at atmospheric pressure have been shown to be in LTE (1), and have been used in the past to determine transition probabilities for atomic lines. The initial concern of this investigation was to apply the same approach to molecular species that are still stable at arc temperatures, and a water vapor plasma generated in a wall-stabilized arc was used to determine the transition probabilities of rotational lines belonging to the ultraviolet bands of OH.

In LTE detailed balancing exists between the collisional processes in the plasma and the pertinent rates are much larger than for the equivalent radiative processes. Although the latter are not in detailed balance (i.e. photons can escape the plasma), the species concentration and the population distributions over energy levels in the plasma are then practically the same as in a system in complete thermodynamic equilibrium at the same temperature, pressure, and chemical composition at standard conditions. The occupation of energy levels can thus be calculated which makes LTE plasmas a convenient source for the experimental determination of transition probabilities, since the number density of emitters must be known in order to derive the optical transition probability from a spectroscopic measurement of the integrated line radiance.

In Section 2C we have calculated the equilibrium composition of a water vapor plasma at various pressures as a function of temperature. Provided the plasma is in LTE, it is then sufficient to determine experimentally the temperature of an isothermal plasma region in order to infer the transition probabilities from the intensities of the emitted optically-thin lines. In principle, a suitable "thermometer line" of known transition probability can be used to determine the plasma temperature. However, as argued in Section 2D (see also Ref. 1), the generalized Fowler-Milne method is preferable because over an extended temperature range a one-to-one correspondence is established between the measured line intensity and the calculated occupation of the upper energy level for the transition.

Because of the quantization of molecular energy states corresponding to nuclear motion, transitions between two electronic states of a molecule form an entire band system. Rigorously, a transition probability or a related quantity – oscillator strength or transition moment[*)] – can only be assigned to an individual rotational line. It is still useful, however, to consider the relationships between the transition moments for the rotational lines in a band, and the various bands in a system, which can be derived from theoretical assumptions and lead essentially to a factoring of the transition moment. The approach followed here was to determine first the transition probabilities for the individual rotational lines and then to use the concept of Franck-Condon factors ("band stengths") and Hoenl-London factors ("line strengths") as a first-order approximation for the representation of the measured data in terms of the <u>transition moments</u> by introducing appropiate correction factors.

[*)] square of the matrix element for electric dipole transition

A representation of rotational line intensities in terms of "band transition probabilities" or "band oscillator strengths" does not appear to be useful since a single frequency cannot be assigned to a band. The introduction of an average band frequency implies a weighting of the various rotational lines which leads to different values depending on the particular population distribution over the rotational energy levels.

Almost all previous measurements of the spectra of stabilized arcs were made by viewing the arc side-on. In order to obtain the spectral data pertaining to isothermal arc regions (radial zones for arcs of cylindrical symmetry), spatial scanning of the arc and an Abel inversion of the experimental lateral intensity profile are required. This is a viable approach when the integrated intensities of optically-thin lines are measured (see Section 4). Severe problems arise, however, in the interpretation of line absorptances and line shapes measured across spatial temperature gradients.

These difficulties are avoided by viewing the arc in the axial direction (end-on mode), since then an essentially homogeneous plasma sample is seen by the spectrometer, provided the arc axis is accurately aligned parallel to the optical axis of the system, and appropiate stops are used to limit the field of view and the aperture of the spectrometer. Even when extreme care has been exercised in setting-up the arc, a direct proof of correct arc alignment is best obtained by an actual measurement. In Section 3D we describe such an experiment which also demonstrates the relative ease with which information on line shapes can be obtained by high-resolution measurements in the end-on mode.

A scanning spectrometer was built whose optical characteristics match the constraints of the arc, and an echelle grating was used to achieve high spectral resolution at small apertures. The performance of the instrument is described

in some detail since high-order spectroscopy has apparently not been applied before to quantitative measurements of arc plasmas.

Provided the emission and absorption coefficients for an optically-thick line are invariant over the spectral bandpass (because of high spectral resolution) and along the line of sight of the spectrometer (because of high spatial resolution), the equation of radiative transfer yields a simple analytical solution, and the measured emission and absorption can be easily interpreted in terms of the emission and absorption coefficients within the plasma. The line profile for the emission coefficient (i.e. the optically thin line) can then be obtained from the measured line profile independent of any a-priori assumption regarding the broadening mechnism, and one can also determine the occupation of the upper and the lower energy level for the transition.

As shown theoretically in Section 2A and demonstrated experimentally in Section 5D this information can often be obtained by high-resolution emission measurements alone in lieu of an actual absorption measurement. This method is not to be confused with the check for self-absorption customarily used in plasma spectroscopy and based on calculating the Planck function at the electron temperature in order to estimate the absorptance from the peak intensity of the line. Our results for the Balmer lines demonstrate how misleading such a procedure can be if applied to non-equilibrium plasmas.

By measuring the line profile one can determine the broadening mechanisms, i.e. obtain information on the environment of the emitter. Thus we derived the kinetic temperature of the heavy particles in the plasma from the shape of the Doppler-broadened rotational lines. The shape of the hydrogen lines is determined predominantly by Stark broadening and can then be used to obtain the electron density in the plasma. In this work the shape of the Stark-broadened H_γ and H_δ lines as predicted by Griem's theory ($2-4$), has been directly verified

6

for electron densities as low as 6×10^{15} cm^{-3}. Moreover, the calculated shape of the line wings is probably also correct at electron densities which are still lower by an order of magnitude.

As the experimental program progressed, it became obvious that our initial optimism regarding the attainment of equilibrium in the arc, was ill-founded. Since the spectroscopic observables could not be correlated with the LTE model, the arc plasma can no longer be characterized by a few parameters - temperature, pressure, and chemical composition at standard conditions. We were faced essentially by a twofold problem: First we had to determine experimentally the plasma state, i.e. the concentration of the various species (molecules, atoms, ions) and their distribution over energy levels. Secondly, the different interaction processes in the plasma had to be analyzed in order to approximate the complex plasma state by a simplified state model and to elucidate the mechanisms bringing about the observed departures from equilibrium.

The refined diagnostic information made available by high-resolution measurements in emission and absorption - which might be largely redundant for LTE-plasmas - becomes important in the absence of equilibrium. If the optical transition probabilities for lines belonging to a certain species are known, the spectroscopic observables can be converted into the population distribution over energy levels for that species, without involving a-priori assumptions concerning the plasma state. The combined emission-absorption method permits one to extend the range of these measurements to the lower energy levels. In emission the same data can either not be obtained at all (metastable levels), or one has to resort to quantitative measurements in the vacuum ultraviolet which are notoriously difficult. But it is precisely the occupation of the lower energy levels which is often of crucial importance for the interpretation of the plasma state.

7

The population distribution over energy levels is conveniently expressed in terms of the occupation of energy states, for which we use the notation n*. Thus, if n(i) is the occupation of energy level i of statistical weight g(i):

$$n*(i) \quad \equiv \quad n(i)/g(i) \qquad (cm^{-3}) \qquad (1-1)$$

Numerically the occupation (also called population density or number density) is expressed in cm^{-3}. The representation of the population distribution in the form of a plot of log n*(i) vs. E_i[*] is here also called a "Boltzmann plot", but this does not imply that its slope is necessarily related to a temperature in the true, i.e. thermodynamic sense. In non-equilibrium situations, the "distribution temperature" introduced by formally equating the source function to the Planck function (Eq. 2-7), does not refer to any meaningful temperature, but is only a convenient parameter to characterize the population distribution between two energy levels.

As shown in this work, the velocity distribution of electrons and of heavy particles in arc plasmas is often still Maxwellian even when considerable departures from equilibrium occur, including a lack of equipartition of kinetic energy between free electrons and heavy particles. One can then properly speak of an electron temperature T_e and a gas temperature T_g. However, the author finds the widespread use of such expressions as excitation, rotational, or vibrational "temperatures" objectionable, because they invoke the wrong physical picture. If the departures from LTE are relatively mild (as, for instance, in the low-current arc at atmospheric pressure), the population distribution over some electronic levels will be approximately determined by T_e and equivalently over some rotational levels by T_g, but then the concept of "excitation temperature" or "rotational temperature" is redundant, at best.

---

[*] Our results are mostly expressed in terms of logarithms to base 10 ("log"), natural logarithms are designated by "ln".

If the departures from equilibrium are more severe (e.g. in the arc at reduced pressure), the "distribution temperatures" for energy levels corresponding to a particular degree of freedom are, in general, different for the various energy levels and also for the various species. In some cases the "distribution temperature" is practically constant over a range of energy levels, leading to a Boltzmann plot that is linear by sections. However, this appears to be only a spurious effect and is attributed to/specific relationship between the pertinent population and depopulation rates as discussed in Section 10B in connection with the observed linearity of the Boltzmann plot for predissociating rotational levels.

In order to illustrate better the practical application of our method we have described in some detail how the Boltzmann plots for hydrogen and oxygen were obtained. The experimental data for the various bands of OH were represented similarly by what we call here an "apparent Boltzmann plot", because the reduced intensity shown on the ordinate is not simply proportional to the occupation of the rotational energy level but contains also the - unknown - dependence of the transition moment on the rotational energy term. In Section 6D we discuss the functional form of this dependence and establish essentially an upper bound for its magnitude.

In the second part of this report the observed population distributions are interpreted in terms of a theoretical state model for the plasma. The basic concepts used in the theory of rate processes in plasmas are described in the literature (see e.g. Refs. 5, 6 and 8). Griem has used theoretical estimates to derive general criteria for the validity of LTE in plasmas (4, 7). For hydrogen plasmas, Bates et al. have obtained the general steady-state solution of the rate equations corresponding to the collisional-radiative model (8).

9

In the approach followed here we proceed by steps using the detailed
spectroscopic information available to establish a correlation between
theoretical deductions and experimental evidence. It is readily seen that
water vapor plasmas are eminently suited to study non-equilibrium effects.
Conclusions of general validity are derived using as representative examples
the two plasma regimes investigated: (a), a water vapor plasma in an argon
matrix generated in a low-current arc at atmospheric pressure, and (b), a
plasma of pure water vapor generated in an high-current arc at reduced pressure.

First, we attempt to simplify the complex plasma state by estimating the
relative importance of the various elementary processes by which transitions
between energy states occur. Hydrogen is chosen for these model calculations
because of the simplicity of its energy level scheme and because the relevant
rate coefficients are at least approximately known. If the ground state is
strongly overpopulated with respect to its occupation in equilibrium with free
electrons and ions, it is shown that the population and depopulation of energy
levels is determined predominantly by step-wise excitation induced by electron
collision. The occupation of energy levels falls off rapidly with increasing
principal quantum number which leads to progressively lower "distribution temp-
eratures". The electron temperature becomes then a rather elusive quantity.
(In a sense, this situation is just the opposite of what is predicted for the
collisional-radiative model). We then apply the step-wise excitation model
to the calculation of the occupation of the hydrogen energy levels in the
water vapor arc at reduced pressure.

The observed non-equilibrium distributions over the energy levels of oxygen
and of OH can also be explained, at least qualitatively, by essentially the

10

same model, although encounters with heavy particles are more effective than electron collisions in inducing transitions involving nuclear motion. The respective Boltzmann plots are similar because ionization of oxygen and dissociation of OH can both occur by an Auger process.

As shown by this study of non-equilibrium plasmas, a close analogy exists between ionization by electron collision and dissociation by heavy particle collision, and both processes are dominated by step-wise excitation. The absence of equilibrium between bound and ionized - or dissociated - states is then appropriately discussed in terms of the occupation of the last bound state. This concept is developed in Section 7 with reference to the ionization equilibrium. Since the Saha equation is only a specialized form of the general mass action equation, identical arguments apply also to the dissociation equilibrium.

The principle of detailed balancing or microscopic reversibility (9) applies rigorously to the rate coefficients for a particular process and its inverse, but not to the process itself. Thus, if the excitation rate for atoms or molecules in the electronic ground state, the recombination rate for an electron-ion pair, or the dissociation rate for a molecule such as OH, are smaller than the probability for a competing irreversible process - diffusion - the species concentration in an isothermal volume element of the plasma can deviate considerably from the equilibrium concentration. Based on the particulate nature of the plasma, we use gas-kinetic considerations to estimate the effect of diffusion processes and the lack of equipartition of kinetic energy between electrons and heavy particles.

2. THEORY

A. Emission-Absorption Measurements of Homogeneous Plasmas at High
   Spectral Resolution

If scattering can be disregarded, the change of intensity of a beam of
monochromatic light of wavelength λ incident on a thin layer of plasma of
thickness dx is given by the difference between the spontaneous emission
(emission coefficient ϵ_λ) and the net absorption[*] (net absorption coefficient $k_\lambda^\bullet$)
by the plasma:

$$dI_\lambda(x) \;=\; \epsilon_\lambda(x)\,dx \;-\; k_\lambda^\bullet(x)\,I_\lambda(x)\,dx \qquad (2\text{-}1)$$

Introducing the source function:

$$S_\lambda(x) \;=\; \epsilon_\lambda(x)/k_\lambda^\bullet(x) \qquad ,$$

Eq. 2-1, the equation of radiative transfer, can be written:

$$dI_\lambda(x) \;=\; k_\lambda^{'}(x)\left[\,S_\lambda(x) - I_\lambda(x)\,\right]dx \qquad (2\text{-}2)$$

In an homogeneous plasma (e.g. the wall-stabilized arc in end-on measure-
ments), the source function and the net absorption coefficient are independent
of position: $S_\lambda(x) = S_\lambda$; $k_\lambda^\bullet(x) = k_\lambda^\bullet$. With the boundary conditions for a plasma
of length L:

$$I_\lambda(x{\leq}0) \;=\; I_\lambda(0) \qquad ; \qquad I_\lambda(x{\geq}L) \;=\; I_\lambda(L)$$

Eq. 2-2 can easily be integrated, yielding:

$$I_\lambda(L) \;=\; S_\lambda\left[1 - \exp\left(-k_\lambda^\bullet L\right)\right] \;+\; I_\lambda(0)\exp\left(-k_\lambda^\bullet L\right) \qquad (2\text{-}3)$$

$$=\; I_\lambda^{Em} \;+\; I_\lambda^{Abs}$$

---

[*] net absorption equals absorption minus induced emission, which should be
properly considered negative absorption.

In an emission measurement: $I_\lambda(0) = 0$, and we measure I_λ^{Em}. In the technique used for absorption measurements, the radiation from the background source is selectively modulated. By synchronous rectification of the ac signal from the detector, I_λ^{Abs} can then be measured without interference by the dc signal due to plasma emission. $I_\lambda(0)$, the intensity of the light from the background source, is measured independently, and we obtain the absorptance α_λ:

$$\alpha_\lambda = \frac{I_\lambda(0) - I_\lambda^{Abs}}{I_\lambda(0)} = [1 - \exp(-k_\lambda' L)] \tag{2-4}$$

Finally, a concurrent measurement of emission and absorption yields the source function:

$$S_\lambda = I_\lambda^{Em} / \alpha_\lambda \tag{2-5}$$

If local thermodynamic equilibrium obtains, the source function equals the Planck function by Kirchhoff's law. Ignoring the small variation of λ over the linewidth, S_λ is thus constant within a line. This is still true in collision-dominated non-equilibrium plasmas (i.e. the line shapes for emission and absorption are also the same), but S is then given by the principle of detailed balancing as:

$$S(\text{line}) = \frac{2 h c^2}{\lambda^5} \left(\frac{n^*(i)}{n^*(j)} - 1 \right)^{-1} \tag{2-6}$$

where j is used to denote the upper, and i the lower energy level for the transition. In non-equilibrium, a distribution temperature T_D can be defined by formally equating the source function to the Planck function:

$$\exp\left[(E_j - E_i)/kT_D \right] \approx n^*(i) / n^*(j) \tag{2-7}$$

Because of the near-constancy of S over the width of the line, low-resolution instruments can be used to determine the distribution temperature, provided the spectral bandpass remains the same in the emission and absorption measurements (10). When a spectrometer of sufficiently high resolving power is available such that a record of the true line shape can be obtained, the spectral radiance over the line (i.e. the profile of the unabsorbed line corresponding to spontaneous emission) can be constructed point-by-point from the spectral scan in emission of an optically thick line, since, as follows from Eqs. 2-3, 2-4, and 2-5:

$$N_\lambda = \epsilon_\lambda L = \ln\left[\left(1 - \frac{I_\lambda^{Em}}{S}\right)^{-S}\right] = I_\lambda^{Em} \ln\left[(1 - \alpha_\lambda)^{-1/\alpha_\lambda}\right] \qquad (2\text{-}8)$$

The integral of N_λ over the line is related to the occupation of the upper energy level via the transition probabilities (Eq. 2-11). Under favorable circumstances, an emission-absorption measurement at high spectral resolution yields the occupation of both, the upper and the lower energy level for the transition. The precision of this method depends on the magnitude of the absorptance. At small absorption the optically thin approximation is recovered, since $N_\lambda \approx I_\lambda^{Em}$ for $\alpha_\lambda \to 0$. The other limiting case is given by a line which is black in the center, and then only the distribution temperature can be determined, since $N_\lambda \to \infty$ for $\alpha_\lambda \to 1$.

A spectral scan of the line in both modes is not required, and in plasma measurements the source function can be obtained by determining only the absorptance at the line center. (The situation is reversed for most flames where considerations of noise favor absorption measurements). Often the source function can be extracted from high-resolution measurements in emission alone.

Consider the case of two adjacent lines, one of which is strong and the other weak, and whose relative line strengths are accurately known. Since

14

Russel-Saunders coupling is well obeyed by the light atoms of interest in plasma spectroscopy, atomic multiplets can easily be found that meet these requirements. The case of the ultraviolet bands of OH is also favorable because of the presence of main and satellite branches in the rotational structure which form several convenient line pairs. Their relative strength is given by the Hoenl-London factor. If R is their line strength ratio, then $N'_o = R N''_o$. The strong line will be self-absorbed in the center if we find $I'_o < R I''_o$. (Single primes refer to the strong, double primes to the weak line)[*]. Assuming the weak line to be optically thin ($I''_o \approx N''_o$), we can write, using Eq. 2-8:

$$R \, I''_o/I'_o \; = \; N'_o \, / \, I'_o \; = \; - \, 1/\alpha'_o \, \ln \, (1 - \alpha'_o) \qquad (2\text{-}9)$$

It should be noted that α'_o can be directly derived from the measured ratio I''_o/I'_o only when the true emission profiles have been resolved. Once α'_o has been found (e.g. from a plot of the function on the right side of Eq. 2-10), one can improve the accuracy by calculating now α''_o and iterating. However, this is rarely required if lines are chosen for which R > 10. Since $\alpha_o = I_o/S$, the distribution temperature between the occupation of the two energy levels follows immediately.

Once the source function has been determined, the experimental profile of I_λ can be converted into the profile of N_λ by using Eq. 2-8; this is not neces-sary, however, if only the half width - or any other fractional width - is re-quired, since, as follows from the same equation:

$$I_{\lambda*} \, / \, I_o \; = \; [1 - (1 - \alpha_o)^{1/n}] \, / \, \alpha_o \; ; \quad \text{with } N_{\lambda*} = N_o \, / \, n \qquad (2\text{-}10)$$

---

[*] Here and in what follows the subscript λ_o for the line center has been simplified, and the emission superscript has been dropped.

The half width hw corresponding to N_λ, the profile of the optically-thin line, can thus be obtained by measuring directly the width of the recorded emission profile I_λ at the fractional height given by Eq. 2-10 with n = 2.

B. Optical Transition Probabilities for the Rotational Lines of OH ($A^2\Sigma$-$X^2\Pi$)

The integrated spectral radiance of an optically-thin line, corresponding to a transition from energy level j to energy level i, emitted by an homogeneous plasma sample of length L, is given by:

$$N_L \equiv \int_{line} N_\lambda \, d\lambda = L \int_{line} \varepsilon_\lambda \, d\lambda = \frac{h\nu}{4\pi} L \, n(j) \, A(j,i) \qquad (2\text{-}11)$$

in energy per second, per square centimeter, and per steradian. $n(j)$ is the population density of the upper energy level j, and $A(j,i)$ the Einstein spontaneous transition probability.

Consider the energy levels i and j to be formed by a group of closely spaced energy sublevels i_r and j_s, respectively. These sublevels do not necessarily correspond to degenerate states of equal statistical weight; however, it is assumed that the sublevels j_s are so close together that their relative occupations are given simply by their statistical weights:

$$n(j_s) = n(j) \, g(j_s) \, / \, \sum_s g(j_s) \quad , \qquad \text{and:} \qquad (2\text{-}12)$$

$$N_L(j,i) = \sum_{s,r} N_L(j_s,i_r) = \frac{h\nu}{4\pi} L \, n(j) \sum_{s,r} g(j_s) \, A(j_s,i_r) \, / \, \sum_s g(j_s) \qquad (2\text{-}13)$$

By equating Eqs. 2-11 and 2-13 we obtain:

$$A(j,i) = \sum_{s,r} g(j_s) \, A(j_s,i_r) \, / \, \sum_s g(j_s) \qquad (2\text{-}14)$$

16

If the sublevels j_s correspond to truly degenerate states of the energy level j, then $g(j_s) = 1$ for all s, and:

$$A(j,i) = \sum_{s,r} A(j_s,i_r) / g(j) \qquad (2\text{-}15)$$

For electric dipole transitions the transition probability is related to the square of the matrix element of the dipole moment (transition moment) by:

$$A(j,i) = \frac{64 \pi^4}{3 h \lambda^3} \sum_{s,r} |R(j_s,i_r)|^2 / g(j) \qquad (2\text{-}16)$$

Because of the more complicated structure of molecules, errors have often been made when these concepts have been applied to molecular spectroscopy. The conceptual framework for a correct quantitative interpretation of intensities in diatomic molecular spectra has recently been reviewed in detail by Tatum (11).

The ultraviolet bands of OH belong to a $^2\Sigma^+ - ^2\Pi_{inv}$ transition. The selection rules for J ($\Delta J = 0, \pm 1$, but not $J=0 \leftrightarrow J=0$) and p (only states of different parity combine) are strictly obeyed. For Hund's case (b) we also have the selection rule for K equivalent to the selection rule for J. The transitions that satisfy all selection rules form the six main branches of each vibrational band. Since the $X^2\Pi$ state is intermediate between case (a) and case (b), the selection rules for K are not strictly valid and are violated by the six weak satellite branches. The energy level diagram and the transitions corresponding to the 12 branches are shown schematically in Fig. 1. The energy levels of the electronic ground state have been labeled according to Hund's case (b). Although this is a Π state, Λ-type doubling does not lead to doublet lines because of the $+ \leftrightarrow -$ selection rule (see Fig. 1).

The integrated spectral radiance of a line of a branch is then given according to Eq. 2-11 by:

$$N_L(n'v'K'J', n''v''K''J'') = \frac{h\,c\,L}{4\,\pi\,\lambda}\, n(n'v'K'J')\, A(n'v'K'J', n''v''K''J'') \quad (2\text{-}17)$$

where n' and n" in the index are used to denote the upper ($A^2\Sigma$), and the lower electronic state ($X^2\Pi$), respectively. Since the spin splitting is small, Eq. 2-12 is used to relate the occupation of each sublevel J' to the occupation of the rotational level K':

$$n(n'v'K'J') = n(n'v'K')\,\frac{2J' + 1}{(2S + 1)(2K' + 1)} \quad (2\text{-}18)$$

The spin quantum number S is not indexed because of the selection rule: S' = S" = S. The statistical weight of the J' sublevel is 2J' + 1 (No Λ-type doubling), and the transition probabilities in Eq. 2-17 are then given by:

$$A_{21} \equiv A(n'v'K'J'', n''v''K''J'') = \frac{64\pi^4}{3h\lambda^3}\, \sum_{m',m''} \left| R(n'v'K'J'm', n''v''K''J''m'') \right|^2 / (2J'+1) \quad (2\text{-}19$$

as follows from Eq. 2-16. m is the magnetic quantum number.

Based on the Born-Oppenheimer approximation, the matrix element can be separated into a radial and an angular part. The integration over the rotational coordinates can be carried out, and we obtain:

$$A_{21} = \frac{64\,\pi^4}{3\,h\,\lambda^3}\, \left| R(n'v'J', n''v''J'') \right|^2\, \frac{S(K'J', K''J'')}{(2J' + 1)} \quad (2\text{-}20)$$

The Hoenl-London factors or rotational line strengths S(K'J', K"J") obey the sum rule:

$$\sum_{K'',J''} S(K'J', K''J'') = 2J' + 1 \quad ; \quad \sum_{K',J'} S(K'J', K''J'') = 2J'' + 1 \quad (2\text{-}21)$$

The Hoenl-London factors given in the literature have to be used with caution since they are often not properly normalized, thus Dieke and Crosswhite's (12) HL-factors for the OH bands have to be divided by 8 in order to satisfy Eqs. 2-21. The HL-factors in Table 4 of Ref. 12 also have been calculated with the same average value for the coupling constant ($\bar{a} = -7.55$). The dependence of a on rotational quantum number for the $v=0$ level of the electronic ground state is shown in Fig. 2 for $K \leq 20$. For higher K values, the magnetic interaction between $\vec{K}$ and $\vec{S}$ has to be taken into account, and the equation used for this computation (Eq. 14 of Ref. 12) is then no longer valid. The effect on the HL-factors of the increase of a with K is practically negligible for the strong branches, but significant for the satellite branches. (see Section 6C).

The validity of factoring the matrix elements in Eq. 2-20:

$$\left| R(n'v'J', n''v''J'') \right| = \int \Psi'(v'J') R_e(r) \Psi''(v''J'') \, dr \qquad (2-22)$$

in order to assign a transition probability to a band and derive Franck-Condon factors for the different bands of a system, has been critically examined by James (13), and by Anketell and Learner (14), with special consideration of the OH molecule. Because of the variation of R_e with internuclear distance (i.e. its dependence also on v and J), it can, in general, not validly be replaced by an average value that can be taken out of the integral. Secondly, as denoted in Eq. 2-22, the vibrational wavefunctions are also J-dependent if the effect of vibration-rotation interaction is taken into account.

Although rigorously the matrix element will thus be different for each rotational line, its dependence on J is a second order effect, and it appears plausible that the matrix element can still be represented by a factor that is

constant for a vibrational band, and a correction factor that depends on the rotational transition involved:

$$|R(n'v'J',n''v''J'')|^2 = |\bar{R}(n'v',n''v'')|^2 \; T(J',J'') \qquad (2\text{-}23)$$

This representation of the matrix element is useful only if $T(J'J'')$ can be approximated by a simple mathematical expression containing the rotational quantum numbers. This is indeed the case for the rotational lines of OH, as shown in Section 6D and further discussed in Section 12.

Formally, one can also define an average transition probability for a vibrational band:

$$\bar{A}(n'v',n''v'') \equiv \frac{64\,\pi^4}{3\,h\,\bar{\lambda}^3} \; |\bar{R}(n'v',n''v'')|^2 \qquad (2\text{-}24)$$

This concept is not useful, however, because it is not possible to assign unambiguously an average wavelength $\bar{\lambda}$ to a band. The same reservation applies to the equivalent quantity: "band oscillator strength".

The measured integrated radiance of a rotational line is expressed here in terms of the state occupation of the upper rotational level K', the "P-factor", and the (rotational) "line strength factor". As follows from Eqs. 2-17, 2-18, and 2-20:

$$N_L = \frac{hcL}{4\pi} \; n*(n'v'K') \; P(n'v'J',n''v''J'') \; S(K'J',K''J'')/\lambda^4 \qquad (2\text{-}25)$$

where the state occupation (defined by Eq. 1-1) is given by:

$$n*(n'v'K') = \frac{n(n'v'K')}{(2S+1)(2K'+1)} = n(n'v'K'J'm') \qquad (2\text{-}26)$$

and:
$$P(n'v'J',n''v''J'') \equiv \frac{64\,\pi^4}{3\,h} \; |R(n'v'J',n''v''J'')|^2 \qquad (2\text{-}27)$$

The "P-factor" defined by Eq. 2-27 is formally equivalent to a transition probability times the cube of a wavelength (compare Eqs. 2-24 and 2-27), and is introduced here because it is dimensionally more convenient than the square of the matrix element.

Customarily, the classical expression involving the oscillator strength is used to relate the occupation of the lower level for a transition to the integrated line absorption coefficient. Here we use the source function to establish the relation between the equivalent quantities obtained by an absorption and by an emission measurement, respectively:

$$\int_{line} k'_\lambda \, d\lambda = S^{-1} \int_{line} \mathcal{E}_\lambda \, d\lambda = S^{-1} \, N_L/L \qquad (2-28)$$

as follows from the definition of the source function S and from the invariance of S over the line (see preceding Section 2A). By substituting the expressions for S (Eq. 2-6) and for N_L (Eq. 2-25), we obtain:

$$\int_{line} k'_\lambda \, d\lambda \approx \frac{1}{8\pi c} \, n^*(n''v''K'') \, P(n'v'J', n''v''J'') \, S(K'J', K''J'') \, \lambda = \int_{line} k_\lambda \, d\lambda \qquad (2-29)$$

In Eq. 2-29 we have written $n^*(n''v''K'')$ instead of the correct factor $\lceil n^*(n''v''K'') - n^*(n'v'K') \rfloor$ because the electronic energy term for the transition OH ($A^2\Sigma - X^2\Pi$) is so large that in all practical situations the state occupation of the lower level is orders of magnitude higher than the state occupation of the upper level, i.e. stimulated emission is insignificant compared to absorption.

If the integrated absorption coefficient is related to the level occupation and the oscillator strength), the Λ-type doubling of the spin sub-levels J" as to be taken into account:

$$n^*(n''v''K'') = \frac{n(n''v''K'')}{2(2S+1)(2K''+1)} = n(n''v''K''J''p''m'') \qquad (2-30)$$

21

Many years ago, Condon and Shortley (50) have already stressed the symmetry achieved by representing the intensities and integrated absorption coefficients of atomic lines in terms of state occupations and transition moments (called "line strengths" by these authors), instead of in terms of level occupations and transition probabilities (or oscillator strengths).

It should be noted here parenthetically that in absence of LTE the level occupation is mostly not a useful quantity. The population distribution over excited energy levels is then conveniently discussed in terms of the Boltzmann plot, i.e. the representation of the log of the state occupation vs. the energy term. The slope of this plot is determined by the "distribution temperature" (Eq. 2-6), an experimentally measurable paramater. The pertinent state occupations and not the species concentration and the -undefined - partition functions enter the mass action equations for non-equilibrium plasmas (see Section 7). Even the rate coefficients are more conveniently expressed in terms of the state occupations (Section 8A).

Whereas in the case of atomic lines the two representations involve essentially only a matter of form, Eqs. 2-25 and 2-29 - based on Condon & Shortley's representation - appear definitely more appropiate in the case of molecular lines. This is due to the fact that - in addition to the practical advantage of avoiding the complications due to Λ-type doubling - the radial part of the transition moment can often be conveniently expressed in the form given by Eq. 2-23. Attempts to introduce a wavelength-dependent electronic transition probability or oscillator strength (51) appear rather artificial.

We shall often use the quantity formally equivalent to the radial part of the transition moment of the vibration- and rotation-less molecule:

$$P^o_o = P(A^2\Sigma,0,0;X^2\Pi,0,1) \tag{2-31}$$

P^o_o is essentially the "P-factor" corresponding to the P-1 lines of the (0,0) band. Bennet and Dalby have inferred an absolute "band oscillator strength" for the (0,0) band - $f(0,0) = 8 \times 10^{-4}$ - from lifetime measurements with a wide spectral bandpass. (15). Based on this value, one can estimate P^o_o to be of the order of $3.3 \times 10^4 \, s^{-1} \mu^3$.

3. Equilibrium Composition of Water Vapor Plasmas

In the temperature range of interest (2000 - 6000K), ionization is negligible, and six components of a water vapor plasma have to be considered. With their partial pressures expressed as:

$p(H_2) = u$; $p(O_2) = v$; $p(H_2O) = w$; $p(OH) = x$; $p(O) = y$; $p(H) = z$;

we can write:

$$u \, v^{1/2} \, w^{-1} = K_1$$
$$x \, u^{1/2} \, w^{-1} = K_2$$
$$z \, u^{-1/2} = K_3$$
$$y \, v^{-1/2} = K_4$$
$$u + v + w + x + y + z = P$$
$$2u + z = 4v + x + 2y$$

here the last equation follows from the condition that the total concentration of hydrogen atoms must be twice the total concentration of oxygen atoms.

This system of equations was solved for the six unknowns on an electronic computer for various pressures and temperatures, using two sets of input data, with the equilibrium constants $K_1 - K_4$ taken from: (a) the composition data for a water vapor plasma at 1 atm given by Burhorn and Wienecke (16); and b), the data compiled in the JANAF tables (17). Sizable discrepancies appeared in the output data that were largest for the datum of major interest, the concentration of OH, amounting to as much as 60% in some cases.

This disagreement was traced to a discrepancy in the equilibrium constant for the dissociation of OH. Since the basic input data are not indicated in Ref. 17, we resorted to a direct calculation of this equilibrium constant.

We used the value for the dissociation energy of OH accepted at present (D_o = 35,501 cm^{-1}), and considered the effect of vibration-rotation interaction in the calculation of Q(OH), the internal partition function of OH. However, over the temperature range of interest the small increase with temperature of the correction factor for Q(OH) due to vibration-rotation interaction (see Eq. 7-39 in Ref. 18), is approximately cancelled by the increase of Q(0). The contribution of the excited electronic states to the partition function is also negligible, and K_p(OH) can then be represented by an expression in closed form, accurate to within 5% for T < 6000 K . With partial pressures in atm:

$$K_p(OH) = \frac{p(O)\ p(H)}{p(OH)} = 2.70\ T^{3/2}\ (1 - 10^{-2231/T})\ 10^{-22180/T} \qquad (2\text{-}32)$$

The agreement between the calculated K_p(OH) and the value listed in Ref. 17 was within 1% at 3000 K, and still within 8% at 6000 K. Therefore we conclude that the JANAF tables are essentially correct whereas the calculation of Ref. 16 appear to be in error. With the equilibrium constants taken from the JANAF tables, the equilibrium composition of water vapor plasmas was then computed (in steps of 100 K) at the following pressures: 0.02; 0.03; 0.04; 0.05 and 1 atm. The results for 1 atm and 0.02 atm are shown graphically in Figs. 3 and 4.

D. The Fowler-Milne Method in Plasma Spectroscopy

In equilibrium plasmas the population density of excited states relative to the species concentration is a monotone-increasing function of temperature. The concentration of a free radical such as OH increases initially with temperature, but then decreases as the dissociation process into atoms begins to predominate. At still higher temperatures the dissociation loss also overrides the increase in the Boltzmann factor for excited states. The number density of emitters reaches, therefore, a maximum value n(max) at a specific temperature - the "normal" temperature - beyond which it decreases again. For LTE-plasmas of given chemical composition at standard conditions, n(max) and the normal temperature can both be calculated. If the plasma is optically thin, n(max) for a certain energy level corresponds to a maximum in line intensity for transitions originating in this level. This is the basis of the Fowler-Milne method introduced by Larenz in the diagnostics of arc plasmas (19). The method is appealing because no prior knowledge of the transition probability is required; in fact, it should be possible to derive both, the temperature and the transition probability from such a measurement.

The Fowler-Milne method has been used in the past to determine the temperature profile of optically thin arc plasmas, if the Abel inversion of the experimental data obtained by side-on measurements showed that the radial intensity distribution was peaked off the arc center. The usefulness of this procedure is impaired in practice because small experimental scatter in the measured intensities or deviations from radial arc symmetry may induce a spurious off-axis peak in the inverted data and lead to temperatures which are utterly wrong.

The noted experimental difficulties can be avoided in end-on measurements. Variation of the arc current provides a simple means of changing the core

25

temperature while changes in the intensity of a spectral line are directly monitored by the recorder display. Provided the arc can be run at a current large enough to exceed the normal temperature, it is then possible to adjust the arc current accurately and unambiguously for peak intensity of the spectral line. As opposed to the customary side-on measurements, the temperature regime of interest (normal temperature for the studied spectral feature) is shifted by this procedure from the arc periphery, where measurements are less accurate, to the arc core.

In Fig. 5 we show the calculated occupation of two rotational levels of OH in a water vapor plasma. It can be seen that over a wide temperature range the number density of emitters (i.e. the line intensity) is almost constant. This implies, of course, that the Fowler-Milne method is not a particularly good (i.e. sensitive) method to determine the plasma temperature.

In the case of interest this argument has to be inverted, however: if the arc current is adjusted to such a value that the peak temperature in the arc core is close to the normal temperature for the spectral line whose transition probability we want to measure, the line intensity will be constant over a relatively wide cross section of the arc and, moreover, will be insensitive to small fluctuations of arc temperature.

3. APPARATUS AND EXPERIMENTAL TECHNIQUES

A. High-Resolution Scanning Spectrometer

The requirements for a spectrometer matching the constraints of arc sources used in plasma spectroscopy are quite different from the traditional design criteria for commercial spectrometers. The focal length of these instruments is relatively small as compared to the size of the grating; but in end-on measurements of arc plasmas, for example, f-numbers of the order of f/100 are dictated by the requirement to isolate a narrow beam of light emerging from a homogeneous plasma region. Thus in a spectrometer with a large aperture only a small fraction of the grating surface will be illuminated, which is not only wasteful but also severely limits the attainable resolution. Concurrently, very narrow field stops are required, and the entrance slit has to be masked down to a fraction of a millimeter. This obviates the need to correct for image curvature in a Czerny-Turner instrument, which is unavoidable in high resolution work with long slits. Finally, the convenience of a direct wavelength read-out over a wide spectral range, although important for a general purpose spectrometer, has to be sacrificed if a grating is to be used in several higher orders, so as to achieve maximum resolution.

We have built a Czerny-Turner spectrometer, specifically designed for high-resolution plasma spectroscopy and whose optical parameters - f/40 aperture and 5 meter focal length - match the characteristics of our wall-stabilized arc. For work in the near UV and visible, the 600 lines/mm grating blazed at 54° is used in higher orders. With the grating fully illuminated, the theoretical resolving power e.g. at 3000 $\overset{o}{A}$ in the 9th grating order is 830,000. The actual performance of a scanning spectrometer of such high resolving power is usually not determined by the optical components, however, as would be the case for a spectrograph using photographic detection, but rather by the mechanical quality

of the drive mechanism. Thus any unevenness in the rotational motion of the grating - due to slip-stick effects of the bearing, translational errors of run of the pushrod and other effects - has to be small on an angular scale equivalent to the maximum theoretical resolution. At 3000 $\overset{o}{A}$ (9th order) this turns out to be an angle as small as 0.3 seconds of arc.

We use a high-precision grating drive, following a design by McCubbin et al. (20). A spectrum is scanned by rotating the grating via a lever arm moved tangentially by an advancing 50 mm micrometer screw. The lever arm is held by a rigidly mounted rolled spring, whose pulling force is independent of displacement, against a pushrod which has quartz flats attached to both ends. The quartz plates press against hardened steel balls on the tip of the micrometer screw and on the lever arm.

The angle of rotation of 9° provided by the fine grating drive covers the blaze of the grating at higher orders (i.e. the angular range of maximum grating efficiency). Synchronous electric motors and a gear train are used to provide three scanning speeds (ratio 1:10:100), the slowest speed of rotation being 13 seconds of arc per minute. A motor-driven "coarse drive", and an angular scale are available for positioning the grating at any angle. For accurate wavelength settings we resort to the micrometer scale of the fine drive and to reference lines of known wavelength. Using the technique of multiple overlapping orders, the few strong lines in the Hg I spectrum provide enough wavelength markers. For rigidity, the front plate containing entrance and exit slit, the grating drive assembly, and the two Czerny-Turner mirrors are mounted on a heavy "ship-builder's" 45-cm-wide steel channel. The simple expedient of embedding the steel channel in sand provides isolation against mechanical vibrations transmitted through the floor. The instrument cover and the exposed part of the steel channel

were lined first with urethane foam for thermal insulation, and then with black cotton velvet to minimize light scattering.

A solenoid-actuated fold-mirror is placed behind the exit slit and the dispersed light can be directed to either of two photomultipliers so that simultaneous measurements can be made over a wide spectral range without detector inter - change, an important feature for plasma spectroscopy. A dry-ice-cooled RCA 7102 (S-1 response) is used for measurements above 8000 Å, corresponding to low grating orders (2nd and 3rd), and glass filters are suitable for discriminating against overlapping orders. For the near UV and visible, an EMI 9558 QA photomultiplier with an S-20 response, especially selected for low dark current and high cathode sensitivity, is used in conjunction with a simple quartz prism-monochromator of the Bunsen-Kirchhoff type, as order sorter. The collimator and telescope lens are also made of quartz, and two indexed telescoping mounts are provided, so that the change of focal length with wavelength can be compensated. The bandpass defined by a slit of width s in the focal plane must be narrower than the free spectral range in the grating order used. For a grating used in higher orders near its blaze $\left(\lambda_{bl}\right.$ = blaze wavelength in the first order), s is then determined by:

$$ s \leq \frac{2\,D}{\lambda_{bl}}\ \lambda^2 \qquad\qquad (3\text{-}1) $$

where D is the linear dispersion of the prism monochromator. In order to minimize stray light usually a much narrower slitwidth than given by Eq. 3-1 was used.

Since in our measurements only a small area of the photomultiplier cathode was illuminated, a permanent focusing magnet was used to improve the performance of the detector, as recommended by Knight et al. (21). This simple expedient

proved to be effective: the gain was enhanced by an order of magnitude and the signal-to-noise ratio by a factor better than three. The signal from the photomultiplier, modulated by a 1 KHz light-chopper, is synchronously rectified by a lock-in amplifier and displayed by a strip chart recorder.

Once the spectrometer has been carefully aligned, focusing of the telescope Czerny-Turner mirror is the critical instrument adjustment for maximizing the resolution. This was accomplished by using a low-pressure mercury discharge as the source and, with the aid of a microscope, visually adjusting for optimum sharpness of the hyperfine components of the Hg I 5461 $\overset{o}{A}$ line in the plane of the exit slit.

The hyperfine structure of Hg I 4358 $\overset{o}{A}$ is more convenient for resolution checks. In Fig. 6 a typical strip chart record of this line is shown, obtained at the slowest scanning speed with a slit height of 4 mm, slit width of 0.030 mm, and an aperture of f/80. The theoretical resolving power in the 6th order for the grating set at an angle of $51^{o}40'$ and illuminated by an f/80 light beam, is 360,000 which corresponds to a resolution of 12 m$\overset{o}{A}$. Since the doublet, whose peak separation is 13 m$\overset{o}{A}$, is better resolved than given by the Rayleigh criterion, the theoretical resolution has been achieved. In Fig. 7 we have plotted the measured chart positions of the resolved hyperfine lines vs. the wavelength increment, and the straight line corresponding to the calculated chart dispersion has also been drawn. The insignificant data scatter demonstrates the smoothness of the grating drive. Rather unexpectedly, almost the same precision could be achieved when the line was scanned in the reverse mode (i.e. when the lever arm is pulled by the spring instead of being pushed).

After several months of intensive use of the instrument, a slight degradation of resolution was noticed, and could be traced to pitting of the quartz flats attached to the pushrod. These can be quickly replaced. Because of the proximity of passing trains (the spectrometer was located only 50 meters away from an active railroad track), we checked for a possible transmission of floor vibrations. However, while sitting on the peak of a hyperfine line of Hg 4358 $\overset{o}{A}$, no signal variation was detected when a high-speed train rushed by. The simple precautions taken in order to isolate the spectrometer from environmental effects appear, therefore, to be entirely adequate.

The experimental set-up for concurrent emission and absorption measurements is shown schematically in Fig. 8. So as to ensure that only light emitted by a homogeneous plasma sample falls on the detector, we had to limit the entrance slit of the spectrometer to a "pinhole" of 0.1 x 0.25 mm, and the aperture to less than f/100. The cathode spot of the xenon arcs used as background sources for absorption measurements, does not maintain the required spatial stability over such small dimensions, but constantly "wanders". The behavior of the available popular types of xenon lamps (Hanovia 491C39 and 959C98) was essentially identical, and we assume that this is an intrinsic characteristic of free-burning arcs. Moreover, the spectral radiance of the xenon arcs in the UV was too low for absorption measurements of the strong OH lines at high spectral resolution. Because of its stability and its higher intensity in the UV, if available, another wall-stabilized arc in the end-on mode, run at high current and filled with argon at, say, 2 atm pressure, would have provided an ideal background source for these measurements.

Different masks on mirror M_2, which focuses the source on the entrance slit at unit magnification, were calibrated and used as aperture stops. For a

uniform source, the signal was found to be exactly proportional to the illuminated area of M_2. Wider apertures were required for intensity calibrations in the UV.

B. Intensity Calibration

A high-current strip lamp with quartz window (GE 30A/T24/13) was our standard source for the intensity calibration. The temperature of the tungsten strip was determined with an optical pyrometer recently calibrated by the National Bureau of Standards. If T_{obs} is the measured temperature in K, we determine the true temperature from the following relation between the radiance of a blackbody and of the striplamp at $\lambda_o = 6530$ Å:

$$N_{BB}(T_{true}, \lambda_o) = \epsilon_{ef} \, N_{SL}(T_{obs}, \lambda_o) \qquad (3\text{-}2)$$

The effective emissivity is given by the emissivity of tungsten times the transmittance of the quartz window:

$$\epsilon_{ef} = 0.92 \, \epsilon_W(T_{true}, \lambda_o) \qquad (3\text{-}3)$$

Using Wien's law, which in this range is accurate to 0.1%, we have with $T^* = 10^{-3} T$:

$$1/T^*_{true} = 1/T^*_{obs} + \log \epsilon_{ef} / 9.569 \qquad (3.4)$$

Eq. 3-2 and 3-4 were solved by iteration based on DeVos' (22) graphs of $\epsilon_W(T, \lambda)$, which had to be extrapolated to 3000 K. These graphs were also used to calculate the radiance of the strip lamp at various wavelengths.

A step-down transformer with the line voltage stabilized by a Sola transformer supplied ac power to the striplamp. This simple power supply was adequate; after a short warm-up period the excursions in temperature from a median $T_{true} = 3012$ K were less than 5 K. This is only slightly higher than the precision of the pyrometer reading. The striplamp was run at the highest permissible temperature in order to increase the radiance in the UV. An available carbon arc

was also tested but finally discarded because its measured radiance in the UV - the only spectral region where its use could be advantageous - was significantly higher than calculated, possibly due to interference by CN bands.

Since the intensity of the strip lamp is so much weaker in the UV than at longer wavelengths, stray light constitutes a serious problem for accurate calibrations in the spectral range of the OH bands. In our spectrometer spurious light of significant intensity can come only from overlapping orders. The wavelength of the stray light is thus known, and its magnitude can be determined with suitable filters. The stray is caused by random scattering by the optical components of the order sorter, and our tests verified this, since the magnitude of the stray was proportional to the width of the exit slit of the order sorter. When working in the UV, spurious light was minimized, therefore, by using slit-widths much narrower than determined by Eq. 3-1, and by using also a glass filter with a wide bandpass in the UV and a cut-off around 4100 $\overset{o}{A}$ (Corning 7-54). With these precautions the residual stray light at 2810 $\overset{o}{A}$ (the shortest wavelength at which measurements were made in this investigation) was determined to be below 5%, an acceptable level.

A stray light problem appeared again in the infrared towards the limit of the useful range of a photomultiplier with an S-20 response, caused in this case by the decrease of quantum efficiency of the detector. This stray could be easily eliminated by resorting to available glass filters with cut-on in the visible.

C. Plasma Source

In prior related work we developed a wall-stabilized arc which includes several new design features in order to increase the versatility of this source and extend its useful range to lower pressures and also to the study of gases which before have been difficult to maintain in a quiescent state, e.g. water vapor plasmas. This device has been described elsewhere (23). The copper segments forming the arc channel were redesigned in order to reduce the channel diameter from 6.3 to 4 mm. This was necessary in order to stabilize the arc column which contracts at the lower arc currents, an effect especially pronounced for molecular gases. Leads were attached to the end plates of the arc-sections facing the electrodes, and the field strength in the sample section could then be determined by measuring the voltage drop (see Section 9C).

When using a power supply with a "drooping" V-I characteristic, a stable arc can be maintained only if the slope of the V-I characteristic of the load (arc + series resistor of resistance R) is positive; the constraint being, that the total voltage drop cannot exceed the open circuit voltage, i.e.

$$\frac{dV_T}{dI} = \frac{dV_A}{dI} + R + I\frac{dR}{dI} > 0 \quad ; \quad O.C.V. > V_A + IR \qquad (3-5)$$

At high currents, the V-I characteristic of the arc is positive, and a very stable arc can be maintained with a battery of Miller rectifiers (23). At low currents the slope becomes negative, however, and a series resistor has to be included in the circuit; but stabilization at 4 Amps. became critical when a water-cooled resistor $(dR/dI = 0)$ was used. A substantial improvement of arc stability was achieved by using instead a battery of incandescent light bulbs as a "dynamical" series resistor $(dR/dI > 0)$. Thus, for example, the intensity of Ar I 4300 $\overset{o}{A}$ remained constant to within 1% over a run, and the

run-to-run repeatability at constant current was of the order of 3%. By taking recourse to a very simple strategem, the stability of our arc matches the best performance of arcs reported in the literature and achieved by using elaborate feed-back controls.

D. Accurate Arc Alignment for End-On Measurements

In end-on measurements the arc axis must be aligned parallel to the optical axis of the system, so that the spectrometer views a homogenous plasma sample when appropiate field and aperture stops are used. We achieve this with the aid of a small laser positioned in front of the exit slit. Proof of correct arc alignment can be obtained by comparing the results of end-on measurements with the equivalent inverted data derived from a spatial scan in the side-on mode (23). This test is quite laborious, however, and a different method was used that requires only measurements in the end-on mode.

The arc is filled with argon at atmospheric pressure, the spectrometer is focused on the arc center, and an argon ion line - e.g. Ar II 4348 $\overset{o}{A}$ - and the adjoining continuum are measured at, say, three different settings of the arc current. Both spectral features are optically thin. For the data reduction we use three graphs derived from the calculated composition of an argon plasma at 1 atm, and representing as a function of temperature (a) the integrated spectral radiance of Ar II 4348 $\overset{o}{A}$, (b) the spectral radiance of the continuum at 4350 $\overset{o}{A}$ (both per unit optical path length), and (c) the ratio of these two quantities.

Graph (c) is used to derive the "core temperature", i.e. the temperature of the plasma sample corresponding to the arc axis, from the measured signal ratio. (The instrument response remains invariant over the small wavelength range covered, and the intensity ratio is independent of optical pathlength).

Once the core temperature has been established, the effective optical path length L* is obtained from the other two plots. Typical results of these measurements are shown in Table I.

TABLE I

CORE TEMPERATURE AND EFFECTIVE OPTICAL PATH LENGTH FOR AN ARGON ARC AT 1 ATM

I (Amp)	T (K)	L*(Ar II) (cm)	L*(cont.) (cm)	T(24) (K)
35	11,950	10.9	10.7	11,640
50	12,750	11.2	10.7	12,320
75	13,500	13.5	13.8	13,230

At given pressure and chemical composition of the plasma, the core temperature of a wall-stabilized arc is uniquely determined by its diameter. Our measurements can thus be compared with the equivalent data reported by Bues et al. (24) for a wall-stabilized arc of almost the same relevant dimension (4.10 mm arc diameter in Ref. 24 and 3.97 mm in our arc). The good agreement between both sets of temperatures is yet improved when corrections are made for the slight difference in arc diameter.

More significant is the agreement between the derived effective optical path lengths and the actual arc dimensions, which were 10.7 cm for the length of the arc channel (test section), and 14.8 cm for the total arc length (distance between electrodes). Our measurements are precise enough to bring out the fact that at the higher currents the hot arc core extends beyond the confining channel into the electrode chambers.

Based on these results, it can be concluded that:

(a) The arc plasma is in local thermodynamic equilibrium.

(b) The correct quantities have been used for the transition probability of Ar II 4348 ($A_{ji} = 1.37 \times 10^8 \text{ s}^{-1}$), and for the representation of the continuum intensity (Eq. 5-5).

(c) Good precision has been achieved in absolute intensity calibration.

(d) The arc axis is coincident with the optical axis.

(e) The field and aperture stops used are appropiate for limiting the light flux falling on the detector to the light emitted by the homogeneous arc core.

Fortuitious agreement appears unlikely in view of the relatively wide temperature range covered by the three concurrent measurements and the different temperature dependence of the intensities: The intensity of Ar II 4348 increases by a factor of about 20 when the current is raised from 35 amperes to 75 amperes, the intensity of the continuum only by a factor of 4.

As a final check, we made use of the high-resolution capabilities of our instrument to derive the Stark broadening parameter for the Ar II 4348 Å line from the measured line shapes, as shown in Table II

TABLE II

MEASURED STARK BROADENING PARAMETER FOR AR II 4348 Å

I (Amp)	T (K)	$n_e \times 10^{-16}$ (cm^{-3})	$\Delta\lambda_T$ (mÅ)	F	$\Delta\lambda_S$ (mÅ)	$\Delta\lambda_S/n_e \times 10^{-16}$
35	11,950	6.33	163	0.87	142	22.4
50	12,750	9.54	231	0.93	215	22.5
75	13,500	12.8	302	0.96	290	22.6

The measured line shape is a convolution of the Stark profile, which is approximately Lorentzian, and of two Gaussians (Doppler and instrument broadening). The Doppler half width followed from the known temperature, and the instrument broadening was determined experimentally by a concurrent scan at the same instrument setting (i.e. same grating order, slit widths, and aperture) of the hyperfine structure of Hg I 4358 $\overset{o}{A}$, generated by a low-pressure mercury arc. Based on the Voigt profile, a correction factor F was calculated in order to derive $\Delta\lambda_S$ from $\Delta\lambda_T$, the measured (full) halfwidth. Since F is close to unity, the precision of measuring $\Delta\lambda_S$ is not sensibly affected by the correction for other broadening mechanisms.

The Stark broadening parameter is obtained by dividing $\Delta\lambda_S$ by the equilibrium electron density calculated for an argon plasma at 1 atm pressure at the measured temperature. The results are shown in the last column of Table II, conveniently normalized for $n_e \doteq 10^{16}$ cm^{-3}. It follows from theory that the Stark broadening parameter should be essentially constant (i.e. a function of n_e alone), and increase only slightly with temperature. This is borne out by the results of our measurements.

No precise experimental values for the Stark broadening parameter of Ar II 4348 $\overset{o}{A}$ are presently available with which to compare our results. It is only known from measurements by other investigators that Griem's calculated values for the argon ion lines are probably too low by a factor of the order of three. Our Stark broadening parameter is 3.8 times larger than calculated by Griem.(4).

It appears that these results, beyond validating our approach, clearly demonstrate that by high-resolution measurements of a homogeneous and time-independent (steady-state) plasma sample, important information can be obtained with higher precision and considerably less labor than has heretofore been possible.

38

4. SIDE-ON MEASUREMENTS AND ABEL INVERSION

The arc was set up with its axis parallel to the entrance slit, and spatially scanned at the location of the middle window. The lateral intensity profiles of the P_1-2 (0,0) and R_1-20 (0,0) lines were recorded while viewing a water vapor arc at reduced pressure. The use of these adjacent lines is advantageous for determining the temperature from their intensity ratio, because of the relatively wide span in upper energy levels, and because the two lines are of comparable intensity in the temperature range of our measurements. Possible errors due to self-absorption are thus minimized. Their relative transition probabilities were set equal to their Hoenl-London factors, which is not quite correct (see Section 6D). The small absolute error in the derived temperatures is inconsequential in this context.

In order to convert the lateral intensity profile into the radial intensity distribution, we used two numerical methods for the Abel inversion, one due to Bockasten (25), and the other to Barr (26). In all cases, each half of the intensity profile was divided into 20 zones, corresponding to increments of 0.2 mm. The spatial resolution of each measurement was 0.1 mm as determined by the width of the entrance slit. The matrix multiplication was performed on a high-speed digital computer.

The center of the distribution was determined as follows: Before the actual run, a lateral intensity profile for the continuum at 3083 Å emitted by an argon plasma at 1 atm pressure, was obtained. By "folding" this profile - which is narrow and quite symmetric - the center can be picked out. The intensity profiles for the rotational lines, obtained next in a run with water vapor at reduced pressure, is much broader because of arc bulging, and shows slight assymetries. It is thus considerably more difficult to determine the center. Agreement with

39

the center found in the argon run is obtained if the profiles are folded to match the wings. Since this is also the procedure used by other investigators, this was the criterion adopted to fix the distribution center.

The results of the measurements of a water vapor arc at 50 Amps. and 22 Torr are shown in Figs. 9 and 10. In Fig. 9 the radial distribution of the emission coefficient for the R_1-20 line is shown as derived from the same input data by using Barr's, and by using Bockasten's method. These data have been combined with the equivalent distribution of the P_1-2 line and converted into the radial temperature profile (Fig. 10). A smooth distribution is obtained by using Barr's method, but the other method leads to considerable data scatter. This is attrib- uted not only to the absence of a built-in data smoothing scheme (Barr uses a least-squares fit), but also to the fact that Bockasten fits the experimental data to an analytical expression which does not reproduce well the points of zero slope. In effect, the scatter is largest at the center of the distribution and at the off-axis peak, which are precisely the regions of greatest interest.

Because of the presence of a pronounced off-axis peak - a situation rarely encountered for the atomic lines used in plasma spectroscopy - our measurements provide an excellent case for testing different methods for the Abel inversion. Direct comparison with end-on measurements is also feasible.

The arc was set up again in the end-on mode and properly aligned with the optical axis of the system. The arc was then spatially scanned along its hori- zontal diameter and the line intensities were recorded in intervals of 0.25 mm. The dimensions of the entrance slit were 0.1 mm wide by 0.25 mm high, and the beam aperture was stopped down to f/300. Thus in each measurement an area ele- ment of the order of only 0.1 mm^2 was "seen" by the spectrometer. Since this amounts to less than 1% of the total cross section of the arc, a sufficiently

high spatial resolution has been achieved.

Two typical intensity distributions are shown in Fig. 11. These measurements not only substantiate the assumption of cylindrical arc symmetry, but also basically agree with the radial intensity distribution derived by side-on measurements. Side-on measurements are affected, however, by "arc bulging" at the location of the small gap between arc section. (23). This effect becomes very pronounced at reduced pressure, and the arc expands to about twice the channel diameter. Thus in side-on measurements the intensity peaks appear slightly shifted towards the arc periphery.

The agreement between the radial temperature profiles obtained by end-on measurements (Fig. 12), and derived from side-on measurements (Fig. 10) can only be called fair, however. More credence is given to the results of the end -on mode because the two lines were measured concurrently for each arc position, whereas in the side-on mode the lateral intensity distribution for each line was measured separately, for reasons of expediency. A slight increase of arc bulging while the R_1-20 line was being measured, could have caused a spurious increase of the measured intensities, leading to higher values for the derived temperature profile. The amplification of errors produced by the Abel inversion may also contribute to the distortion of the temperature profile in the side-on mode.

41

5. DIAGNOSTIC END-ON MEASUREMENTS

A. Choice of Arc Regime

In the measurements at atmospheric pressure, the sample section of the arc was filled with argon saturated with water vapor at room temperature by bubbling argon through an 150 cm high column filled with water and containing a fine wire maze. The intensity of a strong rotational line was monitored, while the arc current was decreased by steps. The Q_1-6 (0,0) line became measurable only at 10 Amps., and its intensity increased rapidly with decreasing arc current, whereas the underlying continuum - essentially proportional to the square of the electron density - showed opposite behavior. Thus at 4.1 Amps. the line was 8 times stronger than at 8 Amps., but the continuum was only 1/3 as strong. These data correspond to the arc core. When the arc at 4.1 Amps. was laterally displaced, so that the spectrometer viewed a region close to the arc periphery, the line intensity increased further by a factor of the order of 3, whereas the intensity of the continuum decreased to 1/6. When in what follows we refer for short to " the arc at atmospheric pressure", we mean the 4.1 Amp. arc burning in argon saturated with water vapor.

Our attempts to run a low-current arc with pure water vapor were unsuccessful. Although the condensation problem was solved by running the arc "hot" (i.e. the inlet temperature of the pressurized cooling water was close to $100^{o}C$), the voltage required to maintain a quiescent arc exceeded our capability of 900 V.O.C.

By reducing the pressure to about 20 Torr, very stable arc operation was achieved with pure water vapor as the sample gas. The plasma expands, filling the arc channel, and the OH bands are strongly excited at relatively high currents corresponding to a positive V-I arc characteristic.

In order to optimize the arc regime for the planned measurements, the intensity of the Q_1-6 (0,0) line was again monitored, while the arc current was varied at constant pressure. The plot of line intensity vs. current corresponding to a pressure of 18 Torr, shows a broad maximum centered at about 37 Amps, dropping to 50% of peak value at 10 Amps. and 60 Amps., respectively. It was also noted that the line intensity depended but weakly on the arc pressure, whereas in LTE the number density of emitters should increase as the square of the pressure.

After this preliminary work had circumscribed the arc regimes to be used, two types of spectroscopic measurements were made. In what we call "Diagnostic Measurements" our aim was to characterize the state of the plasma as completely as possible by resorting to emission and absorption measurements and to line shape studies of suitable atomic lines and of some rotational lines. In another series of measurements we recorded the intensities of all useful - i.e. not overlapped - rotational lines of the OH bands. Since it took about six hours to complete a scan of the entire OH spectrum in the UV, these measurements may appropiately be labelled "Long Runs". Adequate arc stability could be maintained for such extended time periods, but the endurance of the experimenter was severely tested. After two complete scans had been recorded, the data acquisition time was shortened in subsequent "Long Runs" by starting the scan with the (0,0) band. The short wavelength range - i.e. the region of the (1,0) and (2,1) bands - was skipped because it required repeated adjustments of the order sorter and also a painstakingly careful intensity calibration.

In a third series of measurements, 12 selected line groups were measured which comprise 54 rotational lines belonging to the five OH bands studied. Lines of different branches from low to high K-numbers were included. It took a relatively short time to scan these line groups, and measurements were made at various

43

arc currents in an attempt to apply the Fowler-Milne method not only to one line, but to several lines belonging to different bands. The later data analysis revealed, however, that this method is not applicable because of severe departures from LTE. Thus no new information was obtained by these measurements, except that of corroborating the results of the "Long Runs".

B. Measurement of Electron Densities

The theory of Stark broadening of the hydrogen Balmer lines provides the theoretical basis for a convenient method to determine the electron densities in plasmas (2 - 4). Excellent agreement between measured and predicted line shapes has been reported for experiments in which n_e could be independently determined (27,28). The theoretical predictions have not yet been reliably confirmed, however, for $n_e < 5 \times 10^{15}$ cm^{-3}. It is precisely in the lower range, corresponding to departures from LTE in plasmas, where this method would be most useful because the electron density can then no longer be inferred unambiguously from other measurements.

Since H_β - which is generally preferred - showed substantial self-absorption in most of our measurements, we used the H_γ and H_δ lines of the Balmer series as diagnostic lines. Because of the peculiar shape of H_γ, whose center has then the appearance of a narrow cusp, its peak intensity cannot be determined with precision at low electron densities. Moderate self-absorption which has an almost insignificant effect on the integrated line intensity, will "clip" the line peak. It will be further distorted by an experimental slit function, small compared to the half width of the line but wide compared to the narrow peak. The theoretical uncertainties are also largest close to the center, where the line is broadened by electron impact. The theory of quasi-static broadening by ions,

which determines the shape of the line wings, is more firmly established. It is therefore not surprsing that techniques essentially based on a normalization at the line peak, such as inferring the electron density from the half width or from other calculated fractional intensities (29), yielded values that obviously were too high.

In order to compare the recorded line shape with the theoretical Stark profile, we normalize the integrated line intensity:

$$\frac{1}{A} \int_{line} V(\Delta\lambda)\, d(\Delta\lambda) = 1 \qquad (5\text{-}1)$$

where $\Delta\lambda$ is the distance from the line center in $\overset{o}{A}$, and $A = u \times \overset{o}{A}$, is the measured area under the line. The signal (relative line intensity) V is measured in arbitrary chart units u. If other broadening mechanisms can be disregarded, a one-to-one correspondence can be established between the experimental line profile - the integrand in Eq. 5-1 - and the normalized Stark profile for this line. The latter is conveniently expressed in terms of the α-parameters:

$$\int_{-\infty}^{\infty} S(\alpha)\, d\alpha = 1 \qquad ; \qquad \alpha \cong \Delta\lambda / F_o \qquad (5\text{-}2,3)$$

With wavelength in $\overset{o}{A}$ units, the normalized field-strength: $F_o = 1.253 \times 10^{-9} n_e^{2/3}$

In Griem's book (4) calculated values for the reduced Stark broadening parameters $S(\alpha)$ for the Balmer lines are tabulated for various electron densities and temperatures. The $S(\alpha)$ corresponding to intermediate electron densities were found by log-log interpolation. A correction for temperature was not required because the temperature dependence of these parameters is weak, and the $S(\alpha)$ for 10,000 K and 20,000 K are given by Griem.

Starting with an assumed n_e, we calculate the line width $w = 2\Delta\lambda$ corresponding to the value for α given in Griem's tables, and measure the relative intensity $V(\Delta\lambda)$ on the experimental line profile. For each assumed value n_e for the electron density we thus obtain a set of parameters $\left\{S[\alpha(\Delta\lambda)]/V(\Delta\lambda)\right\}_n$, and by iterating over n_e we find the best fit between the measured line shape and the Stark profile, according to the condition:

$$(S/V)_n = const = S/V \approx F_o/A \qquad (5-4)$$

The index n refers to the position on the line profile, and is conveniently expressed as the (apparent) fractional line width: $n \equiv V(\Delta\lambda) / V_o$

TABLE III

COMPARISON OF MEASURED LINE SHAPES WITH THEORETICAL STARK PROFILES

A) Balmer H_δ

a) n_e (assumed) $= 7 \times 10^{14}$ cm^{-3} ; $F_o/A = 0.74$

V/V_o	0.19	0.39	0.53	0.71	0.78	0.88	1
S/V	0.63	0.64	0.66	0.67	0.70	0.73	0.51

b) n_e (assumed) $= 8 \times 10^{14}$ cm^{-3} ; $F_o/A = 0.80$

V/V_o	0.17	0.37	0.51	0.68	0.78	0.89	1
S/V	0.71	0.70	0.71	0.71	0.75	0.75	0.51

c) n_e (assumed) $= 1 \times 10^{15}$ cm^{-3} ; $F_o/A = 0.94$

V/V_o	0.28	0.43	0.61	0.71	0.77	1
S/V	0.91	0.81	0.78	0.79	0.58	0.51

B) Balmer H_γ

n_e (assumed) $= 7.5 \times 10^{14}$ cm^{-3} ; $F_o/A = 0.48$

V/V_o	0.07	0.14	0.30	0.38	0.43	0.52	0.60	1
S/V	0.44	0.44	0.44	0.44	0.46	0.44	0.42	0.52

The results of the line-shape measurements corresponding to the arc at

30 Amps. at reduced pressure, are presented in Table III. In the case of H_δ,

the agreement of the S/V values for small n, corresponding to the line wings,

clearly favors an electron density around 8×10^{14} cm^{-3} over values which are

about 20% higher or lower. The shape of the wings of the concurrently measured

H_γ line is consistent with a theoretical Stark profile for $n_e = 7.5 \times 10^{14}$ cm^{-3}.

The narrow peak of this line is depressed due to self-absorption and distorted

by instrumental broadening, leading to a value for S_o/V_o that is too low.

The opposite effect occurs for the H_δ line whose narrow central dip predicted

by theory is smeared out due to instrumental broadening.

These results could not be verified by an independent determination of the

electron density. In our measurements of the center region of the low-current

arc at atmospheric pressure, however, the intensity of the continuum could be

used for such a check. In this plasma, the concentration of hydrogen and oxygen

atoms is too low to be of significance, and the continuum radiation is then prac-

tically identical to that of a pure argon plasma at the same temperature. The

spectral radiance of the continuum at wavelength λ is thus represented by a simple

formula

$$N_\lambda \text{ (cont.)} = C \frac{n_e^2}{T_e^{1/2}} \frac{\xi(\lambda,T)}{\lambda^2} \tag{5-5}$$

C is a known constant, the ξ-factor – which is only weakly temperature dependent –

accounts for departures from hydrogenic behavior and quantum-mechanical (Gaunt)

corrections. Based on the ξ-factors determined by Wende (30), and with $T_e = 9300K$

we obtain $n_e = 6.3 \times 10^{15}$ cm^{-3} from the measured continuum intensity at two

wavelengths: 3090 $\overset{o}{A}$ and 4370 $\overset{o}{A}$.

In this plasma the higher excited states of argon are in equilibrium with ions and free electrons. The Saha equation can then be used to determine the electron density from measured line intensities, since the concentration of argon ions and of electrons are practically equal. Thus $n^*(j)$, the measured number density of the upper state for Ar I 4300 $\overset{o}{A}$ yielded: $n_e = 5.5 \times 10^{15}$ cm^{-3}. The electron density determined from the shape of H_γ and H_δ in this experiment was: $n_e = (6.0 \pm 0.5) \, 10^{15}$ cm^{-3}. Within the probable experimental error, all three methods yield essentially the same electron density.

C.   Measured Population Distributions over Atomic Energy Levels

In addition to the Balmer series of hydrogen from H_α to H_δ (the higher members were too weak for precise measurements), several O I lines were measured. The transition probabilities were taken from the critical compilation by Glennon and Wiese (31). Concurrent emission and absorption measurements of a line yielded the population distribution between the two energy levels involved, characterized by the distribution temperature T_D (see Section 2A). However, most of these measurements were energy limited, and in the case of the oxygen lines wider slits had to be used than permissible for a measurement of the true line shape. Only when the measured absorptance was below, say, 0.30 did we derive the integrated line radiance by correcting the emission line for self-absorption in order to obtain $n(j)$, the occupation of the upper energy level. It is then preferable to use multiplets for a concurrent measurement of $n(j)$ and $n(i)$. The line strength ratio of the multiplet components is accurately known from theory, and a weak line in the multiplet can then be used to obtain $n(j)$, and a strong line - for which α is significantly higher - to derive T_D leading to $n(i)$.

48

a) <u>The Low-Current Arc at Atmospheric Pressure</u>: The absorptances of the lines belonging to the oxygen triplet at 7773 Å (multiplet # 1 in Moore's notation, Ref. 32) were of a convenient magnitude ($\alpha = 0.57$ for the strongest, and $\alpha = 0.28$ for the weakest line) for a concurrent measurement of $n(j)$ and $n(i)$. In the peripheral zone of the arc, the absorptance of H_α was high enough for a determination of the occupation of the first excited state of hydrogen. The other measured Balmer lines were practically optically thin.

The results for hydrogen and oxygen are presented in Fig. 13 in the form of a Boltzmann plot. The downward curvature of the plots corresponding to the higher energy levels in the off-axis measurements, is a clear indication of departures from equilibrium.

In order to determine the occupation of excited Ar I levels, we measured the intensity of Ar I 4300 Å, and of three other Ar I lines in the same wavelength region. The differences in energy terms are so small that these additional lines are only useful for a check of internal consistency. Based on Wende's value of 3.1×10^5 s^{-1} for the transition probability of Ar I 4300 (33), and using $T_e = 9300$ K for the small temperature correction, we can express the results of these intensity measurements at the arc center in the form of a set of calculated transition probabilities for these lines: Ar I 4333: 4.9 (4.8) ; Ar I 4335: 2.9 (2.9) ; and Ar I 4345: 2.3 (2.2) $\times 10^5$ s^{-1}. The agreement with Wende's values, indicated in parentheses, is excellent.

In the temperature range of interest, the fractional ionization of argon, oxygen, and hydrogen, is almost identical:

$$[Ar^+] / [Ar] = F(T_e) / n_e \approx [O^+] / [O] \approx [H^+] / [H] \qquad (5\text{-}6)$$

The equilibrium composition of an argon plasma is thus not disturbed by the additions of small amounts of water vapor. As seen previously, in our measurements of the arc center three independent methods had yielded essentially the same electron density, which is practically equal to the concentration of argon ions. The occupation of a highly excited state of the ion was determined by a measurement of the absolute intensity of the strong Ar II 4348 $\overset{o}{A}$ line. The recorded line was barely above the noise level, but in this temperature range its intensity is a very steep function of temperature and relatively large errors in the measured intensity do not affect significantly the derived temperature. We thus obtained T_D = 9300 K for the population distribution between the ion ground state and the upper state of this line. This is close to the temperature of 9000 K obtained from the Boltzmann plot for the population distribution over the hydrogen and oxygen energy levels (Fig. 13).

The population density of the argon ground state is practically equal to the total number of particles at P = 1 atm and T_g = 5000 K (see Section 5E), as given by the ideal gas law. Thus one derives a distribution temperature of 8800 K with respect to the population distribution between the ground state and the upper energy level for the Ar I 4300 $\overset{o}{A}$ line.

Based on these measurements it can be concluded that in the center of the arc the excited states of the atoms are in Saha equilibrium with their ions and the free electrons at an electron temperature of about 9300 K. If small departures occur, they are not significantly larger than the probable measurement error. The ground state of argon appears to be slightly overpopulated, however.

The electron density in the plasma region corresponding to the arc periphery was determined by the method of Section 5B, using H_γ as the diagnostic line. A good fit was obtained for the wings of the measured line shape and the theoretical

Stark profile corresponding to an electron density of 2.5×10^{14} cm^{-3}. In order to obtain the distribution temperature over highly excited states of the argon atom, we calculate first via the Saha equation the state population $n^*(\infty)$ corresponding to the energy level of the atom which coincides with the reduced ionization energy E_∞ (see Section 7). We can write the Saha equation, with $[Ar^+] = n_e$:

$$\log n^*_{Ar}(\infty) = 2 \log n_e - \log Q(Ar^+) - 1.5 \log T_e - 15.684 \qquad (5-7)$$

Eq. 5-7 was evaluated with $T_e = 7800$ K. The temperature dependence of the partition function for argon ions is so weak, that $Q(Ar^+)$ can be taken as constant over the relevant temperature range. We thus obtain a distribution temperature $T_D = 3200$ K for the population distribution between the energy levels joining onto the continum and the upper state of the Ar I 4300 Å line, whereas the population distribution between the latter and the argon ground state is characterized by a distribution temperature of 7600 K. The distribution over the argon energy levels follows therefore the pattern found for hydrogen and oxygen (see Fig. 13).

The magnitude of the distribution temperature characterizing the population distribution over the higher excited atomic states is of crucial importance for the interpretation of the mechanism bringing about the noted departures from LTE. Even assuming an error of 30% in the determination of the electron density - which appears unduly pessimistic - the distribution temperature found in the case of argon would still be below 3600 K. The measured population distribution between the 4th and 5th energy level of hydrogen corresponds to a distribution temperature of 2900 K. These distribution temperatures are definitely lower than the kinetic temperature of heavy particles (see Section 9C).

b) <u>The High-Current Arc at Reduced Pressure</u> (Arc core at 30 Amps. and 22 Torr):
The absorptance of the first two Balmer lines was too high for a direct determination
of $n(3)$ and $n(4)$, but the distribution temperatures $T_D(2-3)$ and $T_D(2-4)$ were
obtained with good precision by the emission-absorption method. The measured
absorptance of H_γ was of a convenient magnitude to determine the occupation of
both, the upper and the lower energy level for the transition. With $n(2)$ thus
measured, the previously determined distribution temperatures yielded the values
for $\log n^*(3)$ and $\log n^*(4)$ shown in parentheses in Table IV. The absorptance of
H_δ could not be measured accurately, but was certainly less than 0.20. The cor-
rection for self-absorption of the integrated line intensity amounts then only to
a few percent, and this line can be considered optically thin.

TABLE IV

THE BALMER HYDROGEN LINES

line	λ_o (Å)	Principal Q.N. upper(j)	lower(i)	$\log n^*(j)$	α	T_D (K)	$\log n^*(i)$
H_α	6563	3	2	(10.73)	1	6400	
H_β	4861	4	2	(9.80)	0.81	5300	
H_γ	4340	5	2	9.23	0.32	4800	12.22
H_δ	4102	6	2	8.83			

The gas temperature T_g = 5700 K was derived from a measurement of rotational
line intensities, and we assume that the chemical composition of the plasma is
given, effectively, by 2 H + O. The occupation of the hydrogen ground state
is then obtained from the ideal gas law, since the population of excited states
is insignificant. The contribution of other species (e.g. OH and O_2) to the

52

plasma composition can certainly be disregarded in this context, but it is quite possible that the ratio of hydrogen to oxygen atoms is less than 2:1 in the arc center.

The measured number densities are shown in Fig. 14 in the form of a Boltzmann plot. It is readily seen that the population distribution over the hydrogen energy levels is far from equilibrium.

The absorption measurements of the oxygen atoms (Table V) showed the three lines belonging to multiplet # 1 of O I to be black ($\alpha = 1$). This followed already from the emission measurements: The three lines were of the same intensity although their line strength ratio is 1:1.67:2.33. Since $E_j(\#1) = E_i(\#10)$, and the occupation of the latter was obtained by an emission-absorption measurement of multiplet # 10, we could derive $n(i)$ of # 1.

TABLE V

THE OXYGEN LINES

Multiplet # (32)	λ(Å)	$E_j(cm^{-1})$	Pg.	$E_i(cm^{-1})$	Pg.	log n*(j)	α	T_D(K)	log n*(i)
			a)	Quintets (Spin = 2)					
10	6158	102865	^4S	86631	^4S	8.62	0.198	5370	10.51
1	7772	86631	^4S	73768	^4S		≈ 1	4800	12.18
3	3947	99095	^4S	73768	^4S	9.11			
			b)	Triplets (Spin = 1)					
5	4368	99680	^4S	76795	^4S	9.59			
35	7947	113714	^2D	101135	^2D	8.24	0.30	5700	9.64
55	7476	127282	^2P	113910	^2P	7.46	<0.10	high	
			c)	Singlets (Spin = 0)					
38	7157	116631	^2D	102662	^2D	8.65	0.53	5650	10.19
65	6653	130943	^2P	115918	^2P	7.94	<0.10	high	

(Pg. = parentage of term)

53

The Boltzmann plot for oxygen is shown in Fig. 15. It should be noted that the high distribution temperature for those energy levels of O I that lie above the lowest ionization potential $[E(j) > E_\infty(^4S)]$, is also borne out by the absence of measurable absorption for multiplets # 55 and # 65.

D. High-Resolution Measurements of the Q_1-6 (0,0) Line and its Satellite

As noted before, the available background sources were unsuitable for absorption measurements of the rotational lines of OH, and we resorted to the "two line method", whose theoretical basis has been presented in Section 2A. The Q_1-6 (0,0) line was chosen because it is one of the strongest lines in the ultraviolet spectrum of OH and because the wavelength separation between main and satellite line and their line strength ratio are both of a convenient magnitude. The calculated strength ratio of 12.6 was experimentally verified in run E (see Table VIII), where self-absorption was negligible.

In order to achieve the required high spectral resolution, some compromise had to be made concerning the spatial resolution. An aperture of f/120 was chosen as compared to f/300 used in the "pinpoint" measurements described in Section 4. In these measurements of the arc at reduced pressure, the regions of observation corresponded to arc zones of relative uniformity - at least with respect to the intensity of the rotational lines - by focusing on the arc center (r = 0), and on the location of the off-axis peak (r = 1.1 mm) shown in Fig. 11. We also made measurements close to the arc periphery (r = 1.7 mm),

although in this case only average values over an inhomogeneous region were obtained.

At the narrow slit-widths required for these high-resolution measurements, the calibration signal from the strip lamp is so weak, that it is completely buried in noise. Hence advantage is taken of the fact that the measured integrated line intensity of an isolated line is independent of the slit function. Thus we used I_L of the Q_1-6 line as determined with wide slits (100μ for the entrance, and 400μ for the exit slit), in turn, for the radiance calibration of the narrow slit ($25/25\mu$) measurements. By focusing on the arc center we ensured that the slightly increased field of view in the calibration measurements - determined by the wider entrance slit - still corresponded to a relatively uniform arc zone.

The spectral resolution was determined experimentally by a concurrent scan of the hyperfine structure of Hg I 3125 $\overset{\text{o}}{\text{A}}$ under identical conditions as to aperture and slit widths. In order to improve the signal-to-noise ratio, the slit height was increased to 5 mm, but this can affect the resolution only adversely. The attained resolution, as determined by the half widths of the hyperfine components, closely checked the calculated resolution of 8 m$\overset{\text{o}}{\text{A}}$ (i.e. a resolving power of almost 400,000).

In Fig. 16 we show the spectrum recorded in scan # 2 of Table VI. The calculated Gaussian of the same half width hw' and normalized at the line peak, fits the recorded line shape of the Q_1-6 line very well, even out into the wings. Hence the contribution of a Lorentzian to the line shape has to be small, and it can be concluded that pressure broadening (including Stark broadening by charged particles) is negligible as compared to Doppler broadening. In all experiments,

including the measurements at atmospheric pressure, the recorded profiles of this line were always true Gaussians. This result cannot be simply generalized for all rotational lines of this band system, however. Pressure broadening may be more important for the higher rotational lines (34)

Thus the only broadening mechanisms that have to be considered in the case of the Q_1-6 line are Doppler and instrument broadening. However, since hw' is about 5 times larger than the spectral slit width, the correction for instrument broadening is only of the order of 5% [*], i.e. of the same order as the estimated measurement error. The correction for self-absorption is considerably more important. First the peak absorptance was obtained from the measured peak intensity ratio I'_o / I''_o , and then α_o was used to determine the fractional line height corresponding to the true half width hw (see Section 2A). The results of our measurements are summarized in Table VI.

It can be seen that hw, the true half width of the unabsorbed Q_1-6 line, as obtained from the recorded line shape, practically equals hw' of the satellite line (which is not self-absorbed, and therefore hw' = hw). Since the weaker line is noisier, hw (Q_1-6) was used to calculate the Doppler temperature, i.e. the kinetic temperature of heavy particles or gas temperature T_g.

The source function - derived from the measured peak intensity I'_o and the calculated α_o of the Q_1-6 line - yielded T_D(exc), the distribution temperature for the $A^2\Sigma$ excited electronic state and the $X^2\Pi$ ground state of OH.

---

[*] The square of the half width of a convolution of two Gaussians equals the sum of the squares of the half width of the components.

TABLE VI

RESULTS OF HIGH-RESOLUTION MEASUREMENTS OF THE Q_1-6(0,0) LINE AND ITS SATELLITE

Scan #	1	2	3	4	5
Arc current (Amp.)	50	50	50	15	15
Plasma Pressure (Torr)	20	20	20	18	18
Radial arc zone (mm off center)	0	1.1	1.7	0	1.7
$I_o(Q_1\text{-}6) / I_o(Q_{21}\text{-}6) = I'_o / I''_o$	11.55	9.7	7.65	8.1	6.1
Peak absorptance α_o	0.18	0.43	0.68	0.63	0.82
Distribution Temperature $T_D(exc)$ (K)	10,500	9,700	8,200	9,250	6,900
Q_1-6: Apparent halfwidth hw' (m$\overset{o}{A}$)	47	43.5	44.5	47	40.5
True halfwidth hw (m$\overset{o}{A}$)	43.5	40	36.5	39.5	31
Q_{21}-6: Apparent halfwidth hw' (m$\overset{o}{A}$)	45	40	37	41	31.5
Doppler temperature T_g (K)	6,500	5,500	4,600	5,400	3,300
$T'_{rot}(0,0)$ (K)	5,600	4,900	4,200	4,700	3,750
$T_g / T'_{rot}(0,0)$	1.16	1.12	1.09	1.15	0.9
$p(0,0) \times 10^4$ ("cm")	0.36	0.32	0.30	0.40	
$\log P^o_o + \log n^*(A,0,0)$	14.67	14.89	14.61	14.95	14.41
$\log P^o_o + \log n^*(X,0,1)$	16.59	16.97	17.07	17.13	17.34
$\log Q(OH)$	3.27	3.14	3.03	3.14	2.95
$\log P^o_o + \log [OH]$	19.86	20.11	20.10	20.27	20.29

In order to determine the distribution over rotational states, the integrated intensities I_L of the adjacent P_1-2 and R_1-20 lines of the 0,0-band were also measured ("wide slit" measurements, see Section 6A). Since the (undistorted) line shapes and the source functions for all three lines are practically indentical, the peak absorptance of the Q_1-6 line was used to correct these I_L for self-absorption, yielding N_L (i.e. the integrated radiance of the optically thin line). We thus obtained an "apparent rotational Boltzmann plot " for each of the five scans. These plots are strictly linear, which is not at all the case if the uncorrected I_L are used. The consistency between the derived $N_L(P_1-2)$ and $N_L(Q_1-6)$ is indicative of the precision of our method of correcting for self absorption. The correction factors covered a relatively wide range; thus for scan # 2: Q_1-6: $N_L = 1.19\ I_L$; P_1-2: $N_L = 1.05\ I_L$, and for scan # 5: Q_1-6: $N_L = 1.51\ I_L$; P_1-2: $N_L = 1.12\ I_L$.

In all scans except # 5, the gas temperature is higher than T'_{rot} derived from the "apparent Boltzmann plot". This result can clearly not be attributed to an underestimate of instrumental broadening, because then one would expect the ratio T_g/T'_{rot} to increase with decreasing hw, whereas the opposite is found.

As discussed in Section 6D, the relative strengths of the rotational lines of a band are not simply given by the Hoenl-London factors - which were used here for the apparent Boltzmann plot - but probably show also a slight exponential dependence on the rotational energy term. It follows that the difference between the reciprocals of the "apparent rotational temperature" and the gas temperature should be a constant (Eq. 6-6). In effect, when we evaluate $p(0,0) \equiv 1/kT'_{rot} - 1/kT_g$ we obtain for the first four scans an approximately constant value of $p(0,0) \approx 0.36 \times 10^{-4}$ "cm" (This unit appears because the energy term is expressed in cm^{-1})

The diverging result for scan # 5 is attributed to the spurious effect of plasma inhomogeneity. This measurement corresponds to a region of relatively steep radial temperature gradients, and in the averaging involved in the wide-slit measurements used to derive T'_{rot}, the regions of higher temperature will be more strongly weighted. The probable error in the Doppler temperature is also largest for scan # 5 because of the large correction for self-absorption, the higher level of experimental noise, and the greater sensitivity of T_g (which is proportional to the square of the half width) to small measurement errors.

By extrapolating the Boltzmann plot to $K = 0$, we obtain P_o^o $n*(A,0,0)$, i.e. the occupation of the vibrational-rotational ground state of the $A^2\Sigma$ electronic state of OH, times the molecular constant called here P_o^o and defined by Eq. 2-31. The measured distribution temperature $T_D(exc)$ yields then P_o^o $n*(X,0,1)$. The occupation of the ground state of OH (lowest vibrational-rotational level of the $X^2\Pi$ electronic ground state) is related to [OH], the total concentration of OH in the plasma, via the partition function.

Because of the large gap between the energy terms for the X and A electronic states, the contribution of the A state to the partition function is negligible even at the highest $T_D(exc)$ measured here. The population distribution over the vibrational-rotational levels of the electronic ground state is determined by the gas temperature, and T_g was used to evaluate $Q(OH)$. In run # 5 we estimate $T_g \approx 4100$ K.

A shown in Table VI, the concentration of OH is practically constant in scans #2 to #5, and only slightly lower in the center of the high-current arc. This important, albeit rather unexpected result, clearly demonstates that the concentration of OH in the plasma is not determined by the local values of T_g

or $T_D(exc)$, and can only be understood when the dissociation-recombination process in the plasma is analyzed on the microscopic level (Sections 9A and 10B).

With $\log P_o^o \approx 4.52$ (see Section 2B), the measured $\log [OH]$ is then of the order of 15.6 . For an equilibrium water vapor plasma at the same pressure, this concentration of OH corresponds to a temperature of about 3300 K (compare with Fig. 4 showing the equilibrium composition of a water vapor plasma at slightly lower pressure).

E.   Concentration of OH in the Arc at Atmospheric Pressure

The $p(0,0)$ correction factor obtained in the preceding Section was used to obtain the gas temperature from the "apparent rotational temperature" for the 0,0-band. Even in the peripheral zone, the noise level was too high for precision measurements at high spectral resolution. Based on the two line intensity ratio, the peak absorptance of the Q_1-6 line appears to be less than 0.10; $T_D(exc)$ is therefore certainly higher than T_g = 5000 K, but its exact magnitude could not be determined. The shape of the Q_1-6 line was measured with relatively wide slits $(50/50\mu)$, its profile is Gaussian and consistent with a Doppler temperature of the order of 5000K.

P_o^o $n*(A,0,0)$ was obtained by a measurement of the absolute intensity of the P_1-2 line. The population density of the $X^2\Pi$ ground state in the arc center is then estimated by setting $T_D(exc)$ = 9000 K $\approx T_e$, since the population distribution over the excited levels of atoms has been shown to be close to an equilibrium distribution at the electron temperature. For the plasma corresponding to the peripheral arc zone we calculate P_o^o $[OH]$ with $T_D(exc)$ = 7800 K (i.e. the distribution temperature corresponding to the linear portion of the atomic Boltzmann plots, and presumably the electron temperature), and also with $T_D(exc)$ = 6000 K. We then obtain the occupation of the OH ground state by using again $\log P_o^o$ = 4.52.

In equilibrium, the occupation of the ground state of OH, of O, and of H are related by the mass action equation:

$$\frac{n_O^*(1)\ n_H^*(1)}{n_{OH}^*(1)} = \left(\frac{2\pi\ m_H\ kT}{h^2}\ \frac{16}{17}\right)^{3/2} \exp\ (-D_o/kT) \qquad (5\text{-}8)$$

where $D_o = 35,501$ cm^{-1} is the dissociation energy of OH. The first factor on the right side of Eq. 5-8 contains the translational partition function, and consequently for this term $T = T_g$. The gas temperature also enters the exponetial term, since dissociation and recombination are predominantly induced by heavy particle collision (see Section 10A). Eq. 5-8 can be written in the following form, convenient for numerical computation:

$$\log n^*(X,0,1) = \log n_O^*(1) + \log n_H^* - 20.24 - 1.5 \log T_g + 20,200/T_g \qquad (5\text{-}9)$$

The occupation of the ground state of hydrogen and oxygen was obtained by extrapolating the respective Boltzmann plots (Fig. 13) to E = 0. The internal partition function - i.e. essentially the statistical weight of the ground state - times $n^*(1)$ yields then [H] and [O]. In both arc regions the ratio of hydrogen to oxygen atoms is practically 1:1, and not at all 2:1, as expected. For argon at 1 atm pressure, saturated with water vapor at room temperature, the ratio [H] : [Ar] = 2 [O] : [Ar] = 1: 21 is considerably higher than the measured ratio corresponding to the arc center. Both observations are strong evidence for arc demixing due to diffusion.

By substituting the derived occupation of the ground state of hydrogen and oxygen in Eq. 5-9, we determined the equilibrium occupation of the OH ground state shown in Table VII, where the results of these calculations are summarized.

TABLE VII

CONCENTRATION OF OH IN THE ARC AT ATMOSPHERIC PRESSURE

Arc region:	$r = 0$	$r = 1.1$ mm	
$T'_{rot}(0,0)$ (K)	4800	4400	
Gas temperature T_g (K)	5400	5000	
$\log P_o^o + \log n^*_{OH}(A,0,0)$	12.45	12.93	
Distribution temperature $T_D(exc)$ (K)	9000	7800	6000
$\log P_o^o + \log n^*_{OH}(X,0,1)$	14.69	15.51	16.29
$\log n^*_{OH}(X,0,1)$ ($\log P_o^o = 4.52$)	10.17	10.99	11.77
$\log [O] = \log n^*(1) + 0.96$	16.13	16.85	
$\log [H] = \log n^*(1) + 0.30$	16.11	16.73	
$[H] : [Ar] \approx [O] : [Ar]$	1 : 100	1 : 23	
$\log n^{*Eq}_{OH}(X,0,1;T_g)$	8.89	10.57	
$\log a_{OH}(X,0,1)$	1.28	0.42	1.20

In the last row of Table VII we show the overpopulation of the OH ground state with respect to an equilibrium occupation. Notwithstanding the inherent ambiguity in extrapolating the population distribution over excited states, the result of these calculations supports the conclusion that in the arc at atmospheric pressure the concentration of OH is also higher than the equilibrium concentration corresponding to the local values for the relevant temperature - the gas temperature - and the concentration of the dissociation products.

6. MEASUREMENT OF THE ULTRAVIOLET BANDS OF OH

A. Experimental

In view of the large number of lines to be measured, the standard procedure of obtaining the integrated line intensities by planimetering the area under each recorded line, would have increased the data acquisition and reduction time beyond tolerable limits. Since the rotational lines are quite narrow and of Gaussian shape, the intensity integration can be performed directly by the spectrometer without loss of precision. When a narrow entrance slit is used, and the exit slit is much wider than the half width of the line, the integrated line intensity is proportional to the amplitude of the recorded line trace (peak signal V_o). We determined experimentally that this condition was fulfilled for an entrance slit width of 0.1 mm and an exit slit width of 0.4 mm, and this was the setting used for the "Long Runs". By slowly scanning over various lines we determined the slit function at different grating angles for the two grating orders used (8th and 9th). We always found the area under the line to be equal to V_o x hw'. The half width of the line trace (hw') in chart units (cm) is a constant for each slit setting, and does not depend on grating angle or order.

By comparing the peak signal measured at the scanning speed used in the "Long Runs" (medium speed of the fine grating drive) with a slow scan, we established that pen overshoot does not occur. This prooved that the response time of the detection system (mainly determined by the time lag of the recorder pen) was faster than the time required to scan over a line. In order to ensure that only light emitted by an homogeneous plasma sample falls on the detector, the entrance slit was masked to a height of 0.25 mm and the imaging mirror (M_2 in Fig. 8) was stopped down to f/120.

The scan was started in the 9th grating order at the band-head of the $R_1(1,0)$ branch at 2811 Å and continued in the 8th order at 3160 Å. The strong excitation of the Schumann-Runge bands of O_2 precluded the measurement of OH lines beyond 3300 Å. The weak (0,1) band of OH could thus not be measured.

The scans were interrupted at regular intervals, and selected monitor lines were then scanned repeatedly in order to check for arc stability. The intensity variations were typically of the order of 5% with no notable difference between short-term and long-term stability. The repeatability was of the same order when the arc was restarted and the same experimental parameters were reproduced.

With the aid of Ref. 12 all lines in the spectrum were identified and assigned to the various transitions belonging to five bands of the $OH(A^2\Sigma - X^2\Pi)$ system. Only those lines were used for the data reduction whose peak-to-peak separation from an adjacent line is greater than about 0.2 Å, i.e., which are free from line-blending. We selected a total of 390 lines, distributed as follows: 0,0-band' (135 lines) ; 1,0-band (95 lines) ; 1,1-band (73 lines) ; 2,1-band (57 lines) ; 2,2-band (30 lines). In all scans the lines belonging to bands originating in the v' = 3 level - the 3,2 and 3,3 bands - were missing.

B. Results for the Main Branches

The measured integrated line radiances were reduced according to Eq. 2-25. N_L was divided by the appropriate line strength factor S/λ^4 , and the logarithm (base 10) of this quantity was plotted vs. the energy term of the upper rotational level. The data corresponding to the R, Q, and P branches of each band were plotted separately. Some representative Boltzmann plots are shown in Figs. 17 - 25. The quantity represented on the ordinate - called log y for simplicity - is defined by the relation:

$$\log y \;=\; \log (n*P) - 10.624 \qquad\qquad (6\text{-}1)$$

if n* is expressed in cm^{-3} and P in s$^{-1}\mu^{3}$.

All obtained Boltzmann plots show essentially the same pattern. Below the onset of predissociation the data points lie on a straight line, and within the experimental precision the log y values for the R_1 and R_2, the Q_1 and Q_2, and the P_1 and P_2 branches, respectively, are identical. In many cases the scatter is too small to be shown in the figure, and then we have drawn an open circle around the dot marking the data point. For the levels affected by predissociation a marked splitting occurs between the Boltzmann plot corresponding to the two spin components, and a different symbol has then be used for the weaker (i.e. underpopulated) f_1 level (see Figs. 17 - 25). Predissociation affects the occupation of states and is then better discussed in relation to the interaction proc--esses in the plasma (Section 10B), than in the present context where we are concerned with the transition probabilities for the rotational lines.

With the possible exception of the (1,0) band, discussed below, the log y values for all three main branches corresponding to lines originating in the same rotational state (i.e. also the same spin state if the level occupation is affected by predissociation), are identical within the precision of our measurements. This will be seen by comparing Figs. 17 and 18; and Figs 20 and 21, where the same Boltzmann plot has been drawn through the data points corresponding to the R and to the Q branches.

If a divergence between different branches does exist, it should increase with rotational quantum number (13, 14). A comparison of the data for the higher rotational lines is therefore especially significant. Unfortunately, the lines of high K were very weak because of predisssociation, and the experimental noise is proportionally higher. However, a data analysis showed the scatter to be random (see Fig. 19).

Systematic discrepancies between the Boltzmann plots belonging to different bands were found in some cases, but could then be traced to self-absorption. In run D of Table VIII the strong Q and P lines of the (0,0) band were significantly affected by self-absorption (see also Section 5D).

As another possible source of systematic errors, the variation of the instrument response with wavelength has to be considered. The response curve of the detector is known to be fairly flat over the wavelength region of interest, but increased reflection and absorption losses can be expected at wavelengths shorter than 3000 $\overset{o}{A}$. Although the optical elements are coated with magnesium fluoride, the total loss can be substantial because of the relatively large number of optical elements in the optical train.

Of greater significance yet is the efficiency loss of a grating used in higher orders with an increasing difference between grating angle and blaze angle, because an increasing fraction of the incident light is then diffracted into other orders and lost. Thus in the range 2811 to 2850 $\overset{o}{A}$, the intensity calibration showed an increase of $R(\lambda)$ of more than 1% per $\overset{o}{A}$, which is 7 times higher than the variation of the response in the range 2970 to 3100 $\overset{o}{A}$. This is to be expected, since the blaze wavelength for our grating in the 9th order is close to 3000 $\overset{o}{A}$.

The rapid variation of $R(\lambda)$ in conjunction with the previously described difficulties in obtaining an accurate intensity calibration at the shorter wavelengths, greatly increases the likelihood of error in our measurements of the (1,0) band - especially the R-branch - as compared to other bands. It must be admitted, therefore, that the small divergence resulting for the Boltzmann plots of the different branches of the (1,0) band (see Figs. 22, 23 and 24) may well be only spurious.

Below the onset of predissociation, the Boltzmann plots for the various
branches are well represented by/straight line, and the results of our measure-
ments are then best presented in analytical form by giving the equation of this
line, obtained by a least squares fit to the data points:

$$\log \bar{y} = \log y_o - m F(K')$$ (6-2)

where $F(K')$ is the rotational energy term in cm^{-1}, referred to the rotationless
state of vibrational level v'. In Table VIII the slope m is also expressed as
an "apparent rotational temperature" T'_{rot}.

TABLE VIII

RESULTS OF MEASUREMENTS OF THE MAIN BRANCHES

branch	$\log y_o$	$m \times 10^4$ (cm)	$T'_{rot}(K)$	Fig. #

Run A: P = 1 atm; I = 4.1 Amps.; Sample gas: argon saturated with water vapor
at room temperature. Arc region in focus: 1.1 mm off the arc center.

branch	$\log y_o$	$m \times 10^4$ (cm)	$T'_{rot}(K)$	Fig. #
(0,0)	2.304	0.1415	4400	17, 18
R(1,0)	1.318	0.1318	4700	
Q(1,0)	1.328	0.1468	4250	
(1,1)	1.738	0.1705	3650	
(2,1)	1.00	0.177	3500	
(2,2)	1.04	0.242	2500	

Run B: P = 18.2 Torr; I = 32.5 Amp. Sample gas: pure water vapor. Arc was
spatially scanned to maximize the intensity of Q_1-6(0,0)

branch	$\log y_o$	$m \times 10^4$ (cm)	$T'_{rot}(K)$	Fig. #
(0,0)	4.266	0.1260	4950	
R(1,0)	3.399	0.1090	5750	22
Q(1,0)	3.399	0.1282	4850	23
P(1,0)	3.373	0.1241	5000	24
(1,1)	3.726	0.1465	4250	
(2,1)	3.12	0.226	2750	25

TABLE VIII (cont.)

band	$\log y_o$	$m \times 10^4$	T'_{rot}	Fig. #

Run C-1: P = 18 Torr; I = 50 Amps., other parameters as in Run B.

band	$\log y_o$	$m \times 10^4$	T'_{rot}	Fig. #
(0,0)	4.122	0.1185	5250	19
(1,1)	3.62	0.134	4650	20, 21
(2,2)	3.04	0.316	2000	

Run C-2: Repeat of Run C-1

band	$\log y_o$	$m \times 10^4$	T'_{rot}	Fig. #
(0,0)	4.101	0.1135	5500	
(1,1)	3.587	0.133	4700	
(2,2)	3.05	0.275	2300	

Run D-1: P = 9.6 Torr; I = 18 Amps., other parameters as in Run B

band	$\log y_o$	$m \times 10^4$	T'_{rot}	Fig. #
(0,0)	4.295	0.1295	4800	
(1,1)	3.765	0.1495	4200	
(2,2)	2.99	0.256	2450	

Run D-2: Repeat of Run D-1

band	$\log y_o$	$m \times 10^4$	T'_{rot}	Fig. #
(0,0)	4.304	0.1291	4800	
(1,1)	3.717	0.141	4400	
(2,2)	3.01	0.276	2250	

Run E: P = 60 Torr; I = 50 Amps. Sample gas: mixture of argon and water vapor. Arc setting as in Run B

band	$\log y_o$	$m \times 10^4$	T'_{rot}	Fig. #
(0,0)	2.351	0.108	5800	
(1,1)	1.839	0.119	5200	
(2,2)	1.27	0.188	3000	

In run E an attempt was made to lower the concentration of emitters in order to minimize self-absorption. As shown in Table VIII, the intensity of the rotational lines was of the same order as in the run at atmospheric pressure with an argon matrix (run A), and about two orders of magnitude lower than in the other runs with pure water vapor at reduced pressure. However, the composition of the sample gas could not be well controlled, and the arc stability was adversely affected.

C. Results for the Satellite Branches

In general, the weak lines belonging to the R_{21}, P_{12}, Q_{21}, and Q_{12} satellite branches are too close to the corresponding line of the main branch for an intensity measurement with the wide bandpass used in the "Long Runs". The few favorable cases were used for a check of the theoretical Hoenl-London factors by comparing the intensities of satellite and main line. Although the effect of self-absorption on integrated intensities is smaller than on peak intensities, the strong lines will still be depressed. Only for relatively weak main lines will the intensity ratio be practically equal to the line strength ratio. The R_1-5 and R_1-20 lines of the (0,0) band fulfill this condition, since their intensity is typically 5 times lower than the intensity of the Q_1-6 line.

In various scans we measured the following intensity ratio between the R_1-5 and R_{21}-5 lines: 3.58 - 3.69 - 3.69 - 3.45 - 3.74 - 3.68 - 3.72 - 3.60 - 3.70. The average of these measurements is 3.65, which is very close to 3.63, the ratio of the Hoenl-London factors calculated with the coupling constant a = - 7.54. The results for the R_1-20 (0,0) line and its satellite are shown in Table IX. In this case the measured intensity ratio is also in good agreement with the line strength ratio calculated with the correct $a(K = 20) = - 9.0$ (see Section 2B).

TABLE IX

CALCULATED AND MEASURED LINE STRENGTHS OF R_1-20(0,0) AND ITS SATELLITE

		Line Strengths		
		R_1-20	R_{21}-20	Ratio
Calculated:	(a = - 7.55)	80.5	2.08	38.7
	(a = - 9.0)	80.8	2.72	29.7
Measured:	(Run # C-2)			30.5
	(Run # D-2)			29

The S(0,0) branch lies in a wavelength region where interference by other bands is small, and the first 12 lines are free from line blending. The higher lines form a bandhead, but S-19 could be measured again. This line at 3024.21 $\overset{o}{A}$ is not listed in Ref. 12.

The Hoenl-London factors calculated with the proper a(K) taken from Fig. 2, were used to reduce the intensity data for the S branch as explained in the case of the main branches. However, the representation of log y vs. F(K') does not follow a regular pattern. The experimental results are therefore presented in the form of a relative P-factor, by using the log $\bar{y}$ plot for the R-branch, i.e. the smoothed equivalent data obtained in the same run:

$$\log P'(S) \cong \log y(S,K') - \log \bar{y}(R,K') \qquad (6-3)$$

TABLE X

RELATIVE P-FACTORS FOR THE S-BRANCH

K'	S(K) x 8	log P'(S)			log P̄'(S)
		Run A	Run B	Run C	
1	0.75	0.040	0.037	0.027	0.035
2	1.20	0.005	0.004	0.004	0.004
3	1.39	0.004	0.014	0.013	0.010
4	1.44	0.027	0.027	0.035	0.030
5	1.42	0.024	0.059	0.011	0.031
6	1.38	0.037	0.041	0.024	0.034
7	1.32	0.014	0.034	0.020	0.033
8	1.26	0.038	0.057	0.020	0.039
9	1.20	0.059	0.053	0.054	0.055
10	1.14	0.084	0.074	0.039	0.066
11	1.09	0.049	0.064	0.065	0.060
12	1.05	0.050	0.078	0.094	0.074
19	0.89		0.028	-0.010	0.009

S(K) = Hoenl-London factor

D. The Transition Probabilities for OH ($A^2\Sigma - X^2\Pi$)

It follows from the linearity of the apparent Boltzmann plot that <u>both</u>, the occupation of the non-predissociating rotational levels and the P-factors depend exponentially on the rotational energy term: [*)]

$$n*(v',K') \quad = \quad n*(v',K'=0) \quad \exp\left[-F(K')/kT_g\right] \qquad (6-4)$$

$$P(q',q") \quad = \quad P_o(q',q") \quad \exp\left[-p(q',q")F(K)\right] \qquad (6-5)$$

---

*) The P-factor for the S(0,0) branch appears to be an exception.

71

For simplicity we use the notation q',q" to designate a particular branch of a band:

$$q',q" = v'K'J',v"K"J"$$

although the P-factors appear to be branch-dependent only for the (1,0) band. With the experimental data expressed as:

$$\log \bar{y} = \log y_o - m\,F(K') = \log y_o - 0.4343\,F(K')/kT'_{rot} \quad ,$$

the exponential factor is given by:

$$p = 1/kT'_{rot} - 1/kT_g = m/\log e - 1/kT_g \qquad (6\text{-}6)$$

The gas temperature was determined independently in the measurements reported in Section 5D, and by using Eq. 6-6, we obtained:

$$p(0,0) = 0.36 \times 10^{-4} \quad (\text{"cm"})$$

This value for $p(0,0)$ and the measured $m(0,0)$ were used to obtain the gas temperature for the "Long Runs". The exponential factors for the other bands were then derived form the measured slope of the apparent Boltzmann plots.

The concentration of OH in the plasma could not be determined, and it is then not possible to derive the absolute values for the P-factors. However, we can still obtain relative values by referring the P-factors to the molecular constant called here P_o^o and defined by Eq. 2-31.

$$P_o'(q',q") = P_o(q',q")/P_o^o = \frac{y_o(q',q')}{y_o(0,0)}\,\exp\left[G(v')/kT_g\right] \qquad (6\text{-}7)$$

where $G(v')$ is the vibrational energy term referred to the rotationless state of the lowest vibrational level. We assume here that the occupation of the non-predissociating vibrational levels is also in a Boltzmann equilibrium at the gas temperature. The results for the "Long Runs" are summarized in Table XI. The indicated average has been obtained by weighting the various runs according to their long-term stability and the possible influence of self-absorption.

TABLE XI

NORMALIZED TRANSITION MOMENTS FOR THE ROTATIONAL LINES OF OH ($A^2\Sigma - X^2\Pi$)

a) Measured Values

Run	T_g	$\log(1/P'_o)$ (1,0) R	Q	P	(1,1)	(2,1)	(2,2)	$p \times 10^4$ (cm) (1,0) R	Q	P	(1,1)	(2,1)	(2,2)
A	5000	0.611	0.601		0.191	0.57	0.53	0.04	0.49		1.03	1.18	2.68
B	5700	0.537	0.543	0.563	0.210	0.51		-0.03	0.41	0.34	0.83	2.66	
C-1	6100				0.194		0.49				0.71		4.90
C-2	6400				0.224		0.49				0.82		4.10
D-1	5500				0.190		0.64				0.82		3.28
D-2	5500				0.247		0.63				0.62		3.73
E	6800				0.236		0.55				0.61		2.20
Average			0.550		0.200	0.52		0	0.45	0.34	0.75	2.7	

b) Comparison with Calculated Values

branch q',q''	Franck-Condon factor $P'_o(q',q'')$ This work	D&C (12)	James (13)	A&L (14)	Exponential correction factor $p \times 10^4$ (cm) This work	James (13)	A&L (14)
R(0,0)	1	1	1	0.99	0.36	0.30	0.55
P(0,0)				1			0.48
R(1,0)	0.28	0.22		0.26	0.47	0	-0.73	0.13
Q(1,0)				0.46	0.45		0.20
P(1,0)			0.25	0.45	0.34	-0.53	0.26
R(1,1)	0.64	0.77		0.78	0.75		0.87
P(1,1)				0.79			0.65
(2,1)	0.30	0.40		0.69	2.7		0.38
R(2,2)	0.30	0.45		0.57	2.7		1.20
P(2,2)				0.60			0.79

73

In Table XIb the results of the present work are compared with theoretical predictions. Dieke and Crosswhite have calculated Franck-Condon factors neglecting the effect of vibration-rotation interaction and the variation of the electronic transition moment with internuclear distance (12). Anketell and Learner present tables of calculated relative transition probabilities for several lines of the band system (14). Although not noted in their paper, their data show an almost strictly exponential dependence on the rotational energy term, and are then better represented by the expression of Eq. 6-5. James' data for the (0,0) and (1,0) band (13) show only slight departures from an exponential dependence and can be approximated by an expression of the same form.

In run D-2 we measured the intensities of $P_2(2,1)$, and also of $R_2(2,2)$ and $Q(2,2)$ lines corresponding to high K'-numbers (14-18). Within the precision of our measurements of these weak lines, the log y values for the same K' were identical for the three branches. Since predissociation weakens different lines originating in the same upper energy level by the same amount, it must be concluded that the P-factors - and therefore also their dependence on the rotational energy term - are similar. This is contrary to Anketell and Learner's predictions (see Table XIb).

7. RATE PROCESSES IN PLASMAS

In electric discharges, collisions with electrons is the predominant mechanism for electronic excitation and for ionization. Provided the electrons have a Maxwell velocity distribution, the rates for a process induced by electron collision and its inverse are related by the principle of detailed balancing (9). Thus with the collisional excitation rate for a transition from energy level i into energy level j expressed in terms of the rate coefficients:

$$R_{col}(i,j) \equiv n(i)\, n_e\, X(i,j) \qquad (cm^{-3}\, s^{-1}) \quad , \qquad (7\text{-}1)$$

the following relation holds rigorously between the rate coefficient for excitation and for the inverse process (de-excitation from level j into level i), regardless of the equilibrium situation in the plasma:

$$n^{Eq}(j)\, X(j,i) = n^{Eq}(i)\, X(i,j) \qquad (7\text{-}2)$$

The ratio of the equilibrium populations of level i and j is given by the Boltzmann factor containing the electron temperature T :

$$\frac{n^{Eq}(j)}{n^{Eq}(i)} = \frac{g(j)}{g(i)}\, \exp\left[-(E_j - E_i)/kT\right] \qquad (7\text{-}3)$$

Similarly, for collisional ionization from level i, and three-body recombination into level i $(N_i$ = total concentration of ions of same species and next higher ionization stage, c = continuum):

$$R_{col}(i,c) = n(i)\, n_e\, S(i,c) \qquad\qquad R_{col}(c,i) = n_e^2\, N_i\, S(c,i) \qquad (7\text{-}4,5)$$

$$S(i,c)\, /\, S(c,i) = F(i,T) \qquad (7\text{-}6)$$

$F(i,T)$ is the Saha equation connecting the equilibrium population of energy level i and the concentrations of ions and free electrons, and Eq. 7-6 follows

from the principle of detailed balancing. Introducing the quantities $a(i)$ that relate the occupation of energy level i to its occupation in Saha equilibrium with the ions and free electrons (35),

$$a(i) = n^*(i) / n^{*Eq}(i) \quad , \qquad (7-7)$$

we have, as follows from Eqs. 7-4, 7-5, and 7-6,

$$a(i) = R_{col}(i,c) / R_{col}(c,i) \qquad (7-8)$$

In absence of equilibrium we find it advantageous to refer the Saha equation to $n^*(\infty)$, the occupation of the last bound state of the atom whose energy coincides with the reduced ionization energy E_∞. At the low electron densities typical for non-LTE plasmas, the lowering of the ionization energy is negligible, and one can set E_∞ numerically equal to the ionization potential of the free atom. The actual value of $i(\infty)$ does not concern us in this context. *) With $n^*(1,1)$ = number density of ions in the ground state; Z_e = total partition function of free electrons:

$$\frac{n_e \, n^*(1,1)}{n^*(\infty)} = Z_e = 2 \, (2\pi m_e kT/h^2)^{3/2} = 4.82 \times 10^{15} \, T^{3/2} \qquad (7-9)$$

$$n^{*Eq}(i) = n^*(\infty) \; \exp\left[(E_\infty - E_1)/kT\right] \qquad (7-10)$$

The true $i(\infty)$ state is a hybrid because of the mixing of the eigenfunctions for the bound and the continuous state of the same energy. Clasically, the rate coefficients pertaining to a transition from $i(\infty)$ into the continuum will be very large. Eq. 7-9 will therefore hold [i.e. $n^*(\infty) = n^{*Eq}(\infty)$], even when the occupation of the lower bound levels is not described by Eq. 7-10 [$a(i) \neq 1$]. The population distribution over bound levels (Boltzmann plot) must then converge to the $n^*(\infty)$ that is in equilibrium with ground state ions and free electrons.

---

*) For our low-pressure plasma: $i_H(\infty) \approx 50$ (see Eq. 6-38 in Ref. 4)

In principle, the rate coefficients for the various processes in the plasma can be obtained by averaging the appropiate cross-sections - which depend on the energy of the colliding electron - over a Maxwell velocity distribution. However, with the exception of hydrogen, accurate cross-sections are generally not available because experimental data are scanty and theoretical calculations are beset by considerable difficulties.

In optically thin plasmas, radiative decay and recombination are irreversible processes in the sense that photons can escape the plasma, and deviations from LTE can be expected if the rate for a collision-induced process is smaller or comparable to the rate for the equivalent radiative process. McWhirter and Hearn have obtained the population distribution over the hydrogen energy levels for this collisional-radiative plasma model by finding the steady-state solutions for the system of rate equations over a range of electron densities and temperatures (35). Their calculations for an optically thin hydrogen plasma with $n_e = 10^{15}$ cm^{-3}; $T = 16,000$ K - which is comparable to the electron density and temperature in our plasma at reduced pressure - predict significant departures from LTE only for the ground state, which will be overpopulated by a factor of the order of ten. The higher energy levels are in Saha equilibrium with the ions and free electrons, because the effectiveness of collisional processes relative to radiative processes is a rapidly increasing function of the principal quantum number (See next Section).

Fig. 14 shows convincingly that our experimental data cannot be reconciled with these theoretical predictions: The collisional-radiative plasma model is clearly not applicable to arc plasmas at reduced pressure.

77

8. ATOMIC SPECIES

A. Analysis of the Interaction Processes in Hydrogen Plasmas

The excitation rate coefficients for hydrogen have been given by Drawin (36), and are conveniently expressed in terms of the absorption oscillator strengths f_{ij}. Disregarding factors of the order of unity, and with $u_{ij} \equiv (E_j - E_i)/kT$; E_H = ionization potential of hydrogen:

$$X(i,j) = 8.7 \times 10^{-8} (E_H/kT)^{1/2} E_H/(E_j - E_i) f_{ij} \exp(-u_{ij}) U[u_{ij}] \quad (8\text{-}1)$$

$$U[u_{ij}] \equiv \ln[1.25(1 + u_{ij}^{-1})] / (1 + u_{ij}) \quad (8\text{-}2)$$

The collisional excitation rate from level i into level i + n, and the de-excitation rate for the inverse process can be written with $C(T) \equiv 1.7 \times 10^{-7} (E_H/kT)^{1/2}$;

$$R_{col}(i,i+n) \equiv n(i) \, n_e \, X(i,i+n)$$

$$= n^*(i) \, n_e \, C(T) \, I(i,i+n) \exp(-u_{i,i+n}) \, U[u_{i,i+n}] \quad (8\text{-}3)$$

$$R_{col}(i+n,i) \equiv n(i+n) \, n_e \, X(i+n,i)$$

$$= n^*(i+n) \, n_e \, C(T) \, I(i,i+n) \, U[u_{i,i+n}] \quad (8\text{-}4)$$

$$I(i,i+n) = f_{i,i+n} \frac{i^4 (i + n)^2}{n (2i + n)} = c \frac{i^5 (i + n)^5}{n^4 (2i + n)^4} \quad (8\text{-}5)$$

An expression given by Unsöld (37) has been used to relate the hydrogen oscillator strengths to the principal quantum number i. c is a slowly varying function of i and n, whose value ranges from 1.41 for $f_{1,2}$ to 1.85 in the limit of large i and n.

We wish to compare the probability of a collisional transition from level i into the two neighboring levels i ± 1 with the probability of a collisional transition into more distant levels. In this context, we can take c to be effectively constant and also disregard the ratio of the functions defined by Eq. 8-2, which is close to unity. Thus we obtain:

$$\frac{R_{col}(i,i+1)}{R_{col}(i,i+n)} \approx \left(\frac{i+1}{i+n}\right)^5 \left(\frac{2i+n}{2i+1}\right)^4 n^4 \exp(u_{i+2,i+n}) \tag{8-6}$$

$$\frac{R_{col}(i,i-1)}{R_{col}(i,i-n)} \approx \left(\frac{i-1}{i-n}\right)^5 \left(\frac{2i-n}{2i-1}\right)^4 n^4 \xrightarrow[i\to\infty]{} n^4 \tag{8-7}$$

It follows from Eq. 8-7 that a collisionally induced de-excitation from the third into the second energy level of hydrogen is about 200 times more probable than a transition into the ground state. This ratio decreases with increasing principal quantum number of the level involved, but even in the limit of high i, a de-excitation into the next lower level will be at least 16 times more probable than a transition into the level i - 2.

The ratio of the excitation rates into the adjacent and the next higher level, given by Eq. 8-6, contains the electron temperature via the exponential factor. For the higher quantum numbers this term is insignificant, and the limit for $i \to \infty$ is the same as for Eq. 8-7. The lower bound for Eq. 8-6 is 6, and corresponds to the probability ratio for excitation from the ground state to the second and to the third energy level in the limit of infinite temperatures. At $\sim$ 25,000 K, this ratio is larger than 10 for all energy levels of hydrogen.

Since transitions from level i into levels higher than i + 2 and lower than - 2 are still less probable, this analysis shows that the error introduced by considering only stepwise excitation and de-excitation is never serious.

The collisional ionization coefficients for hydrogen are given by Drawin as (36):

$$S(i,c) = 6.7 \times 10^{-8} (E_H/kT)^{1/2} i^2 \exp(-u_{ic}) \ U[u_{ic}] \qquad (8-8)$$

where $U[u_{ic}]$ is of the same form as Eq. 8-2, with $u_{ic} \equiv (E_H - E_i)/kT$. The ratio of collisional ionization to three-body recombination for each level i can then be calculated by using Eqs. 7-8 and 7-10.

Recombination can also occur by a two-body collision, in which the atom formed is stabilized by emission of a photon. The plasmas considered here are optically thin with respect to the recombination continuum, and the inverse process (photo-ionization) can surely be disregarded. The radiative recombination rate is given by (p = free protons):

$$R_{rad}(c,i) = n_e[p]\alpha(i) \qquad , \qquad (8-9)$$

and one obtains for the ratio of the probabilities of radiative and three-body recombination into level i:

$$\frac{R_{rad}(c,i)}{R_{col}(c,i)} = \frac{\alpha(i)}{n_e S(i,c)} \ F(i,T) \qquad (8-10)$$

$$= \frac{\alpha(i)}{i^4 \ U[u_{ic}]} \ \frac{2.3 \times 10^{30}}{n_e} \left(\frac{E_H}{kT}\right)^{-2} \qquad (8-11)$$

The radiative recombination coefficients are only weakly temperature-dependent, and were obtained by extrapolating to 25,000 K the $\alpha(i)$ tabulated by Bates and Delgarno (38).

Lastly, we consider depopulation of level i by radiative decay into lower levels:

$$R_{rad}(i,j<i) = n(i) \sum_{j<i} A_{ij} \approx 1.5 \times 10^{10} i^{-4} n*(i) \qquad (8-12)$$

The preceding concepts are now applied numerically to the water vapor plasma generated in the core of the high current arc at reduced pressure. In Table XII we compare the relevant population and depopulation rates for the first six levels of hydrogen, based on the measured electron density $(n_e = 8 \times 10^{14} \text{ cm}^{-3})$ and population distribution (Fig. 14). We also use $T = 25,000$ K, and $n^*(\infty) = 2 \times 10^7 \text{ cm}^{-3}$ (see Sections 8B & D).

TABLE XII

POPULATION AND DEPOPULATION RATES FOR HYDROGEN LEVELS IN THE LOW PRESSURE ARC

i	$\dfrac{R_{col}(c,i)}{R_{col}(i,c)}$	$\dfrac{R_{rad}(c,i)}{R_{col}(c,i)}$	$\dfrac{R_{rad}(i,j<i)}{R_{col}(i,i+1)}$	$\dfrac{R_{col}(i,c)}{R_{col}(i,i+1)}$	$R_{col}(i,i+1)$ $(\text{cm}^{-3} \text{ s}^{-1})$
1	7×10^{-7}	150	-	0.019	1.6×10^{21}
2	5×10^{-5}	0.81	2.7	0.175	2.3×10^{21}
3	7×10^{-4}	3.5×10^{-2}	3.5×10^{-2}	0.132	2.7×10^{21}
4	4×10^{-3}	4.3×10^{-3}	2×10^{-3}	0.095	2.8×10^{21}
5	1×10^{-2}	8×10^{-4}	3×10^{-4}	0.087	3.5×10^{21}
6	3×10^{-2}	2×10^{-4}	5×10^{-5}	0.071	4.9×10^{21}

The ratio of the collisional ionization rate for atoms in energy level i to the collisional recombination rate into this level equals $a(i)$, the overpopulation of level i (Eq. 7-8). As shown in the second column of Table XII, the ground state is thus overpopulated by more than 6 orders of magnitude with respect to the occupation of this level that is in Saha equilibrium with free electrons and protons. Three-body recombination into the

ground state is insignificant compared to ionization. Although radiative re-combination is larger by more than two orders of magnitude, it still is a very infrequent process compared to ionization. The probability for three-body re-combination increases rapidly with principal quantum number and becomes then much larger than the probability for the radiative process. But even for i = 6, recombination amounts to only 3% of the ionization rate.

Radiative depopulation is only important for the first excited level of hydro-gen, and radiative decay from this level into the ground state is about three times as probable as a collisionally induced transition into the next higher level. However, Lyman-α will be practically completely absorbed in the plasma, i.e. photo-excitation will balance radiative decay, and the net contribution of this process to the depopulation of the i = 2 level will then be much smaller.

With the exception of the levels i = 2, and i = 3, the probability for an hydrogen atom to be excited into the next higher level is at least ten times larger than the probability of a direct transition into the continuum. Although this may not be entirely correct for the second and third energy level, direct ionization can therefore also be disregarded as compared to the stepwise excitation and de-excitation process.

B. Population of Hydrogen Energy Levels by Stepwise Excitation

The steady-state occupation of level i is determined by equating the rates for transitions into level i to the rate of transitions out of level i. As seen previously, to a good approximation we can disregard all population and depopulation processes except transitions from and into neighboring levels induced by collisions with electrons. The rate equation for level i can then be written:

82

$$n(i-1)\, n_e\, X(i-1,i) + n(i+1)\, n_e\, X(i+1,i) = n(i)\, n_e\, [X(i,i-1) + X(i,i+1)] \qquad (8-13)$$

and, by applying the principle of detailed balancing:

$$n(i-1)\left[1 - \frac{a(i)}{a(i-1)}\right]X(i-1,i) = n(i)\left[1 - \frac{a(i+1)}{a(i)}\right]X(i,i+1) \qquad (8-14)$$

The quantities $a(j)$ were defined in Eq. 7-7. It should be noted that the ratio $a(j)/a(k)$ is a function of the electron temperature, but that $n^*(\infty)$ cancels. The expressions in square brackets in Eq. 8-14, for which we shall use a short-hand notation - e.g. $B(i-1,i)$ - denote the fraction of exciting collisions that are effective in populating the next higher level, taking into account the inverse process (de-exciting collisions into the lower level).

We have used the measured number densities and the appropiate rate coefficients calculated for $T = 18,000$; $20,000$; and $25,000$ K, to obtain the state occupation of the next higher level and compare it with the measured quantity. The ratios of the various factors in the expression for the rate coefficients (Eq. 8-1) were calculated separately, and are shown in Table XIII. Eq. 8-14 is then written as:

$$n^*(i) = n^*(i-1) \cdot \frac{I(i-1,i)}{I(i,i+1)} \frac{U(u_{i-1,i})}{U(u_{i,i+1})} \frac{\exp(-u_{i,i-1})}{\exp(-u_{i+1,i})} \frac{B(i-1,i)}{B(i,i+1)} \qquad (8-15)$$

TABLE XIII

IALCULATED OCCUPATION OF HYDROGEN ENERGY LEVELS IN THE CORE OF THE LOW-PRESSURE ARC

i-1	log $n_m^*(i-1)$	log $\dfrac{I(i-1,i)}{I(i,i+1)}$	log $\dfrac{U(u_{i-1,i})}{U(u_{i,i+1})}$	log $\dfrac{e^{-u}_{i-1,i}}{e^{-u}_{i,i+1}}$	log $\dfrac{B(i-1,i)}{B(i,i+1)}$	log $n_c^*(i)$	log $\dfrac{n_m^*(i)}{n_c^*(i)}$

a) Assumed electron temperature: T = 18,000 K

1	16.12	-1.522	-0.888	-2.327	0.013	11.40	0.82
2	12.22	-0.927	-0.436	-0.444	0.032	10.44	0.29
3	10.73	-0.675	-0.225	-0.099	0.081	9.81	-0.01
4	9.80	-0.530	-0.136	-0.039	0.088	9.19	0.04
5	9.23	-0.444	-0.092	-0.019	(0.174)	8.85	-0.02
6	8.83						

b) Assumed electron temperature: T = 20,000 K

1			-0.883	-2.095	0.024	11.64	0.58
2			-0.418	-0.309	0.036	10.57	0.16
3		see a)	-0.218	-0.089	0.080	9.83	-0.03
4			-0.132	-0.035	0.088	9.19	0.04
5			-0.080	-0.017	(0.178)	8.87	-0.04

c) Assumed electron temperature: T = 25,000 K

1			-0.862	-1.674	0.029	12.19	0.03
2			-0.389	-0.248	0.041	10.66	0.07
3			-0.195	-0.071	0.085	9.87	-0.07
4			-0.120	-0.029	0.082	9.20	0.03
5			-0.078	-0.013	(0.100)	8.83	0.00

Note: n_m^* is the measured, and n_c^* the calculated state occupation. The occupation of the energy level is given by $n(i) = 2i^2 n^*(i)$. Quantities in parentheses are based on an estimated occupation of the energy level $i = 7$.

The predicted population process is quantitatively confirmed by the excellent agreement between the measured and the calculated number densities, as shown in Table XIII. It should be noted that only the relative occupations of the second and third energy level depend significantly on the assumed electron temperature. The agreement is best for an electron temperature of the order of 25,000 K. The temperature can still be higher, however, if the assumption of complete trapping of resonance radiation does not hold. Although Eq. 8-15 will then yield too high an occupation number for the second energy level, this results from the neglect of radiative decay from the second energy level into the ground state.

The ratio of the exponential factors approaches unity for the higher energy levels, and the increase of the factor containing the U-functions is approximately cancelled by the slow increase in the ratio of de-exciting to exciting collisions expressed by the B-factor. The state occupation pertaining to energy level i is then mainly determined by the I-factor that depends only on the principal quantum number and for $i \rightarrow \infty$, increases as i^6. Thus n*(i) will fall rapidly with increasing principal quantum number i, leading to a downward curvature of the Boltzmann plot. The failure to detect experimentally any measurable lines in the series limit is consistent with this pattern.

C. Population Distribution over the Oxygen Energy Levels

The oxygen atom has a complex term scheme, and the collisional excitation rates are not available; it is therefore not possible to obtain the number densities by calculation, as in the simple case of hydrogen. However, the pattern of the measured population distribution, shown in Fig. 15, can be explained in a qualitative manner.

Collisional as well as optical transition probabilities are determined by the matrix element of the dipole - in general multipole - moment. If a transition between two energy levels is forbidden for optical dipole radiation, the probability for a transition induced by electron collision will also be very small. Intercombination lines between terms of different multiplicity are forbidden for oxygen (Russel-Saunders coupling), and measured collisional cross-sections involving a change of multiplicity are significant only at energies close to threshold.

A splitting between the Boltzmann plots for singlet, triplet, and quintet states can then be expected in a non-equilibrium plasma. This is, in fact, a notable feature of the population distribution shown in Fig. 15. Thus the $4p\ ^3P$ state at 99092 cm^{-1} is overpopulated by a factor of the order of three with respect to the adjacent $4p\ ^5P$ state at 99680 cm^{-1}. The next higher state - $3s'\ ^3D^o$ at 101135 cm^{-1} - lies practically on the same Boltzmann plot as the $4p\ ^3P$ state, although it is a state of different parentage. Combinations between states of different parentage but same multiplicity are not only allowed, but can be very strong.

Analagously to hydrogen, in this plasma the ground state and lower lying levels of oxygen are highly overpopulated with respect to the occupation that is in Saha equilibrium with oxygen ions and free electrons. The triplet ground state of O I is populated by dissociation of the $X^2\Pi$ and predissociation of the $A^2\Sigma$ state of OH. The low-lying metastable singlet state of O I ($2p^4\ ^1D$) will be populated mainly by dissociation of oxygen molecules, a substantial component of the plasma (see Section 10A). The quintet states of OI are formed by dissociation of the higher excited electronic states of O_2 and OH, which in this plasma have very small occupation numbers. This population mechanism can

lead to the observed overpopulation of the excited singlet states of oxygen with respect to the triplet states, which, in turn, are overpopulated with respect to the quintet states.

A shown in Fig. 15, the two Boltzmann plots for the doubly excited bound levels of oxygen of ^2P and of ^2D parentage cross undisturbed the energy threshold $E_\infty(^4S)$ for ionization into ground state ions. The measured distribution temperature is actually higher for the energy levels above $E_\infty(^4S)$. It must therefore be concluded that the probability for an oxygen atom in a doubly excited state to be excited into a higher bound level of same multiplicity is much higher than the probability of ionization into ground state ions.

The population distribution over bound states of ^4S parentage must converge to the occupation of the last bound state $n*[E_\infty(^4S)]$ that is in Saha equilibrium with free electrons and ground state ions (Section 7). This implies a sharp drop in the Boltzmann plot for the quintet states in the energy interval between $E_\infty(^4S)$ and the last measured occupation plotted in Fig. 15. It also implies a splitting between the Boltzmann plot for the higher excited triplet states of ^4S parentage and the Boltzmann plot for the triplet states of ^2D and ^2P parentage, since the point on the latter corresponding to $E_\infty(^4S)$ is higher than $n*[E_\infty(^4S)]$ by two orders of magnitude.

The splitting between Boltzmann plots corresponding to states of allowed combination, can be explained by the rapidly decreasing probability for transitions involving a quantum jump over more than one principal quantum number. The $(^2D)3s\ ^3D$ state, whose number density is plotted in Fig. 15, is the only triplet state of excited ion parentage below $E_\infty(^4S)$. The next higher doubly excited triplet states of principal quantum number 3, lie already around 113,500 cm^{-1}. The $(^2D)3s\ ^3D$ state is followed by closely spaced ^4S triplets with the valence electron

in levels with principal quantum number 4 and higher. Once an atom has been excited into these levels, it has a much higher probability of being further excited into an adjacent ^{4}S-triplet than of going into the high triplet states of ^{2}D or ^{2}P parentage. Transitions from these doubly excited triplets of low principal quantum number into the relatively underpopulated ^{4}S-triplets of high principal quantum number will, in turn, also be an infrequent process. This will lead to the predicted splitting of the Boltzmann plots.

When progressing to higher energies, the Boltzmann plot for the doubly excited triplet states will again show a drop before converging to the ionization limit for ^{2}D and ^{2}P. These excited ions can be formed by ionization of singlet and of triplet atoms, and a split of each Boltzmann plot is predicted and indicated qualitatively in Fig. 15.

The population distribution over oxygen energy levels is further discussed in Section 11.

D. Occupation of Energy Levels in the Ionization Limit

Since the concentration of molecule-ions in the water vapor plasma is negligible, and second ionization of oxygen can still be disregarded, the condition of plasma quasi-neutrality requires the electron concentration to be equal to the added concentrations of free protons and oxygen ions.

Thus: $[O^+] = x \, n_e$; $[p] = (1 - x) \, n_e$

where: $x \equiv \dfrac{[O^+]}{[O^+] + [p]}$ $0 < x < 1$

88

Protons do not have discrete energy states, but in order to obtain the occupation of ground state oxygen ions, we need the partition function, i.e. the population distribution for ions. Next to the statistical weight of the ground state $[g(1) = 4]$, the largest contribution comes from the low-lying meta-stable states, which are not likely to be in a Boltzmann equilibrium with the ground state (see Section 11). However, in view of the approximate nature of this calculation, the possible error introduced by using $Q_O^+ = Q_O^+(\text{Eq.},25000K)$ is not serious. With $n_e = 8 \times 10^{14}$ cm^{-3}, $T = 25,000$ K, the occupation of the last bound states of the oxygen and hydrogen atom is given by the Saha equation (Eq. 7-9) as:

$$\log n_O^*(\infty) = 6.69 + \log x$$

$$\log n_H^*(\infty) = 7.52 + \log (1 - x)$$

Considering the bounds for the ratio x, it can be seen that even for $[p] \ll [O^+]$, $n_O^*(\infty)$ is lower by an order of magnitude than the linear extension of the measured population distribution for the quintet states of oxygen, shown in Fig. 15. Conversely, even for $[p] \gg [O^+]$, the distribution temperature between the sixth energy level of hydrogen and E_∞ must be lower than the last measured distribution temperature of 2100 K.

In order to show the trend for the Boltzmann plot at high quantum numbers, as predicted by theory, we have arbitrarily set $x = 0.5$, based on the higher diffusion rate for protons and on the assumption of approximately equal rates of formation of oxygen and hydrogen ions.

9. MECHANISMS LEADING TO DEPARTURES FROM LTE IN ARC PLASMAS

A. Diffusion of Ground State Atoms and Ambipolar Diffusion of Charged Particles

The axial zone ("core") of the water vapor arc at high currents and reduced pressure is characterized by a large overpopulation of ground-state neutrals with respect to an occupation in equilibrium with their ions and free electrons at the electron temperature. The excitation and ionization rates greatly exceed the rates for the inverse processes, as follows from the principle of detailed balancing. Ions are therefore constantly formed, and ground state neutrals constantly lost, either by direct transitions into the continuum or by the step-wise excitation process. In order to maintain the plasma in a steady state, there must be a corresponding influx of ground-state neutrals and an outflow of ions and free electrons.

The distance an atom in energy level i can diffuse, on the average, before undergoing an exciting collision, is given approximately by:

$$d(exc,i) \approx \lambda \sqrt{\frac{t(exc,i)}{t_f}}$$

$$\approx \sqrt{\lambda \, \mathbf{v} \, t(exc,i)} \qquad (9\text{-}1)$$

where λ and t_f are the mean free path and the mean free time for elastic collisions, respectively, $\mathbf{v}$ is the root mean square velocity of the atom, and $t(ex,i)$ the free time for exciting collisions.

The pertinent elastic cross-sections are of the order of 10^{-15} cm^2. The kinetic temperature of heavy particles (gas temperature) in the core of the arc at reduced pressure has been determined as $T_g = 5600$ K. The diffusion length for hydrogen atoms is then estimated by:

$$d(exc,i) \approx 0.15 \sqrt{10^6 \, t(exc,i)} \quad (cm)$$

We have seen previously that in this plasma excitation of hydrogen atoms occurs mainly by a step-wise process. The average lifetime with respect to collisional excitation is then given by:

$$t(exc,i) = n(i) / R_{col}(i,i+1) \quad (s) \qquad (9-2)$$

Based on the measured number densities and the calculated collisional excitation rates (see Table XII), we obtain for the hydrogen ground state: $t(exc,1) = 1.6 \times 10^{-5}$ s ; $d(exc,1) = 0.6$ cm; and for the first excited state: $t(exc,2) = 5.7 \times 10^{-9}$ s; $d(exc,2) = 0.01$ cm.

Since the diffusion length for the hydrogen ground state is larger than the radius of the arc channel by a factor of the order of 3, it can readily be seen that diffusion of ground state atoms from the arc periphery will maintain the high overpopulation in the arc center. The concentration of atoms in the first excited state will not change significantly over a radius comparable to their diffusion length, and the level occupation will then not be sensibly affected by diffusion. Collisional lifetimes scale, at least, as the occupation of each level, and diffusion will still be less important for the higher bound levels.

In evaluating the free path for ions, ion-ion encounters also have to be taken into account. Although in this context one only has to consider strong collisions (i.e. those deflecting the scattered particle by more than 90°), the pertinent cross-sections are larger than ion-atom cross-sections by almost an order of magnitude. However, since this plasma is only 2% ionized, ion-ion collisions can still be neglected, and the mean free path for protons is then practically the same as for hydrogen atoms. This actually might involve an underestimate because of the correlation between the diffusion of ions and of electrons (ambipolar diffusion), that leads to a diffusion rate for the ions twice as large as for ordinary diffusion.

We can thus estimate the distance a free proton can diffuse in this plasma before recombining with an electron to form a hydrogen atom in level i, with:

$$d(rec,i) \approx 0.15 \sqrt{10^6\, t(rec,i)} \qquad (cm)$$

where:

$$t(rec,i) = \frac{[p]}{R_{col}(c,i)} = \frac{F(i,T_e)}{n_e^2\, S(i,c)} \qquad (9\text{-}3)$$

$$t(rec,i) = \left(\frac{10^{10}\, T_e}{i^2\, n_e}\right)^2 1\,/\, U(u_{ic}) \quad (s) \qquad (9\text{-}4)$$

We have used Eq. 8-8 that applies to the rate coefficients for collisional ionization, in order to derive the relation of Eq. 9-4, and it is then only valid for recombination into excited levels. Recombination into the ground state occurs predominantly by the radiative process (see Section 8A), yielding $t(rec,1) \approx 10^{-2}$ s. The lifetime of a free proton with respect to recombination into the second energy level is of the same order of magnitude. Because of the small probability for volume recombination into lower energy levels, a steady-state can be maintained with a large overpopulation of these levels compared to their equilibrium values.

Even for high quantum numbers, say i = 20, we obtain with $t(rec,20) = 10^{-7}$ s, a diffusion length of the order of 0.45 mm. A free proton formed in the arc core can thus be lost by ambipolar diffusion to the arc walls before recombining into these high energy levels.

Eqs. 9-1 and 9-4 yield the following approximate scaling law:

$$d(rec,i) \propto \frac{T_g^{3/4}\, T_e}{i^2 p^{1/2}\, n_e} \qquad (9\text{-}5)$$

92

Eq. 9-5 has been derived for hydrogen plasmas in the limit of negligible ionization, and has then only a restricted validity for other plasmas, but is useful for an order of magnitude estimate. Thus one can expect departures from the Saha equilibrium in a plasma due to ambipolar diffusion of ions and electrons,

$$\text{if:} \qquad \frac{1}{L} \frac{\rho_D^2}{N_t^{1/2}} < A \qquad\qquad (9\text{-}6)$$

where the ratio of electron temperature to electron density is expressed as the square of the Debye radius, N_t is the total concentration of particles, and L is a typical linear dimension of the plasma over which significant changes in the plasma state occur, i.e. L is a measure of the spatial inhomogeneity. A in Eq. 9-6 is not a constant, but depends on the plasma composition via the elastic cross-sections. Because of the larger ion-ion cross-section, A decreases with increasing degree of ionization.

It is of interest, to apply these concepts to the low-current water vapor arc in an argon matrix at atmospheric pressure. For the plasma in the arc core we obtain a diffusion length for proton recombination which is smaller by more than two orders of magnitude than the equivalent length in the case of the low-pressure arc. This explains why only mild departures from LTE were observed.

At the periphery of the atmospheric arc, the ratio of electron temperature to electron density is practically the same as in the core of the low pressure arc, and the respective diffusion lengths scale then only as $P^{-1/2}$, or 1:6. However, this plasma region corresponds to an arc zone of very steep gradients of electron density and temperature (i.e. L in relation 9-6 is very small), which will lead to a high probability for the ions to diffuse outward and recombine with electrons via wall-recombination. Thus we observed a "dropping-off" of the

Boltzmann plots for the excited states of argon and hydrogen entirely equivalent to our measurements of the center region of the arc at reduced pressure.

B. Electronic Excitation by Heavy-Particle Collision and Non-Maxwellian Velocity Distribution for Electrons

The author is not aware of prior similar work with arc plasmas at high currents and reduced pressure. Our measurements at atmospheric pressure, however, can be compared with experimental work by Kolesnikow, who has reported departures from LTE in low-current arcs burning in a mixture of argon and hydrogen at atmospheric pressure (39). He also observed a decrease of the distribution temperature over the higher excited states, but attributes this to an entirely different effect.

Kolesnikow argues that at low electron densities encounters with atoms - notwithstanding the much smaller cross-sections - can be more effective than electron collisions in inducing transitions between higher levels. The gas temperature in these plasmas is substantially lower than the electron temperature, and because of the threshold condition, the effectiveness of excitations induced by collisions with heavy particles will increase with a decrease of the energy jump involved in the transition. Thus excitation of atoms in the lower energy levels will still occur by electron collision because the energy gaps are much larger than the mean kinetic energy of heavy particles, but excitation by atom-atom collision should become progressively more important for the higher energy levels. One should then observe an assymptotic approach of the distribution temperature to the kinetic temperature of heavy particles.

Kolesnikow's interpretation of observed departures from LTE in arc plasmas at low electron densities appears to be generally accepted (6,40). It is however, irreconcilable with the results of more refined measurements.

In the peripheral zone of our arc at atmospheric pressure, the measured electron density was 2.5×10^{14} cm^{-3}, which is lower by a factor of about three than in the plasma of lowest electron density investigated by Kolesnikow. But even at the high ratio of atoms to electrons of the order of 5000, the observed departures from LTE are surely due to diffusion and not to excitation by atom collisions, since the measured distribution temperatures over the higher excited states of hydrogen and of argon are substantially lower than the gas temperature.

Atom-atom collisions can be more effective than electron-atom encounters, if the ratio of atoms to free electrons in the plasma fulfills the following condition (41):

$$\frac{N_a}{n_e} > \frac{1}{2}\left(\frac{m_a}{m_e}\right)^{3/2} f(1, T_e, T_g) \qquad (9-7)$$

The function f in Eq. 9-7 is determined by the specific energy dependence of the pertinent cross-sections, and is difficult to estimate for the range of interest, i.e. for a mean kinetic energy of the colliding particles much larger than the threshold. Since $T_e > T_g$, we assume that in this range f is not significantly smaller than unity. Electronic excitation by collision with atoms will then only become important if the concentration of atoms exceeds the electron density by a factor of the order of 5×10^4 in a hydrogen plasma - the most favorable case - and of the order of 10^6 in an argon plasma.

At atmospheric pressure and below, the electron densities required to maintain an arc discharge, are always higher than the critical density determined by this estimate, and it can be concluded that for arc plasmas electronic excitation by heavy particle encounters is probably always negligible.

Our treatment of the interaction processes in the plasma is based on the assumption of a Maxwell velocity distribution for the electrons. Equilibration of the velocity distribution occurs mainly by electron-electron interaction because this process is very efficient, and the pertinent cross-sections are large. The electron-electron relaxation time can be estimated, according to Spitzer (42), with:

$$t_{ee} \approx 0.03 \ T_e^{3/2} \ / \ n_e \qquad (s) \qquad (9\text{-}8)$$

which yields $t_{ee} \approx 1.5 \times 10^{-10}$ s for the plasma in the arc core at reduced pressure and $t_{ee} \approx 0.7 \times 10^{-10}$ s for the peripheral zone of the arc at atmospheric pressure and low current. These times are very short, much shorter than the recombination times (Eq. 9-4). Since electrons and ions diffuse together, and the ambipolar diffusion rate is determined by the slow-moving ions, the diffusion length for an electron in time t_{ee} will be small compared to typical arc dimensions. The velocity distribution of electrons will, therefore, be indeed Maxwellian, and a well defined electron temperature can be assigned to small radial zones of the arc.

Schlüter has attributed observed anomalies in spectras of high-frequency discharges to a Druyvestyn velocity distribution for the electrons, caused by diffusion of the energetic electrons from the tail of the Maxwell distribution (43). The theoretical treatment of this question is beset by considerable difficulties (36). No evidence for this effect has been found in the present work.

C. Lack of Equipartition of Kinetic Energy between Electrons and Heavy Particles

in the Plasma

So far we have only discussed departures from equilibrium with respect to
species concentrations and population distributions over quantized energy levels.
We now consider the lack of equipartion between the kinetic energy of electrons
and of heavy particles that leads to the observed discrepancy between the elec-
tron temperature T_e and the gas temperature T_g.

If the energy loss by inelastic collisions can be disregarded, in a steady
state the energy gained by an electron from the applied electric field in t_f ,
the mean free time between elastic collisions with heavy particles, must equal
the mean energy transferred by such a collision (44).

$$\Delta \varepsilon_+ = \frac{(Ee)^2}{2m_e} \, t_f^2 = 8.8 \times 10^4 \, E^2 \, t_f^2 \qquad \text{(eV)} \quad (9\text{-}9)$$

$$\Delta E_-(\text{el}) = \frac{3}{2} k \, (T_e - T_g) \frac{2m_e}{M} = 1.40 \times 10^{-7} \, (T_e - T_g)/A \quad \text{(eV)} \quad (9\text{-}10)$$

where temperatures are reckoned in K, and A is the atomic weight (mass number)
of the collision partner. In the numerical form of Eq. 9-9, the field strength
is expressed in V/cm. E is experimentally determined by measuring the voltage
drop along the arc channel (see Section 3C).

By setting $\Delta E_+ = \Delta E_-$, and with $t_f = \lambda_e / v_e$, we obtain the electron
free path with respect to elastic collisions with heavy particles:

$$\lambda_e = 8.5 \times 10^{-6} \frac{T_e}{E \, A^{1/2}} \left(\frac{T_e - T_g}{T_e} \right)^{1/2} \qquad \text{(cm)} \quad (9\text{-}11)$$

Eq. 9-11 was used to calculate $\lambda_e = 8.4 \times 10^{-4}$ cm from the measured data
corresponding to the plasma in the core of the arc at atmospheric pressure:

97

$T_e \approx 9300$ K, $T_g = 5400$ K, $E = 15$ V/cm. The chemical composition of the plasma is approximately 98% Ar with only 1% H and 1% O, but one has to use $\overline{A} = 28$ in Eq. 9-11, by properly averaging.

Since this plasma is only 0.2% ionized, we can disregard collisions with ions and set $\lambda_e^{-1} = \sigma_{ea} N_t$, yielding $\sigma_{ea} = 1.0 \times 10^{-15}$ cm^2. This agrees to better than 20% with measured elastic cross-sections of argon for collisions with slow electrons.

If the long-range interaction between charged particles is taken into account, the cross-sections for electron-ion encounters are much larger than for scattering by neutrals. For approximate calculations one can use an expression valid for all singly charged ions (42):

$$\sigma_{ei} \approx 3 \times 10^{-5} \, T_e^{-2} \qquad (cm^2) \qquad\qquad (9\text{-}12)$$

Thus at $T_e \approx 26,000$ K, the estimated electron temperature in the core of the water vapor arc at reduced pressure, $\sigma_{ei} \approx 5 \times 10^{-14}$ cm^2, which is 50 times larger than the cross section of hydrogen with respect to elastic collisions with electrons. At 2% ionization, the frequency of electron-ion and electron-atom encounters are about equal in this plasma. With the calculated $\lambda_e = 1.3 \times 10^{-2}$ cm, we obtain $t_f = 1.2 \times 10^{-10}$ s. The measured field strength was 26 V/cm. Thus, as given by Eq. 9-9, an electron gains 8.5×10^{-3} eV from the applied electric field in the free time between elastic collisions. However, with $(T_e - T_g) = 20,000$ K and $\overline{A} = 1.5$, the mean energy transferred to a heavy particle by an elastic collision is only of the order of 1.9×10^{-3} eV (Eq. 9-10). This is less than 25% of the energy gained from the field. The balance must then be dissipated by inelastic collisions.

In diffusion-controlled, non-equilibrium plasmas, the electrons lose energy by inelastic collisions, because excitation processes are not balanced by their inverse, i.e. collisions of the first kind are much more frequent than collisions of the second kind. The kinetic energy of electrons converted per unit volume and per second into potential energy, by exciting the atoms in energy level i to energy level j, is given by the product of the energy jump $\Delta E(i,j)$ involved, the collisional excitation rate, and the factor $B(i,j)$ defined in Section 8B as the fraction of exciting collisions that is not balanced by de-exciting collisions. As has been shown previously, in the case of hydrogen no serious error is introduced by disregarding all other collisional excitation processes, including direct ionization, and considering only step-wise excitation. This can be written:

$$R_{col}(i,i+1) \; B(i,i+1) = const. \;(all\; i) = R_{col}^{ef} \quad , \qquad (9\text{-}13)$$

which will be recognized as Eq. 8-14 written in another form. Since:

$$\sum_{i}^{\infty} i\Delta E(i,i+1) = E_{\infty} \quad ,$$

the average energy loss per electron due to inelastic collisions in time t_f, can thus be estimated with:

$$\Delta E_{-}(exc) = R_{col}^{ef} \; t_f \; E_{\infty} \; / \; n_e \qquad (9\text{-}14)$$

In the arc core at reduced pressure, $B(1,2) \approx 1$, and we can set $R_{col}^{ef} = R_{col}(1,2)$, whose value is shown in Table XII. This yields: $\Delta E_{-}(exc,H) \approx 4 \times 10^{-3}$ eV. Assuming that $\Delta E_{-}(exc,O)$ is of the same order, we have:

$$\Sigma \; \Delta E_{-} = \Delta E_{-}(el) + \Delta E_{-}(exc,H) + \Delta E_{-}(exc,O) = 7.9 \times 10^{-3} \text{ eV} = \Delta E_{+} \quad ,$$

which comes quite close to the ΔE_{+} calculated before.

Lack of equipartition between the kinetic energy of electrons and heavy particles is generally associated with plasmas at low pressure. It has been shown here, however, that even at atmospheric pressure a substantial divergence between the electron and the gas temperature of the plasma can arise, if the degree of ionization is very low. Because of the small neutral cross-sections, the mean free path is then so long that the electrons can gain a relatively large amount of energy from the applied electric field. Ion cross sections are typically 50 times larger, and if the plasma is only a few percent ionized, the free path will be substantially decreased. Elastic collisions with neutrals can then be disregarded in a first approximation, and by combining Eqs. 9-11 and 9-12, one obtains a scaling law for the lack of equipartition:

$$\frac{T_e - T_g}{T_e} \propto \left(\frac{T_e}{n_e} \right)^2 = \rho_D^4 \qquad (9\text{-}15)$$

The dependence on T_e/n_e is therefore still stronger than in the case of departures from an equilibrium distribution over energy levels due to diffusion (Eq. 9-6).

One also has to examine if equipartition of kinetic energy exists between the ions and neutrals in the plasma. In plasmas that are in LTE and are substantially ionized, the kinetic temperature of ions and of neutrals will tend to equilibrate via the ionization-recombination process, which is then more effective than elastic collisions between ions and neutrals (4). This mechanism is not operative in diffusion-dominated plasmas, however, because of the low probability for volume recombination (Section 9A). In the core of the low-pressure arc investigated in this work, at 2% ionization, the frequency of elastic electron-neutral and electron-ion collisions are about equal. At slightly higher

ionization, most of the kinetic energy transfer to heavy particles will already
occur by electron-ion interaction. Since distant encounters between charged
particles again have to be taken into account, the cross-sections for elastic
ion-ion collisions are much larger than for ion-neutral collision. Equiparti-
tion of kinetic energy between ions and atoms depends then to a large extent
on the effectiveness of the charge-transfer mechanisms, which is difficult to
estimate. In prior work with high-current argon arcs at reduced pressure, we
have found a notable divergence between the kinetic temperatures of ions and of atoms
(45); although the ion temperatures reported in Ref. 45 are too high because the
calculated Stark broadening parameter was used to correct the half width of the
Doppler-broadened Ar II 4348 $\overset{o}{A}$ line (see Section 3D).

10. MOLECULAR SPECIES IN DIFFUSION-DOMINATED PLASMAS

A. Excitation Processes

We will now apply the concepts developed in the preceding Sections to a discussion of the interaction processes in non-equilibrium plasmas leading to the observed population distributions over molecular energy levels.

Also for molecules such as OH, electronic excitation and ionization and the inverse processes are dominated by collisional interaction with free electrons. A close correspondence will therefore exist between atomic and molecular species with respect to the population distribution over excited electronic states and the ionization-recombination equilibrium.

For a diffusion-dominated water vapor arc one would predict a population distribution between the ground and first excited electronic state, described by a distribution temperature much higher than the gas temperature and comparable to the distribution temperature pertaining to the occupation of the first and second energy level of hydrogen. The distribution temperature will fall substantially when progressing to higher energies, leading to a decreased occupation of the higher electronic states. The population of the Rydberg states and the concentration of OH^+ will then be very small.

The first of these predictions was indeed verified by our experimental results, and also no trace of the $OH(B^2\Sigma - A^2\Sigma)$ band at 4336 $\overset{o}{A}$ was found. The search for the $OH^+(A^3\Pi - X^3\Sigma)$ bands was inconclusive, because these bands fall in a very crowded spectral region due to the strong excitation of the Schumann-Runge bands.

We have shown that in the plasma the distribution over the rotational-vibrational levels of $OH(A^2\Sigma)$, that are not affected by predissociation, is close to a Boltzmann distribution at the gas temperature. It must be concluded, therefore, that the rate coefficients for excitation of nuclear motion by electron impact are not significantly larger than the rate coefficients for the equivalent process induced by heavy particle encounters, so that at low electron densities the latter predominates.

Because of the small optical transition probabilities for the transition $A^2\Sigma \rightarrow X^2\Pi$, radiative decay to the ground state is negligible compared to collisionally induced transitions between the vibrational and rotational levels of the $A^2\Sigma$ state. To a good approximation, these excitation rates are proportional to the transition moment and therefore subject to the same selection rules as optical dipole transitions. A rotational level J can then combine only with the rotational levels $J \pm 1$, and rotational excitation and de-excitation will occur by a step-wise process. The threshold is small compared to the mean kinetic energy of heavy particles, and the exponential factor is close to unity. The magnitude of the excitation rate for the transition $J \rightarrow J + 1$ is therefore determined by the transition moment, proportional to $(J +1)/(2J + 1)$. With the exception of the lowest rotational levels, the excitation rate is thus practically independent of the rotational quantum number. This can be contrasted with collisional excitation of hydrogen atoms, where transitions into other than neighboring levels are less probable, but not strictly forbidden. The rates for the transition $i \rightarrow i \pm 1$ increase as i^4 for the higher energy levels of hydrogen.

The occupation of the $A^2\Sigma$ state of OH is mainly determined by the balance between transitions from the ground state and into the next higher electronic state, induced by electron collision. The excitation process $X^2\Pi \rightarrow A^2\Sigma$ occurs, of course, according to the Franck-Condon principle; moreover the electronic

103

excitation rate is also independent of the nuclear motion of the excited molecule. The distribution over the vibrational-rotational levels of the ground state is, therefore, "frozen" into the population distribution for the electronically excited molecule.

Since dissociation occurs by heavy particle collision, the equilibrium occupation of energy levels with respect to the dissociated state is determined by the gas temperature. Because of the high distribution temperature characterizing the relative occupation of the $A^2\Sigma$ and the $X^2\Pi$ state, the overpopulation of the electronically excited state will always be larger than for the ground state; in the low pressure arc, in fact, by several orders of magnitude. Experimentally, it has been established, however, that the population distribution over the lower rotational and vibrational levels of the $A^2\Sigma$ state is close to a Boltzmann distribution at the gas temperature. The probability for a collisionally induced transition into the dissociated state must therefore be very small for these states. This is discussed more fully in the next Section.

The concentrations of O_2 and of H_2 will be in a quasi-equilibrium with OH at the gas temperature, because collisions with heavy particles are effective in inducing reactions of the type:

$$OH + O \rightleftharpoons H + O_2$$
$$OH + H \rightleftharpoons O + H_2$$
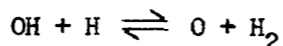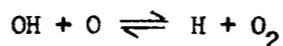
whose energy threshold is comparable to the mean kinetic energy of heavy particles. Because of the higher gas temperatures in arcs, the pertinent rate coefficients will be higher than in flames, but in principle the same considerations apply (46). The experimental evidence for a substantial concentration of O_2 in the arc plasma is given by the prominence of the Schumann-Runge bands belonging to transitions between highly excited vibrational levels.

B. The Dissociation Equilibrium of OH and Predissociation

The Saha equation is only a specialized form of the general mass action equation, and the conclusions reached in discussing ionization-recombination equilibria apply also to the dissociation-recombination equilibrium. Dissociation of ground state OH can be compared with the previously discussed ionization of ground state hydrogen, with heavy particles taking the part of free electrons. The transition moment for direct transitions into the dissociated state is small, and the threshold energy is large compared to thermal energies. It follows that the free time of a $OH(X^2\Pi)$ molecule with respect to a dissociating collision is much longer than the free time between elastic collisions. It can thus diffuse over a distance comparable to the arc diameter before being effectively dissociated.

Because of the small probability for volume recombination, ground state OH will mostly be formed by the effective mechanism of wall-recombination. The concentration of OH in the arc center is then not determined by an equilibrium relation, but by the balance between the rate of diffusion of OH from the arc periphery and the excitation rate into the $A^2\Sigma$ state, induced by electron impact. Thus we found the concentration of ground state OH to be almost constant over the entire cross-section of the arc at reduced pressure, and higher than the equilibrium concentration at the gas temperature by almost two orders of magnitude. In the arc at atmospheric pressure an overpopulation of $OH(X^2\Pi)$ has also been established (Sections 5D and 5E).

Gaydon and Wolfhard (47) have discussed the perturbation of the $A^2\Sigma^+$ state by a lower electronic state, leading to a predissociation belonging to Herzberg's case Ic (48). The perturbing state is most likely a $^2\Sigma^-$ state, and its dissociation products are normal (i.e. ground state) atoms, whereas the $A^2\Sigma$ state dissociates

into ground state hydrogen and excited (^{1}D) oxygen atoms. The effective potential energy curves (i.e. including rotation) cross at about $E' = 42,000$ cm^{-1} for $v' = 0$ of the $A^2\Sigma$ state and at progressively lower energies for the higher vibratinal levels. An unusual characteristic of the predissociating rotational levels is the splitting of the Boltzmann plots for the two spin components (see Fig. 25). The f_1 level with $J = K + 1/2$ is weakened because the probability for a transition into the perturbing electronic state is higher than for the f_2 level of same K (47).

The A electronic state of OH is a $^2\Sigma$ state, and the selection rules for Hund's case b apply, i.e. in addition to the strict selection rule for dipole transition: $J \rightarrow J \pm 1$, we also have the selection rule $K \rightarrow K \pm 1$. Combinations between the f_1 and f_2 levels are not strictly forbidden and correspond to the weak satellite branches, whose intensity with respect to the main branches decreases with increasing J. Similarly for collisional processes, if the f_1 levels are more strongly depopulated by predissociation than the f_2 levels, the splitting of the Boltzmann plots should increase with J because of the decreased probability for $f_2 \rightarrow f_1$ transitions. This is, in fact, what is observed and can be taken as further evidence that the selection rules for optical dipole transition also apply to transitions induced by collisions.

As is seen most clearly in the case of the (2,1) and (2,2) bands (see Fig. 25), after the onset of predissociation a short transition region is followed by a range of rotational energy levels for which the Boltzmann plot is again linear, although its slope does not correspond to any meaningful temperature. This can be explained as follows. In this range $a(J)/a(J-1) \ll 1,^{*)}$ and de-excitations can

---

*) $a(J)$ is equivalent to $a(i)$ defined in Eq. 7-7

be disregarded in a first approximation. The occupation of a predissociating rotational level J is then mainly determined by the balance between transitions from J - 1 to J, and from J to J + 1 and dissociating transitions via the perturbing state:

$$n(J-1) \; X(J-1,J) \;\; \approx \;\; n(J) \left[\; X(J,J+1) + D(J) \; \right] \qquad (10\text{-}1)$$

Since $\Delta E(J,J+1) \ll kT_g$, the exponential factor is close to unity, and the specific dependence of the excitation cross-section on the energy of the colliding particle is unimportant. The excitation rates can then be approximated by an expression of the form:

$$X(J,J+1) \;\; \approx \;\; \frac{J+1}{2J+1} \; C(T_g) \qquad (10\text{-}2)$$

and Eq. 10-1 can be written:

$$\frac{n^*(J-1)}{n^*(J)} \;\; \approx \;\; \frac{J+1}{J} + \frac{2J+1}{J} \; \frac{D(J)}{C(T_g)} \qquad (10\text{-}3)$$

$$J \gg 1 \; ; \; D(J) \ll C(T_g): \quad \frac{n^*(J-1)}{n^*(J)} \;\; \approx \;\; \exp \left[\; 2D(J)/C(T_g) \; \right] \qquad (10\text{-}4)$$

The Boltzmann plot will thus be approximately linear over the range, where:

$$D(J) \;\; = \;\; D(T_g) \;\; \ll \;\; C(T_g) \qquad (10\text{-}5)$$

Is shown by Kronig, the transition moment for predissociations for which $\Delta\Lambda = 0$ – which applies to this case – is independent of J in a first approximation (49). The predissociation also has to be considered as weak $[D(J) \ll C(T_g)]$, because it violates the $K \rightarrow K$ rule (47, 48).

The observed sharp drop in the occupation of the highest rotational levels occurs because of the now significant probability for direct dissociation of the $^2\Sigma$ state into $H(1) + O(^1D)$ ("predissociation by rotation"). As the energy term

of the vibrational-rotational levels approaches the dissociation energy for the $A^2\Sigma$ state, the occupation of these levels will tend to an equilibrium occupation with respect to the dissociated state.

11. EFFECT OF THE AUGER PROCESS ON POPULATION DISTRIBUTIONS

The population distributions over the energy levels of oxygen and over the predissociating rotational levels of the $A^2\Sigma$ state of OH are both affected by an Auger process of small probability as compared to the excitation rates, and a similarity between the respective Boltzmann plots can be expected. A splitting of the Boltzmann plot, which is readily observable in the case of OH, has also been predicted for oxygen and is caused by an essentially similar mechanism as discussed in Section 7C.

The Boltzmann plot for oxygen is also approximately linear over a considerable range of energy levels (see Fig. 15), and the same explanation appears plausible: Predominance of step-wise excitation and near-constancy of the excitation and ionization rates. It is certainly only accidental that the measured distribution temperatures for the quintet states of oxygen are close to the gas temperature, because excitation by heavy particle collision has been shown to be insignificant in this plasma as compared to the same process induced by electron impact.

The dissociated states of OH - oxygen atoms in the ^3P and ^1D levels - are analagous to the ionized states of oxygen - ions in the ^4S, ^2D, and ^2P levels - in the sense that in both cases optical dipole transitions between these states are strictly forbidden by the Laporte rule. Because of a correspondingly small collisional interaction among these states, their occupation will be effectively uncoupled in non-equilibrium plasmas.

12. CONCLUSIONS

It has been shown in this work that the integrated radiance of the rotational lines belonging to the OH ($A^2\Sigma - X^2\Pi$) system can be represented by an expression of the form:

$$N_L = C\, n^*(n', v', K')\, P_o^o\, P_o'(q', q'')\, \exp\left[-p(q', q'')\, F(K)\right]\, S/\lambda^4 \qquad (12\text{-}1)$$

The integrated line absorption coefficient - i.e. the quantity obtained by an absorption measurement at high resolution - is then related to the occupation of the lower state for the transition by a similar expression, with the "line strength factor" S/λ^4 substituted by $S\lambda$.

Eq. 12-1 follows from the linearity of the "apparent Boltzmann plot", and has been verified here for the main branches of the (0,0), (1,0), (1,1), (2,1), and (2,2) bands below the onset of predissociation. The molecular constant denoted by P_o^o - formally equivalent to an "average electronic transition moment" for the system - is proportional to the radial part of the transition moment for the P-1 lines of the (0,0) band (see Eqs. 2-27 and 2-31) that corresponds, in a sense, to the fundamental transition for this system (the "vibration and rotation-less molecule"). The numerical value for P_o^o could not be ascertained because of the difficulties in determining the concentration of OH in the plasma, noted below. The quantities $P_o'(q', q'') = P_o'(v', v'')$ have been shown to be constant for a particular band, i.e. they do not depend on the specific branch, and are, therefore, enitrely equivalent to the concept of Franck-Condon factors. The dependence of the radial part of the transition moment on the rotational transition is contained in the exponential factors $p(q', q'')$, that also have been found to be, in general, independent of the specific branch within a band. An exception has been noted for the (1,0) band, but this may only be spurious (see Section 6B). Because of the ambiguity in assigning an average frequency to a band, the representation of

rotational line intensities (or absorption coefficients) in terms of band transition probabilities or band oscillator strengths is not appropriate.

Implicit in our derivation of the transition moments is the assumption that the occupation of the non-predissociating rotational-vibrational energy levels is, in effect, given by a Boltzmann distribution at the gas temperature. However, even when the population distribution over energy levels shows an exponential dependence on the energy term, this is not sufficient proof for an equilibrium distribution, as has been discussed in Section 10B. Since departures from LTE in diffusion-dominated plasmas lead to lower distribution temperatures when progressing to higher energies, the P'_o-factors (Franck-Condon factors) derived in this work constitute only a lower bound, and the exponential p-factors only an upper bound for the true values. This is especially evident for the bands originating in the $v' = 2$ level, where the P'_o factors measured here are probably too low, and the p-factors obviously too high.

$-$ o $-$

Even at the lowest electron densities at which a steady arc discharge can be sustained, electronic excitation of OH by electron impact is more effective than by heavy particle collision. The distribution temperature characterizing the relative occupation of the ground state of OH and the $A^2\Sigma$ excited electronic state exceeds then the gas temperature, that is the relevant temperature for the dissociation-recombination equilibrium. The $A^2\Sigma$ state will thus be overpopulated with respect to the dissociated state, and the population distribution over its higher rotational-vibrational levels will be determined by predissociation. If the electric current of an arc at atmospheric pressure is increased, the degree of ionization of the plasma rises sharply, and equipartition between the kinetic energy of electrons and of heavy particles will eventually be approached by the mechanism discussed in Section 9C. Based on the present investigation it can be predicted, however, that this will not occur at temperatures below 10,000 K.

110

;ince OH is almost completely dissociated at this temperature, it does not
ppear possible to obtain arc plasmas with an equilibrium concentration of OH,
hat are suitable for spectroscopic measurements.

By varying the pressure and the current of a water vapor arc, the occu-
ation of a particular rotational-vibrational level of the $A^2\Sigma$ state of OH can
e maximized, as has been done in this investigation. However, this occupation
annot be calculated with precision because it depends to a large extent on the
ffectiveness of the various diffusion processes occurring simultaneously in the
lasma. Although the Fowler-Milne method is then clearly inapplicable, this arc
egime still offers the significant practical advantage of an increased stability
gainst small arc fluctuations.

Because of the small probability for direct transitions into the dissociated
tate or into the adjacent rotational-vibrational levels, the step-wise excitation
nd de-excitation mechanism in conjunction with the near-equality of the transi-
ion rates, effectively uncouples the lower rotational-vibrational levels from
he dissociated state. The relative population distribution over these levels
ill therefore approach an equilibrium distribution at the gas temperature, even
hen the total occupation of the $A^2\Sigma$ state is orders of magnitude higher than its
quilibrium occupation.

The relaxation times with respect to the dissociation-recombination process
re still much longer for OH molecules in the ground state, which can diffuse
ver a considerable distance before equilibrium is established. The relative
spulation distribution over the excited states is essentially determined by local
arameters, and can then be derived in principle, even in absence of equilibrium,
f the appropiate rate coefficients are known. The concentration of OH can be
xperimentally measured in high-resolution work if the molecular constant

111

P_o^o $(A^2\Sigma - X^2\Pi)$ is known, as has been shown here. It does not appear possible, however, to obtain the concentration of OH in arcs by calculation, which requires not only detailed information on the entire arc profile, but also on the boundary conditions because of the significance of wall-recombination.

It should be noted, that in this respect the situation is not much more favorable in diffusion flames, and the use of equilibrium relations in order to calculate the concentration of OH in these sources and derive absolute transition probabilities, has to be viewed with caution.

Much work remains to be done in characterizing and interpreting departures from equilibrium in flames. Overpopulation of excited electronic states can occur not only via chemiluminescence, but conceivably also by electron collisions, since the concentration of free electrons in many flames is much greater than expected at equilibrium, and it has also been suggested that the electron temperature is higher than the gas temperature. It appears likely that observed inconsistencies in measurements of flame temperatures, that in the past have been attributed to incorrect transition probabilities, were also caused by nonequilibrium effects.

A	area under recorded line trace or atomic weight
$A(j,i)$	spontaneous transition probability (s^{-1})
a	coupling constant
$a(i)$	overpopulation of energy level i
$B(i,j)$	ratio of effective to total number of exciting collisions
c	velocity of light in vacuum
D	dispersion $(mm/\overset{\circ}{A})$
d	diffusion length (cm)
E	electric field strength (V/cm)
E_H	ionization potential of hydrogen
E_i	energy term pertaining to energy level i (cm^{-1})
E_∞	ionization potential
$F(i,T)$	Saha equation for atoms in energy level i
$F(K)$	rotational energy term (cm^{-1})
F_o	normalized field strength
$f(i,j)$	absorption oscillator strength
$G(v)$	vibrational energy term (cm^{-1})
$g(i)$	statistical weight of energy level i
h	Planck constant
hw	(full) half width of a line
I	current (amps)
$I(i,j)$	part of excitation rate coefficient that depends only on the quantum numbers of the two levels
I_L	integrated line radiance (W cm^{-2} sr^{-1})
I_λ	intensity = spectral radiance (W cm^{-2} sr^{-1} μ^{-1})
i	(principal) quantum number

113

J	total angular momentum quantum number
j	(principal) quantum number
K	quantum number of total angular momentum except for spin or equilibrium constant
k	Boltzmann constant
k'	net absorption coefficient (cm^{-1})
L	length of optical path (cm)
m	magnetic quantum number or slope of Boltzmann plot (cm)
N_i	concentration of ions (cm^{-3})
N_L	integrated radiance of optically thin line ($W\ cm^{-2}\ sr^{-1}$)
N_t	total concentration of particles (cm^{-3})
N_λ	spectral radiance of optically thin line ($W\ cm^{-2}\ sr^{-1}\ \mu^{-1}$)
n_e	electron density (cm^{-3})
n(i)	occupation of energy level i (cm^{-3})
n*(i)	occupation of degenerate energy states belonging to level i
n*(∞)	occupation of last bound energy state (cm^{-3})
P	pressure (atm) or radial part of the transition moment times a constant ($s^{-1}\ \mu^3$)
$P'_o(v',v'')$	Franck-Condon factor
p	partial pressure (atm) or exponential correction factor (cm)
Q	internal partition function
q	specified group of rotational-vibrational levels
R	response of detection system or reaction rate ($cm^{-3}\ s^{-1}$)
$\|R(j,i)\|^2$	transition moment

S	source function ($W\ cm^{-2}\ sr^{-1}\ \mu^{-1}$) or resultant spin quantum number or rate coefficient for collisional ionization/recombination
S(K'J',K"J")	Hoenl-London factor (rotational line strength)
S(α)	Stark broadening parameter
T	temperature (K)
T_D	distribution "temperature" (K)
T_e	kinetic temperature of electrons (K)
T_g	kinetic temperature of heavy particles (gas temperature) (K)
T'_{rot}	apparent rotational "temperature" (K)
$U[u(i,j)]$	function entering the rate coefficients
$\dot{u}(i,j)$	exponent of the Boltzmann factor
V	potential (volt)
V_λ	recorded signal (relative intensity)
v	vibrational quantum number or root mean square velocity (cm/s)
X	rate coefficient for collisional excitation/de-excitation
[X]	concentration of species X
y	reduced intensity of rotational line
Z	total partition function
$\alpha(i)$	radiative recombination coefficient ($cm^6\ s^{-1}$)
α_λ	absorptance
ϵ	emissivity
ϵ_λ	emission coefficient ($W\ cm^{-3}\ sr^{-1}\ \mu^{-1}$)

ζ	correction factor for the intensity of the continuum
Λ	quantum number of the resulting orbital angular momentum about the internuclear axis
λ	wavelength or mean free path (cm)
ν	frequency (s^{-1})
ρ_D	Debye radius (cm)
σ	cross section (cm^2)

SUBSCRIPTS, SUPERSCRIPTS AND INDICES

c	(ionization) continum
col	collisional
Eq	equilibrium
e	electron
ef	effective
exc	excitation
o	line center
rad	radiative
rec	recombination

REFERENCES

1. J. Richter, Über Temperaturmessungen an thermischen Plasmen bekannter Zusammensetzung. Z. Astrophys. $\underline{61}$, 57 (1965).

2. H. R. Griem, A. C. Kolb, and K. Y. Shen, Stark Broadening of Hydrogen Lines in a Plasma, Phys. Rev. $\underline{116}$, 4 (1959).

3. H. R. Griem, A. C. Kolb, and K. Y. Shen, Stark Profile Calculations for the H_β Line of Hydrogen, Astrophys. J. $\underline{135}$, 272 (1962).

4. H. R. Griem, Plasma Spectroscopy, McGraw-Hill, New York (1964).

5. J. Cooper, Plasma Spectroscopy, Rep. Prog. Phys. $\underline{29}$, 35 (1966).

6. J. Richter, Radiation of Hot Gases, ch. 1 in Plasma Diagnostics, Ed. W. Lochte-Holtgreven, North-Holland, Amsterdam (1968).

7. H. R. Griem, Validity of Local Thermal Equilibrium in Plasma Spectroscopy, Phys. Rev. $\underline{131}$, 1170 (1963).

8. D. R. Bates, A. E. Kingston, and R. W. P. McWhirter, Recombination between Electrons and Atomic Ions. I. Optically thin Plasmas, Proc. Roy. Soc. A, $\underline{267}$, 297 (1962).

9. R. C. Tolman, The Principles of Statistical Mechanics, Oxford University Press, London (1938).

10. H. J. Babrov, Instrumental Effects in Infrared Gas Spectra and Spectroscopic Temperature Measurements. J. Opt. Soc. Amer. $\underline{51}$, 171 (1961).

11. J. B. Tatum, The Interpretation of Intensities in Diatomic Molecular Spectra, Astrophys. J. (Suppl.), $\underline{14}$, 21 (1967).

12. G. H. Dieke and H. M. Crosswhite, The Ultraviolet Bands of OH - Fundamental Data, J. Quant. Spectrosc. Radiat, Transf. $\underline{2}$, 97 (1962).

13. T. C. James, Rotation-Vibration Interaction in Electronic Transitions. Application to Rotational "Temperature" Measurements. J. Chem. Phys. $\underline{32}$, 1770 (1960).

14. J. Anketell and R. C. M. Learner, Vibration-Rotation Interaction in OH and the Transition Moment, Proc. Roy. Soc. A $\underline{301}$, 355 (1967).

15. R. G. Bennet and F. W. Dalby, Experimental Determination of the Oscillator Strength of the Violet System of OH, J. Chem. Phys. $\underline{40}$, 1414 (1964).

16. F. Burhorn and R. Wienecke, Plasmazusammensetzung, Plasmadichte, Enthalpie und spezifische Wärme von Wasserstoff und Wasser bei 1, 3, 10 und 30 atm im Temperaturbereich zwischen 1000 and 3000 K, Z. Phys. Chem. $\underline{215}$, 285 (1960).

17. JANAF, Thermochemical Tables, Dow Chemical Co., Midland, Mich. (1960).

18. J. E. Mayer and M. G. Mayer, Statistical Mechanics, J. Wiley, New York (1940).

19. R. W. Larenz, Über ein Verfahren zur Messung sehr hoher Temperaturen in nahezu durchlässigen Bogensäulen, Z. Physik $\underline{129}$, 327 (1951).

20. T. K. McCubbin, J. A. Lowenthal, and H. R. Gordon, An Infrared Vacuum Grating-Prism Spectrometer, Appl. Optics $\underline{4}$, 711 (1965).

21. W. Knight, Y. Kohanzaden, and G. Lengyel, Evaluation of Magnetic Defocusing for a Photomultiplier Tube with Large Area Semitransparent Photocathode, Appl. Optics $\underline{7}$, 1115 (1968).

22. J. C. DeVos, A New Determination of the Emissivity of Tungsten Ribbon, Physica $\underline{20}$, 690 (1954).

23. L. Klein, Arc Source for Spectroscopic Measurements of Isothermal Plasma Samples at Various Pressures, Rev. Sci. Instrum. $\underline{41}$, 668 (1970).

24. I. Bues, H. J. Patt, and J. Richter, Über die elektrische Leitfähigkeit und die Wärmeleitfähigkeit des Argon bei hohen Temperaturen, Z. Angew. Phys. $\underline{22}$, 345 (1967).

25. K. Bockasten, Transformation of Observed Radiances into Radial Distribution of the Emission of a Plasma, J. Opt. Soc. Amer. $\underline{51}$, 943 (1961).

26. W. L. Barr, Method for Computing the Radial Distribution of Emitters in a Cylindrical Source, J. Opt. Soc. Amer. $\underline{52}$, 885 (1962).

27. E. A. McLean and S. A. Ramsden, Optical Interferometric and Spectroscopic Measurements of Electron Density in a Plasma, Phys. Rev. $\underline{140}$, A1122 (1965).

28. R. A. Hill and J. B. Gerardo, Stark Broadening of H_β, H_γ, and H_σ: An Experimental Study, Phys. Rev. $\underline{162}$, 45 (1967).

29. R. A. Hill, Fractional Intensity Widths and Stark-Broadening Formula for the Hydrogen Balmer Lines, J. Quant. Spectrosc. Radiat. Transf. $\underline{7}$, 401 (1967).

30. B. Wende, Kontinuierlicher Absorptionsquerschnitt von Argon im Bogenplasma, Z. Physik $\underline{198}$, 1 (1967).

31. W. L. Wiese, M. W. Smith, and B. M. Glennon, <u>Atomic Transition Probabilities</u>, Vol. I, National Bureau of Standards, Washington, D.C. (1966).

32. C. E. Moore, A Multiplet Table of Astrophysical Interest, Natl. Bur. Std. (U.S) Tech, Note 36 (1959).

33. B. Wende, Optische Übergangswahrscheinlichkeiten der Konfiguration $3p^5 4s - 3p^5 5p$ des Argon I. Z. Physik $\underline{213}$, 341 (1968).

34. H. J. Babrov, G. Ameer, and W. Benesch, Molecular Collision Cross Sections from Infrared Absorption Measurements, J. Chem. Phys. $\underline{33}$, 145 (1960).

35. R. W. P. McWhirter and A. G. Hearn, A Calculation of the Instantaneous Population Densities of the Excited Levels of Hydrogen-like Ions in a Plasma, Proc, Phys. Soc. $\underline{82}$, 641 (1963).

36. H. W. Drawin, Zur spektroskopischen Temperatur- und Dichtemessung von Plasmen bei Abwesenheit thermodynamischen Gleichgewichtes, Z. Physik $\underline{172}$, 429 (1963); Anregung und Ionisation eines Wasserstoffplasmas unter dem Einfluss zweier Elektronengruppen unterschiedlicher Temperatur und Dichte, Ann. Phys. $\underline{17}$, 374 (1966).

37. A. Unsöld, *Physik der Sternatmosphären*, Springer, Berlin (1955).

38. D. R. Bates, and A. Delgarno, Electronic Recombination, ch. 7 in *Atomic and Molecular Processes*, Ed. D. R. Bates, Academic Press, New York (1962).

39. V. N. Kolesnikow, *Dugovoi razriad v inertnih gazah* (Arc Discharge in Noble Gases) Tr. Fiz. Inst. Akad. Naukk 30, 66 (1964).

40. W. Lochte-Holtgreven, Evaluation of Plasma Parameters, ch. 3 in *Plasma Diagnostics*, Ed. W. Lochte-Holtgreven, North-Holland, Amsterdam (1968).

41. H. W. Drawin, Influence of Atom-Atom Collisions on the Population Densities of Excited Atomic Levels, Z. Naturforsch. 25a, 145 (1970).

42. L. Spitzer, *Physics of Fully Ionized Gases*, Interscience, New York (1962).

43. H. Schlüter, Rekombination und Ionisation in einer stationären Hochfrequenzentladung, Z. Naturforsch. 18a, 439 (1963).

44. W. Finkelnburg and H. Maecker, Elektrische Bögen und thermisches Plasma, *Handbuch der Physik*, Vol. 22/II, Springer, Berlin (1956).

45. L. Klein, Spectroscopic Diagnostics of Argon Arcs at Reduced Pressure, Proc. 9th Int. Conf. Phenomena Ionized Gases, Bucharest (1969) p. 636.

46. R. M. Fistrom and A. A. Westenberg, *Flame Structure*, McGraw-Hill, New York (1965).

47. A. G. Gaydon and H. G. Wolfhard, Predissociation in the Spectrum of OH; the Vibrational and Rotational Intensity Distribution in Flames, Proc. Roy. Soc. A 208, 63 (1951).

48. G. Herzberg, Molecular Spectra and Molecular Structure, I. *Spectra of Diatomic Molecules*, 2nd, ed., Van Nostrand, Princeton, N.J. (1950).

49. R. de L. Kronig, Zur Deutung der Bandenspektren II. Z. Physik <u>50</u>, 347 (1928).

50. Condon, E. U. and Shortley, G. H., <u>The Theory of Atomic Spectra</u>, University Press, Cambridge (1935).

51. Schadee, A., The Relation Between the Electronic Oscillator Strength and the Wavelength for Diatomic Molecules, J. Quant. Spectrosc. Radiat. Transf. <u>7</u>, 169 (1967).
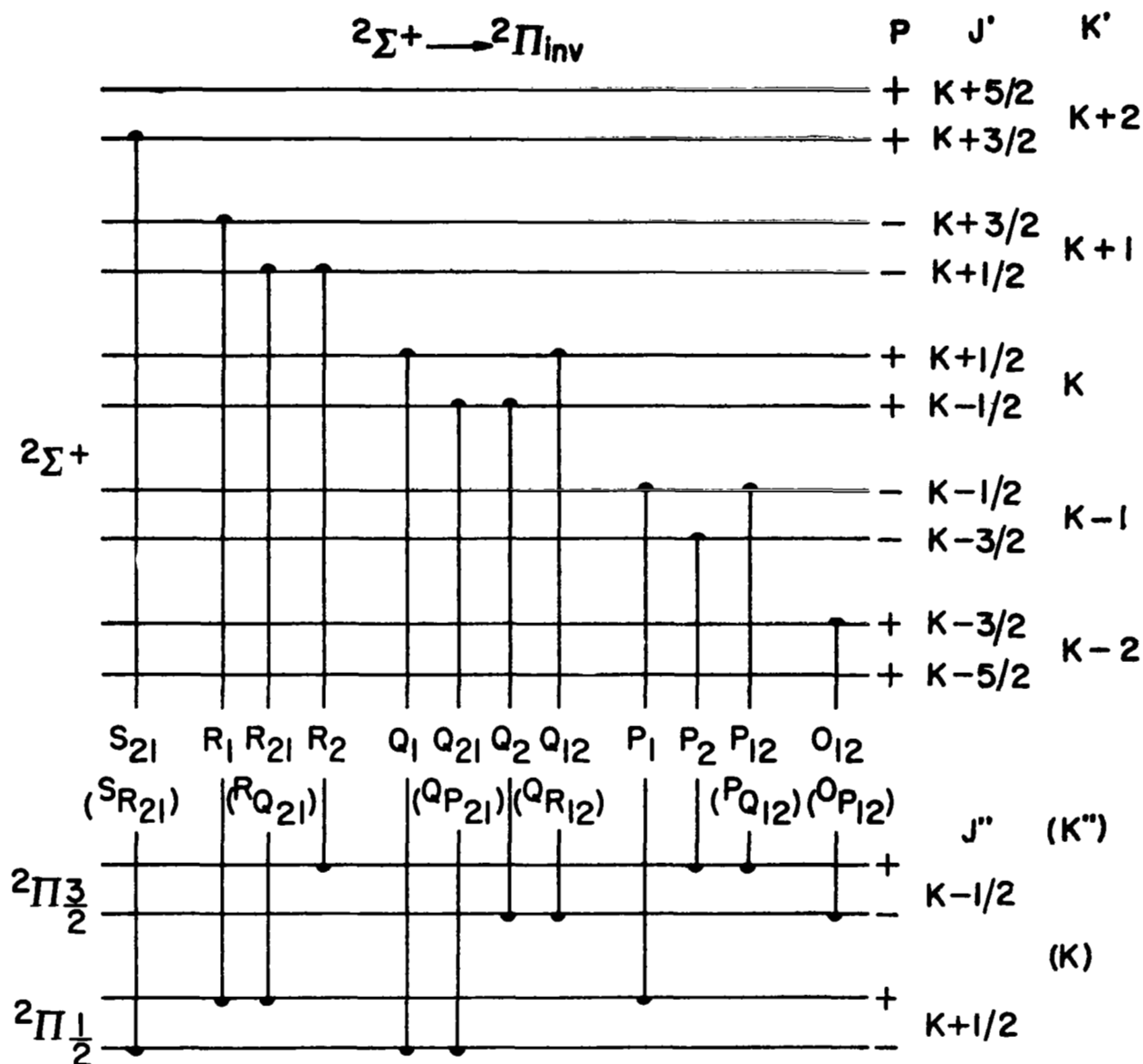
Fig. 1. Diagram of the rotational energy levels of the $X^2\Pi$ and $A^2\Sigma$ states of OH. The twelve branches corresponding to the allowed transitions to a lower rotational level $K \geq 2$ are shown. The branches are labelled assuming Hund's case (b) for the ground state. Herzberg's notation for the satellite lines is indicated in parentheses.
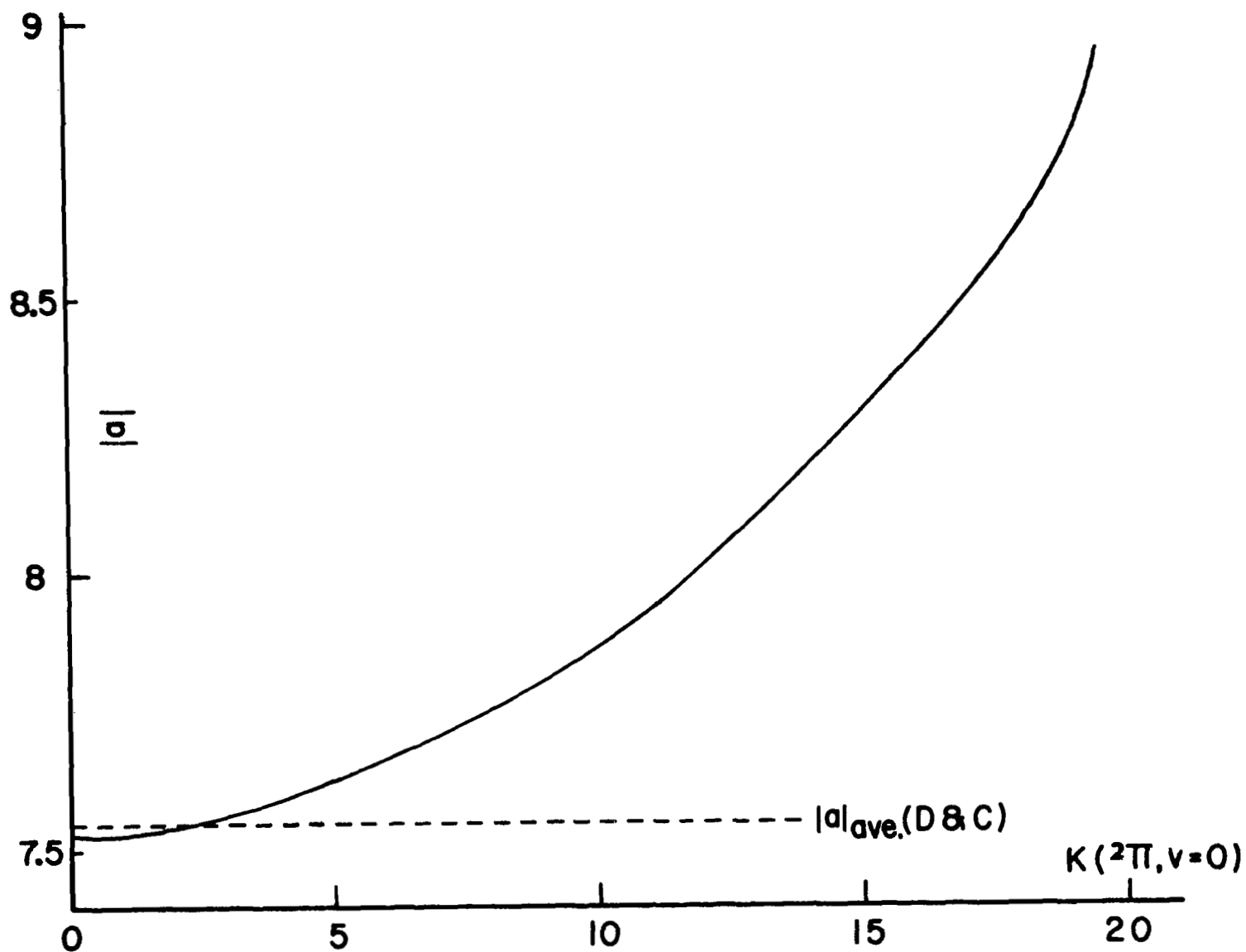
Fig. 2. Dependence of the coupling constant on the rotational quantum number for the lowest vibrational level of the $X^2\Pi$ state of OH. The average value of the coupling constant (a = -7.55) used by Dieke and Crosswhite (12) for their computations of line strengths is indicated.
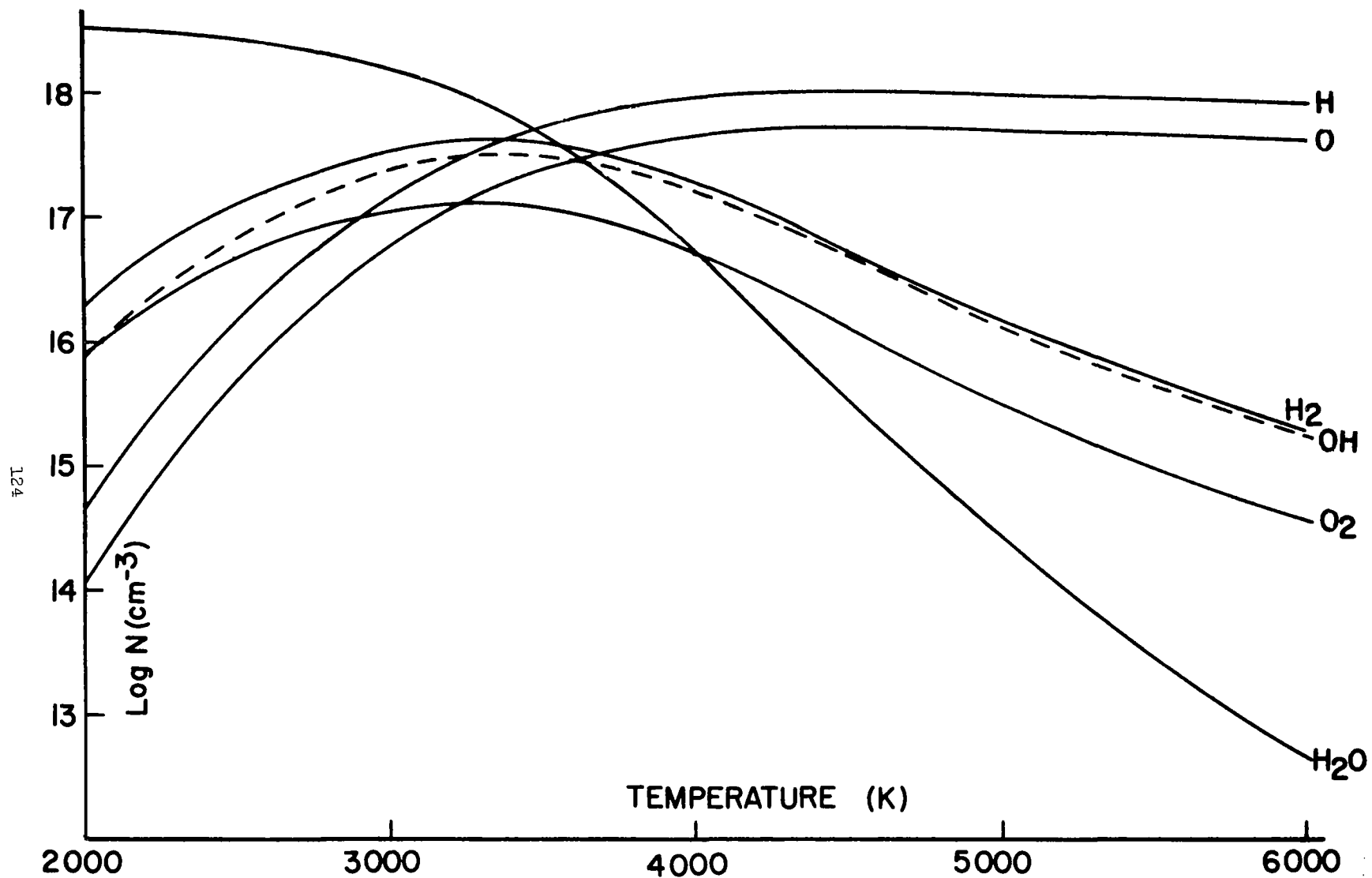
Figure 3. Calculated equilibrium composition of a water vapor plasma at 1 atm pressure.
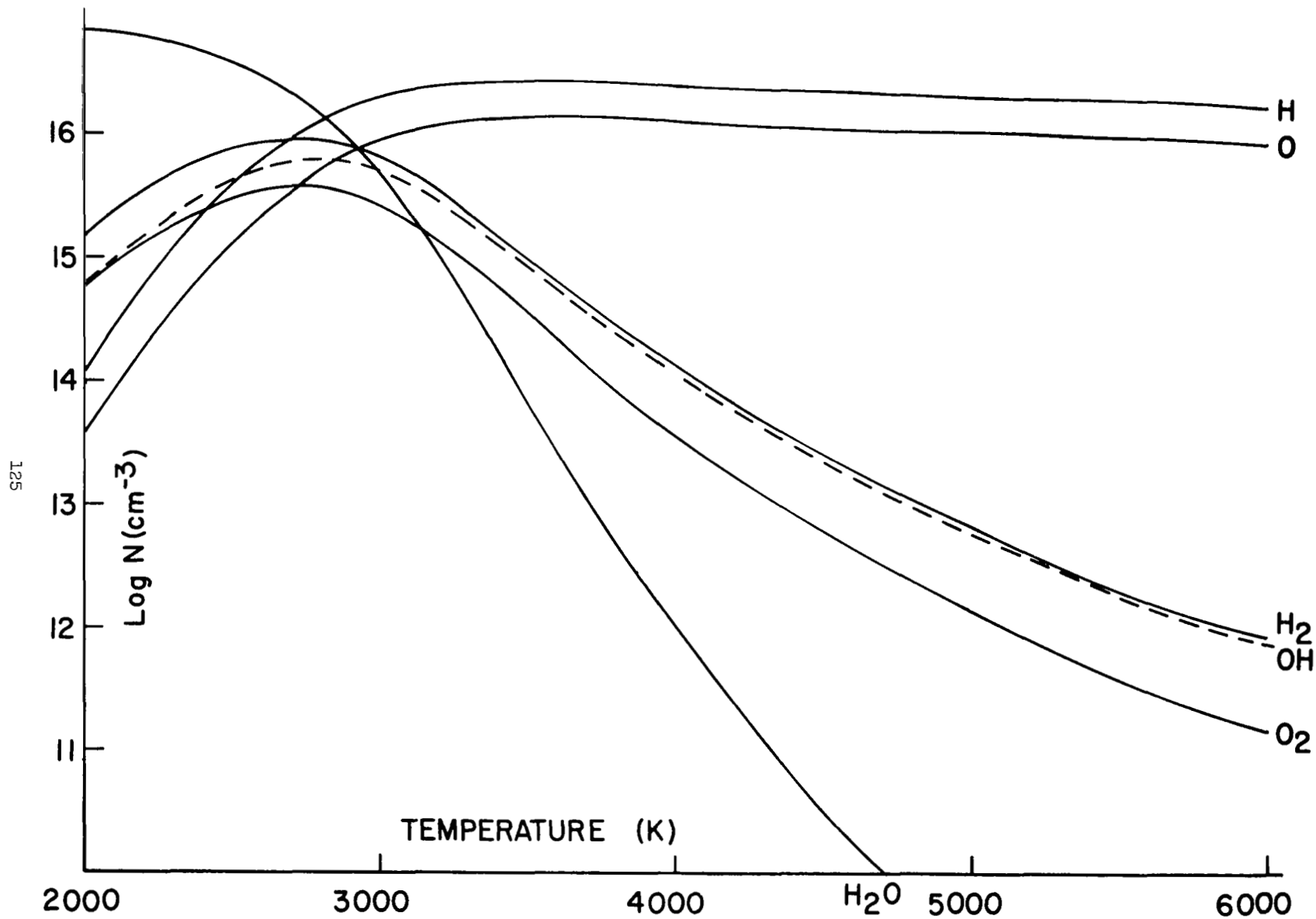
Fig. 4. Calculated equilibrium composition of a water vapor plasma at 0.02 atm pressure.
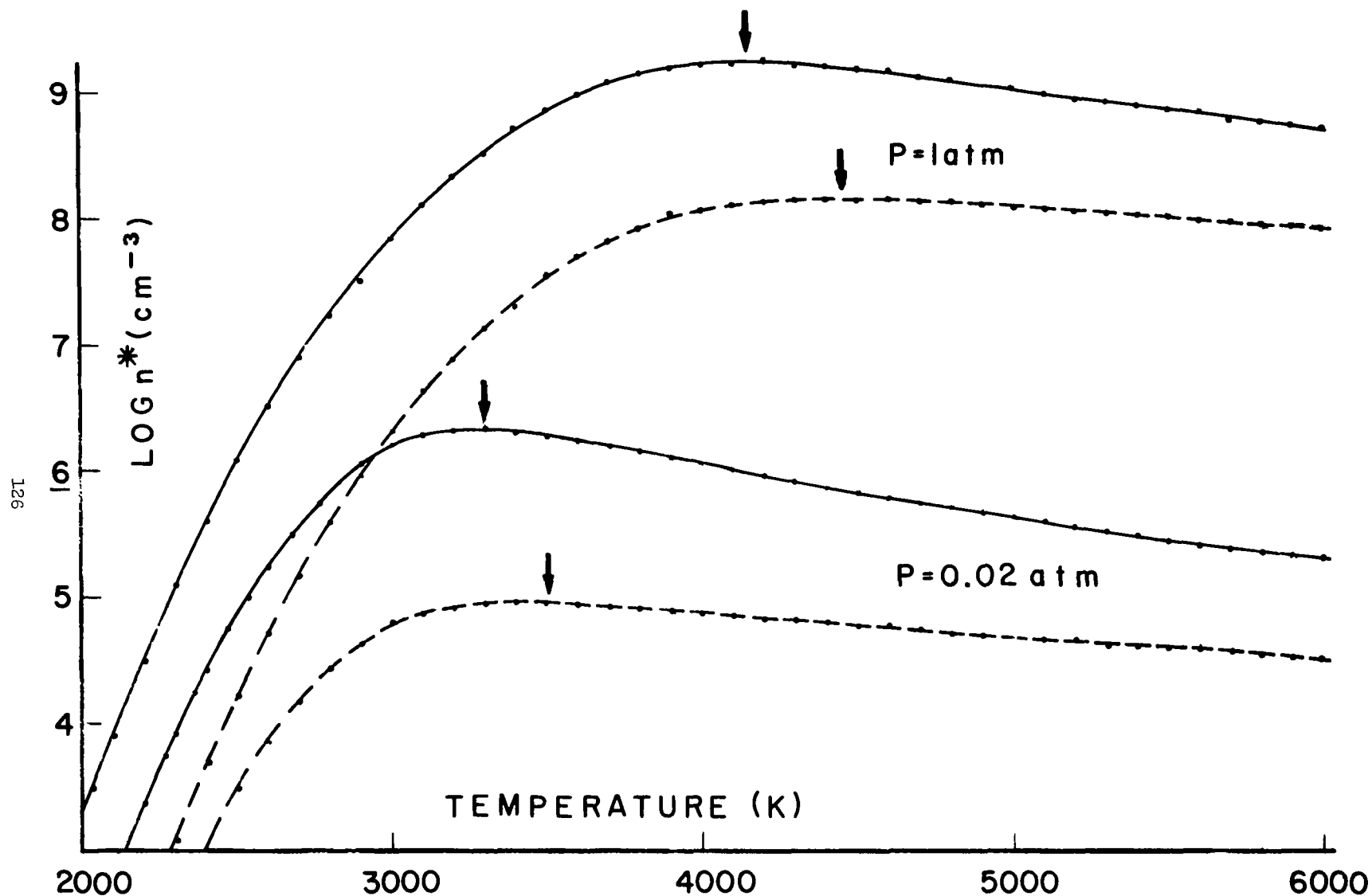
Fig. 5. Equilibrium occupation of the energy states corresponding to the upper energy levels for the P_1-2 (solid line), and the R_1-20 (broken line) transitions of the (0,0) band of OH in a water-vapor plasma at 1 atm and at 0.02 atm pressure. An arrow indicates n*(max) at the normal temperature.
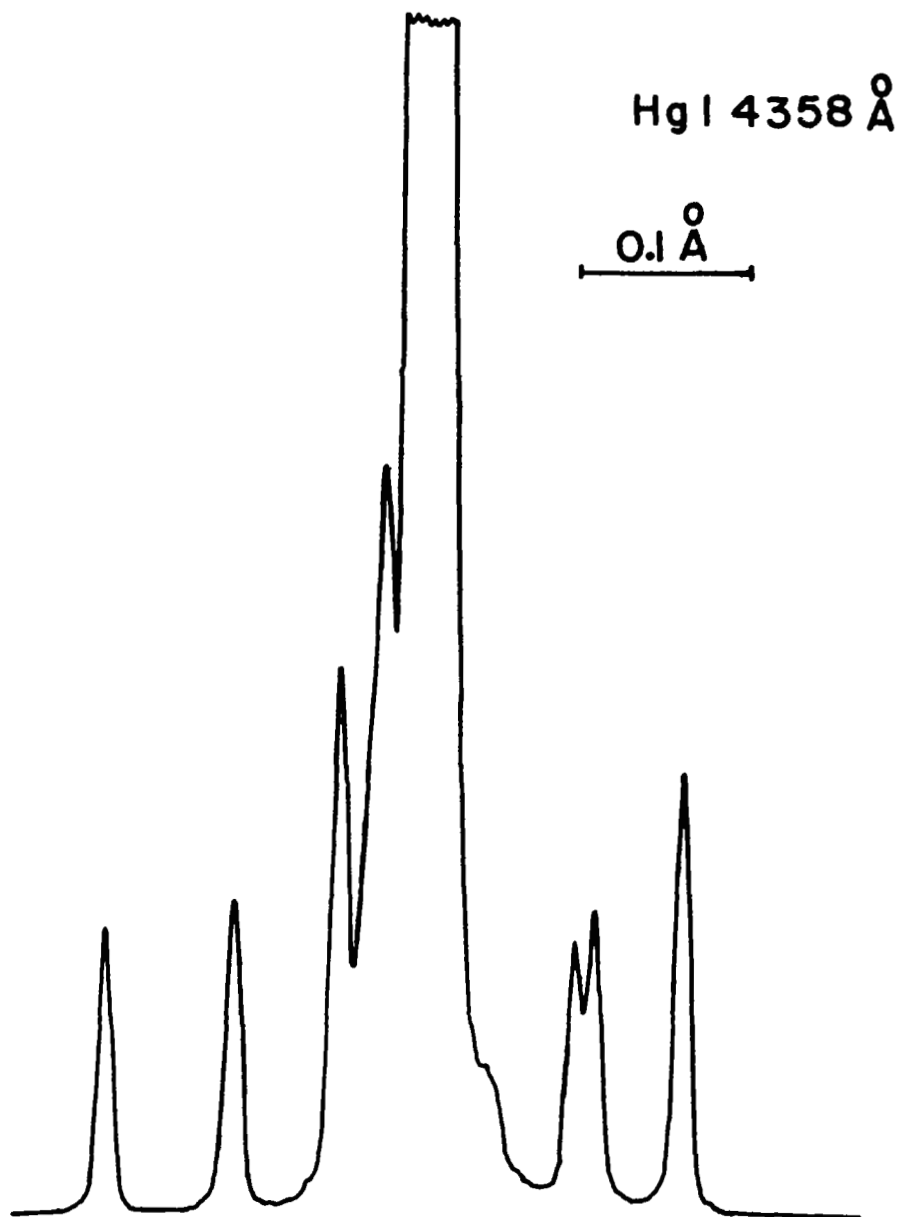
Fig. 6. Photoelectric record of the hyperfine structure of Hg I 4358 Å,
scanned with the five meter spectrometer at a beam aperture of f/80; 4 mm slit-
height, and 0.030 mm slitwidths. The B&L replica grating (600 lines/mm; blazed
at 54°) was used in the 6th grating order at a grating angle of 51°40'.
Source: uncooled low-pressure mercury discharge (germicidal lamp).
Detector: EMI 9558 QA photomultiplier.
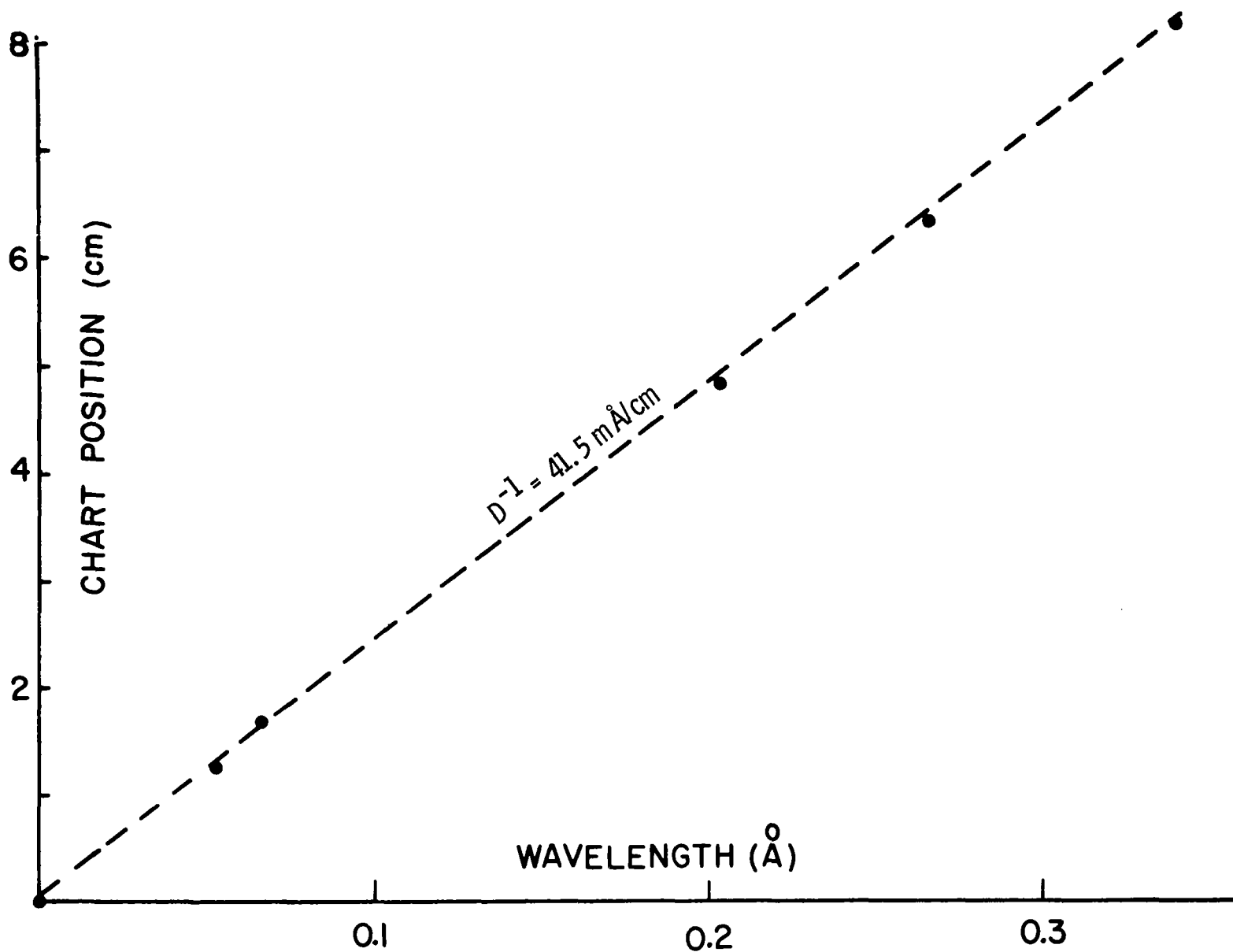
Fig. 7. The measured chart positions of the hyperfine lines in the spectrum of Hg I 4358 Å shown in Fig. 6 have been plotted vs. the increment in wavelength units.
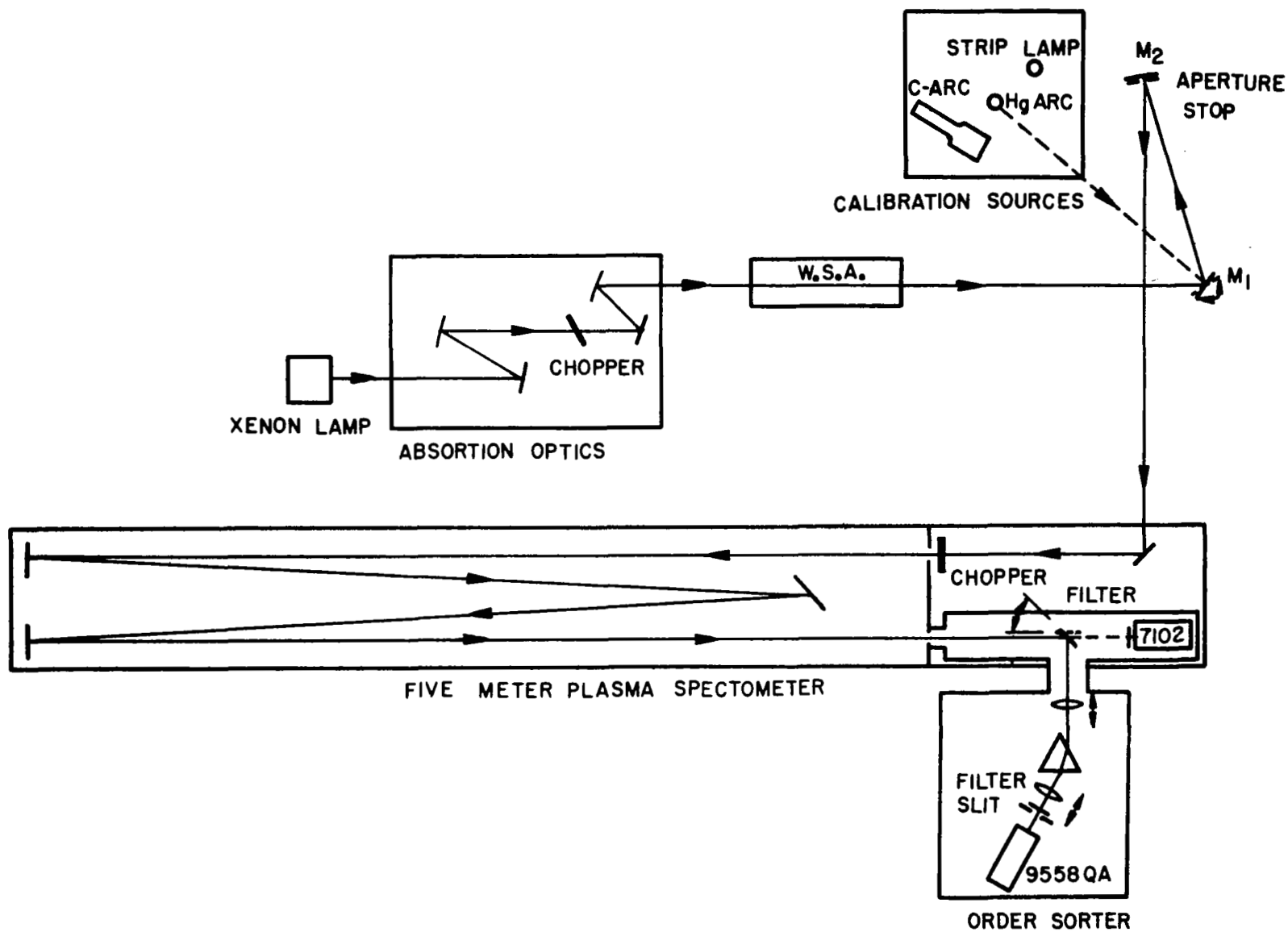
Fig. 8.   Experimental set-up for concurrent emission and absorption measurements of arc plasmas.
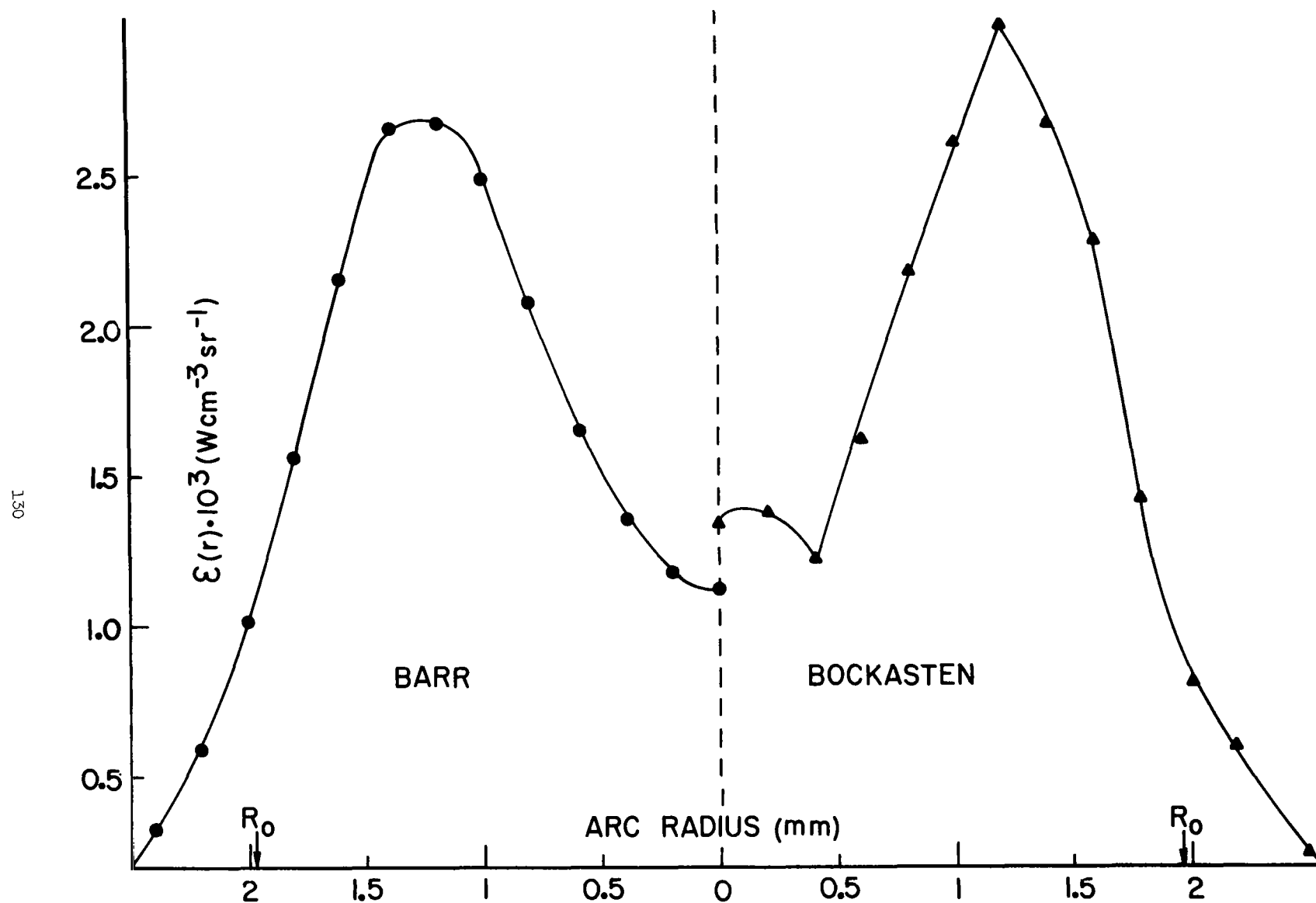
Fig. 9. Results of the Abel inversion of side-on measurements of the R_1-20 (0,0) line of OH. The radial distribution for the emission coefficient has been obtained by Barr's (26) and by Bockasten's (25) method. The source was a water vapor plasma at 50 Amps. and 22 Torr. R_O = radius of arc channel.
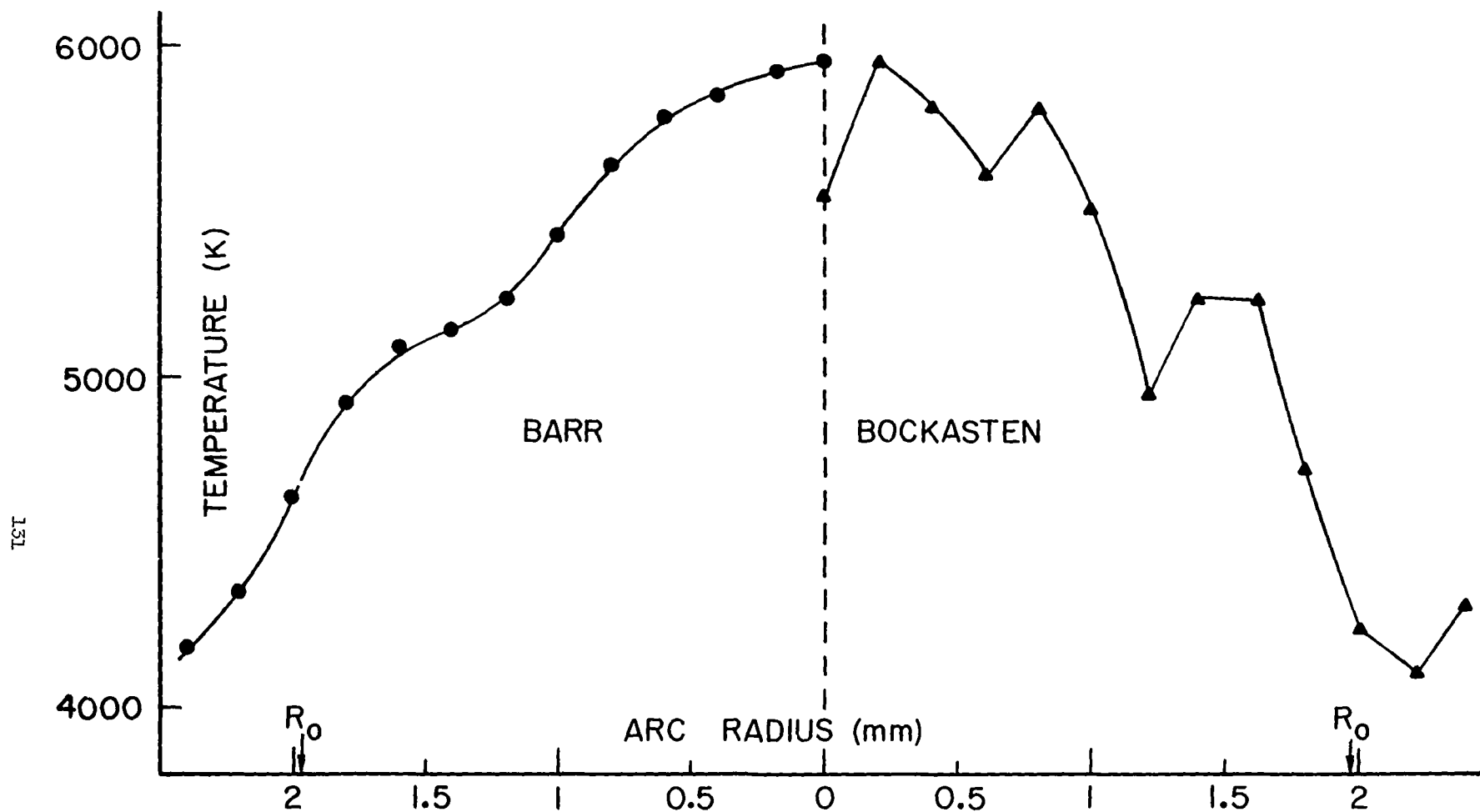
Fig. 10. Radial temperature profile of a water-vapor arc at 50 Amps. and 22 Torr, as derived from the radial distribution of the emission coefficients for the P_1-2 and the R_1-20 lines of the (0,0) band of OH. The profiles obtained from an Abel inversion of the same input data by Barr's and by Bockasten's method are shown to the left and the right, respectively, of the arc center.
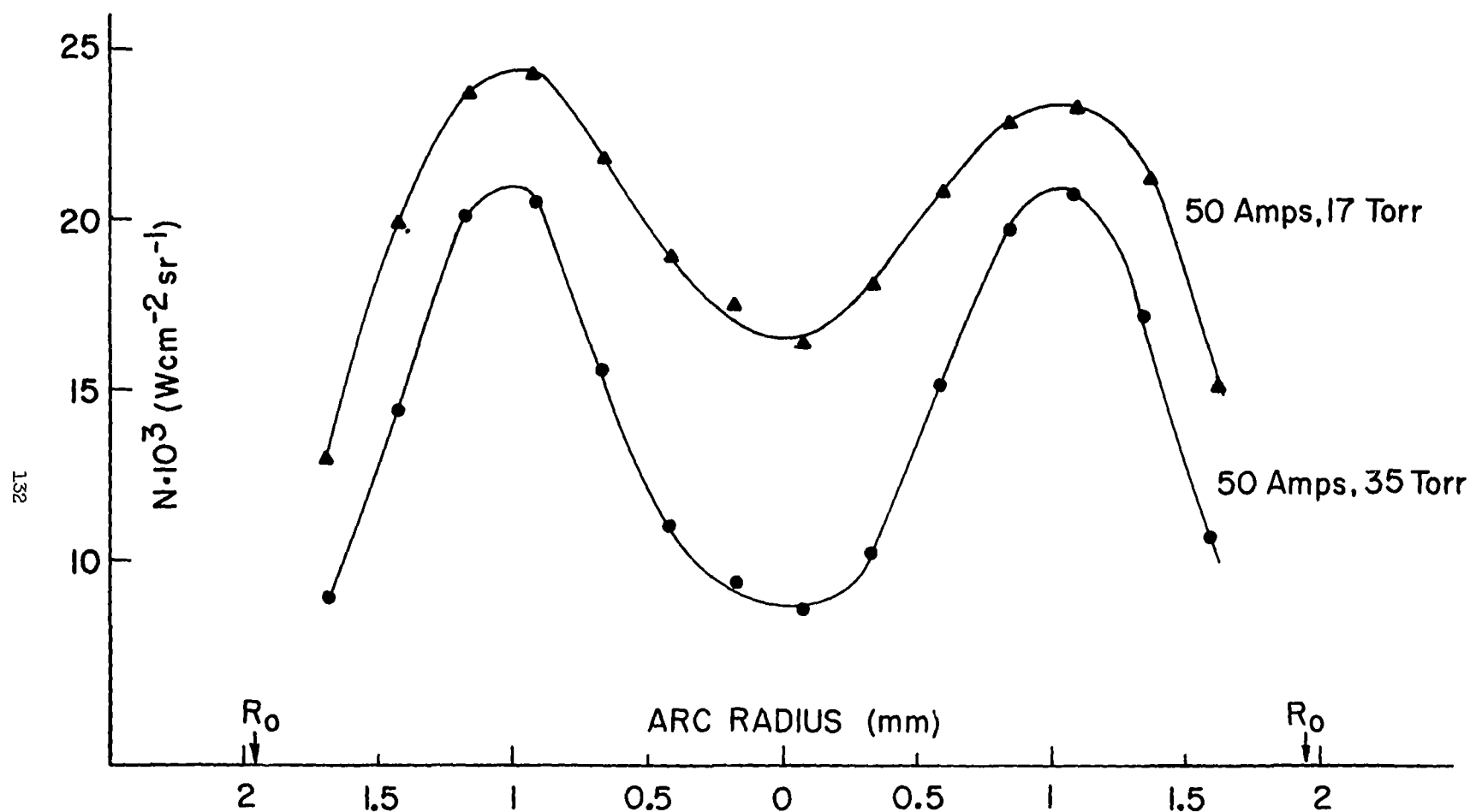
Fig. 11. Local values for the integrated intensity of the P_1-2 (0,0) line, obtained by spatially scanning the arc in the end-on model along its horizontal diameter. The spatial resolution is determined by the dimensions of the entrance slit (0.1 mm wide x 0.25 mm high) and by the f/300 aperture.
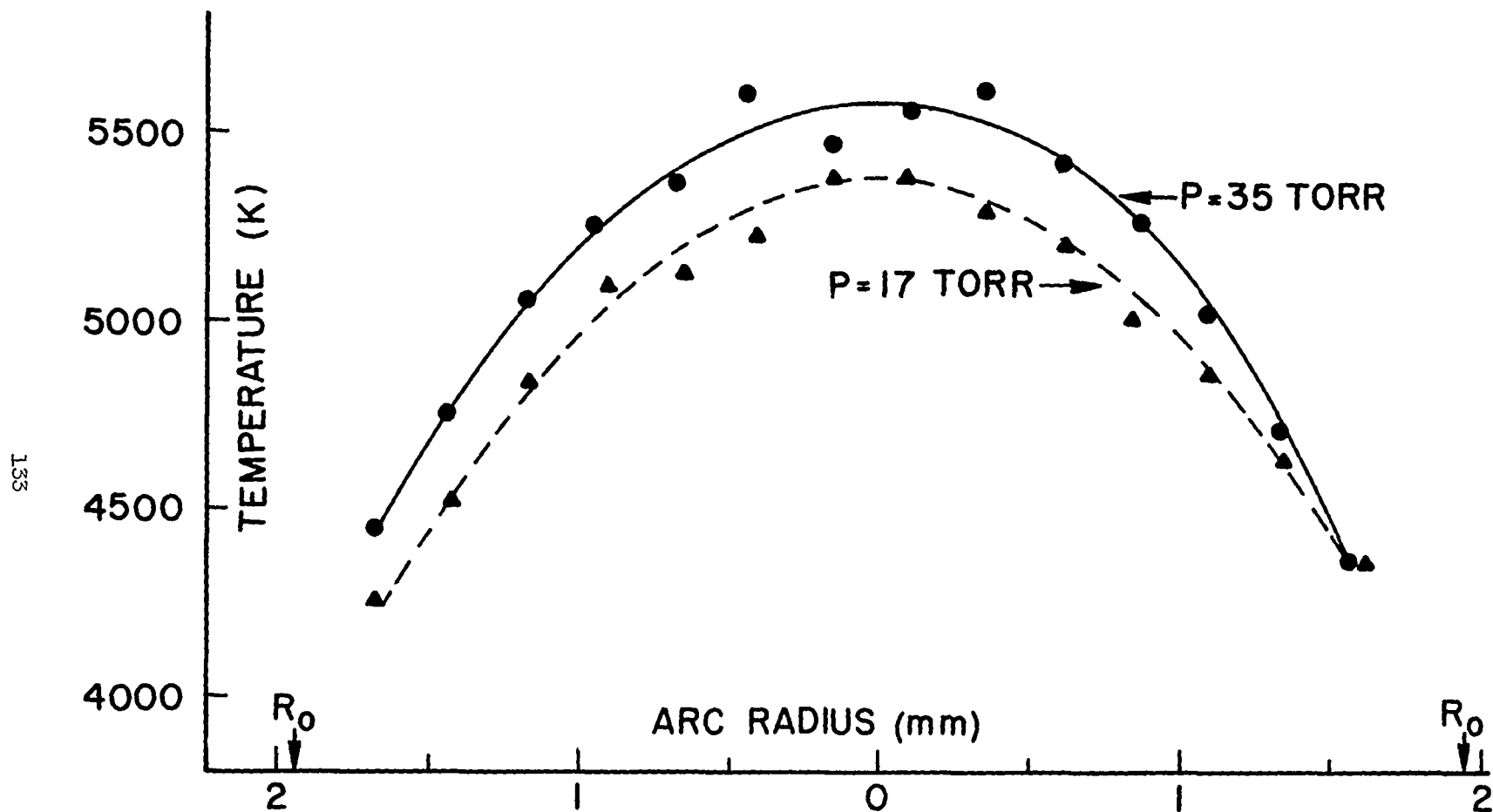
Fig. 12. Radial temperature profile of the 50 Amps. arc in water vapor at 17 and at 35 Torr pressure, as derived from the intensity ratio of the P_1-2 and R_1-20 lines of the (0,0) band of OH. The radial intensity distributions were obtained by spatially scanning the arc in the end-on mode (see Fig. 11).
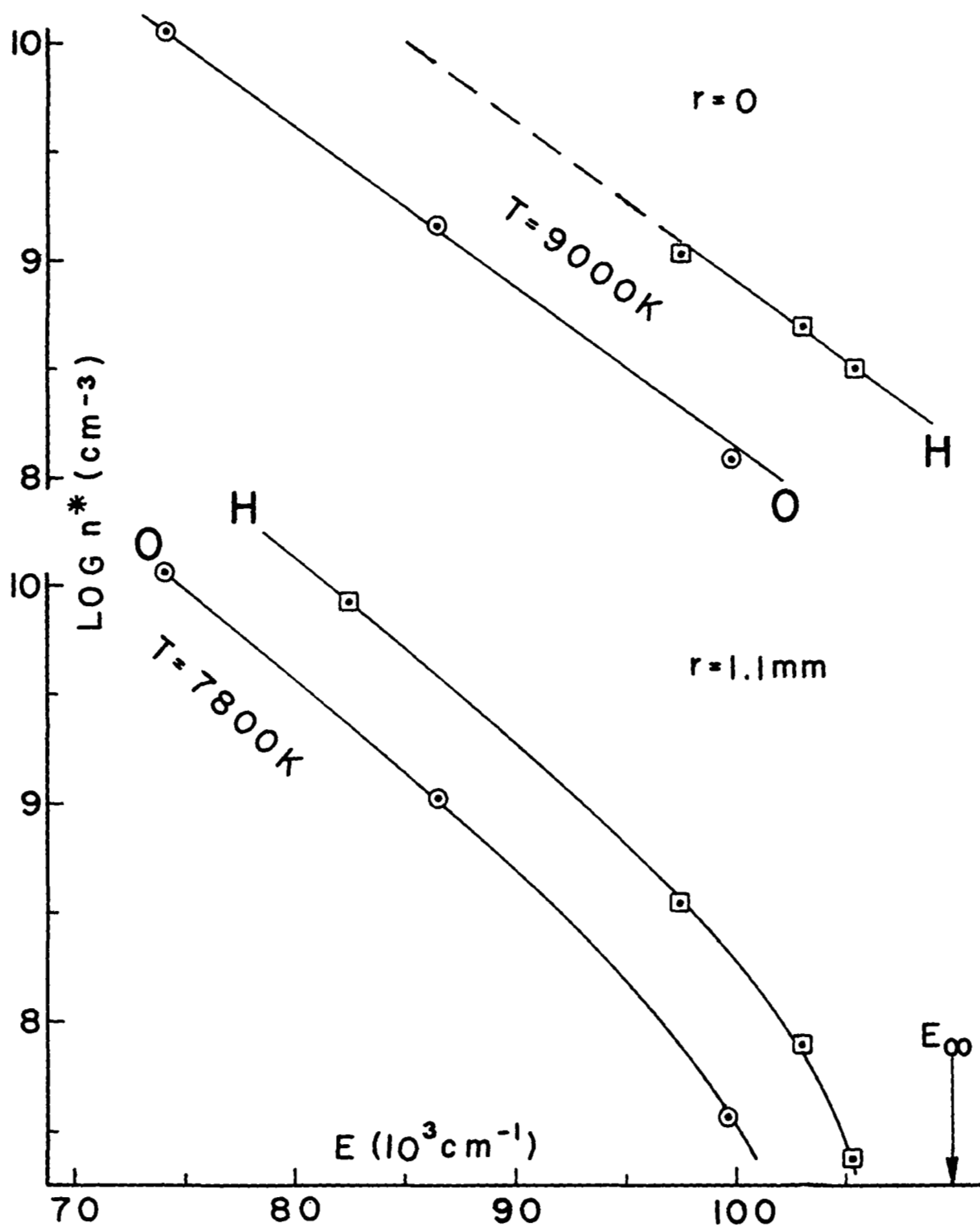
Fig. 13. Measured occupation of energy states of hydrogen and oxygen in the center (r = 0), and at the periphery (r = 1.1 mm) of an arc at atmospheric pressure and 4.1 Amps. The sample gas was argon saturated with water vapor.
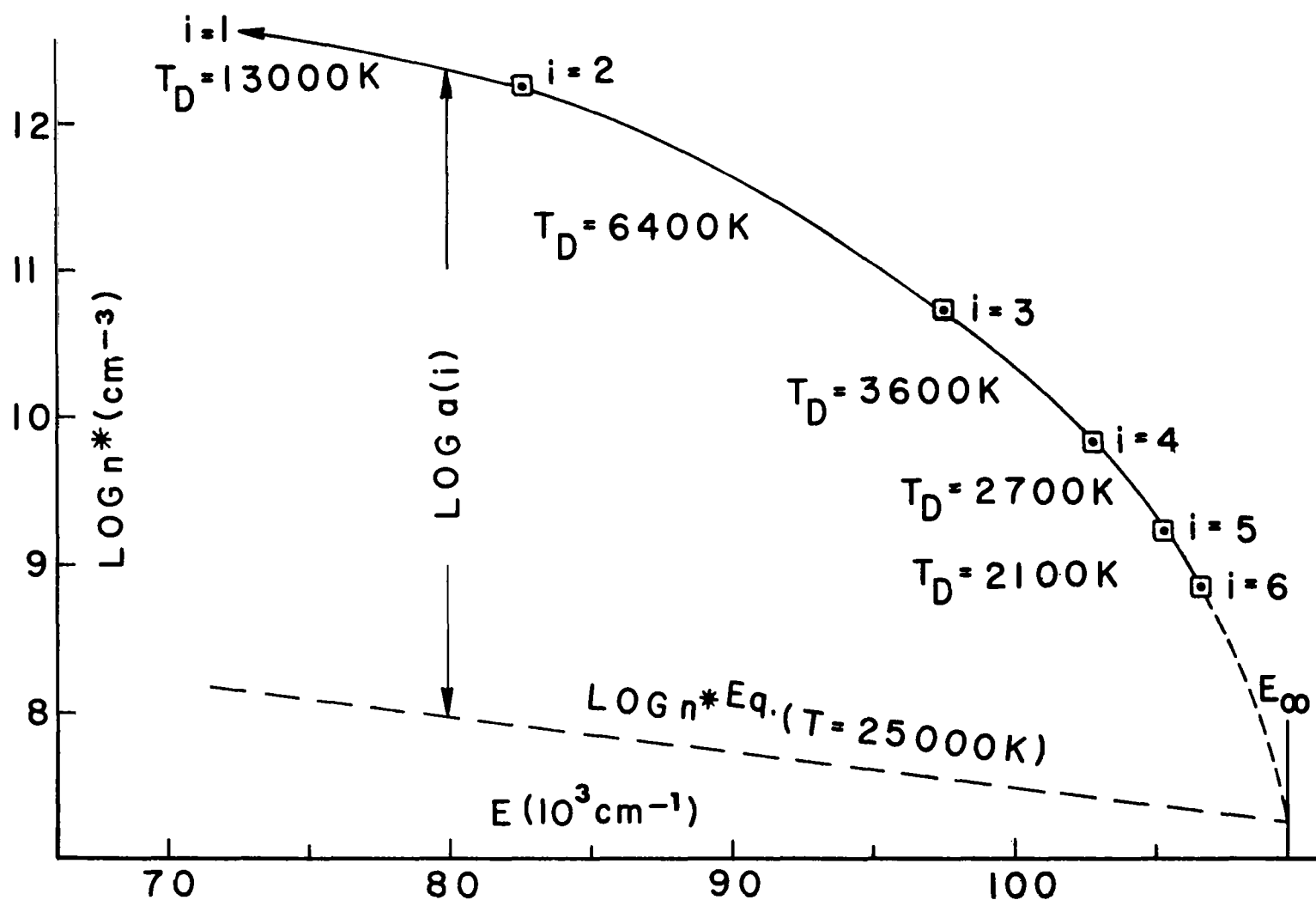
Fig. 14. Occupation of the hydrogen energy states with principal quantum numbers 2 to 6; measured in the center of an arc in water vapor at 22 Torr and 30 Amps. T_D is the distribution temperature for neighboring energy levels. The equilibrium distribution is indicated qualitatively for an electron temperature of 25,000 K.
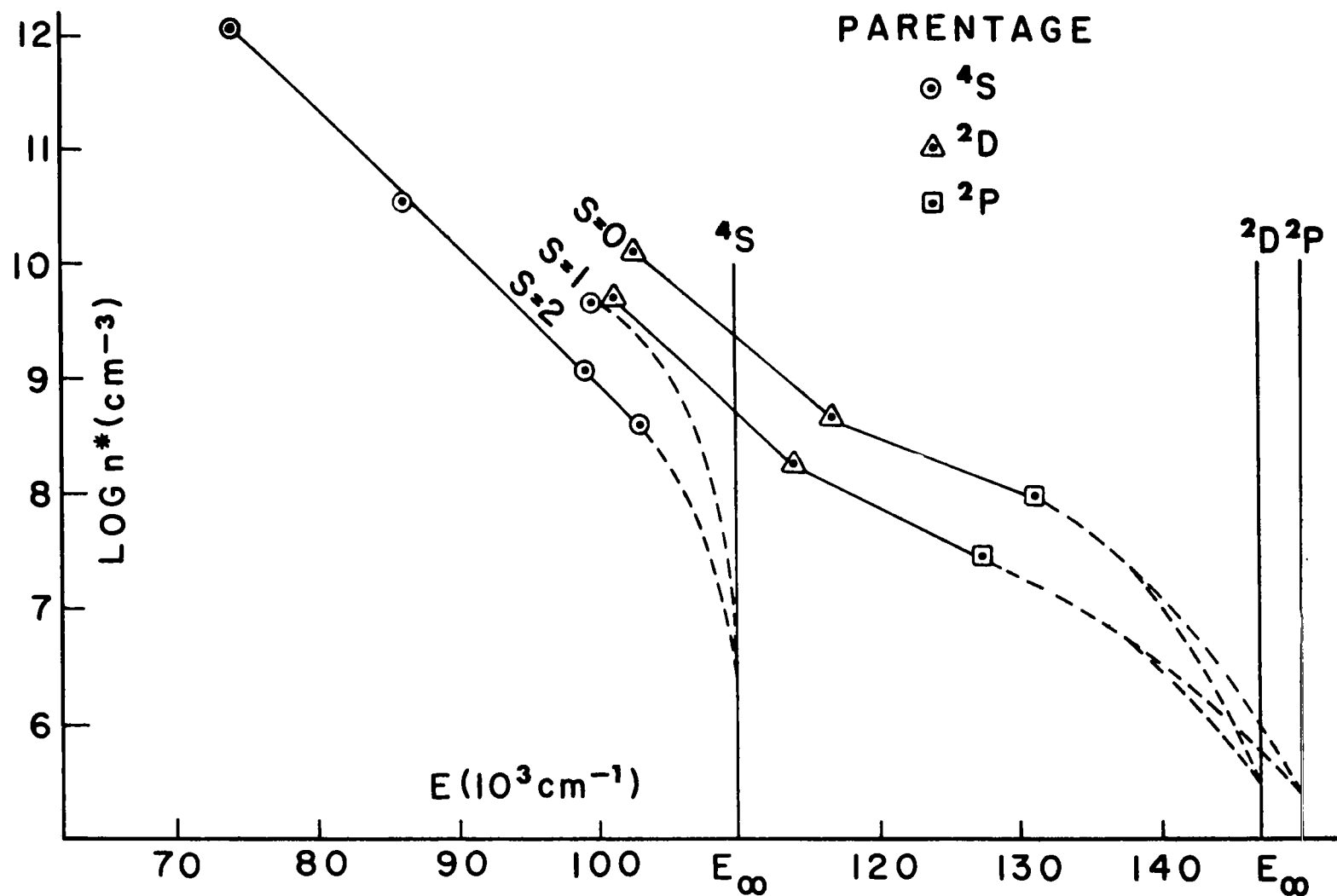
Fig. 15. Occupation of oxygen energy states in the center of an arc in water vapor at 22 Torr and 30 Amps. The predicted population distribution over the higher states corresponding to singlet, triplet, and quintet energy terms is indicated qualitatively by broken line.
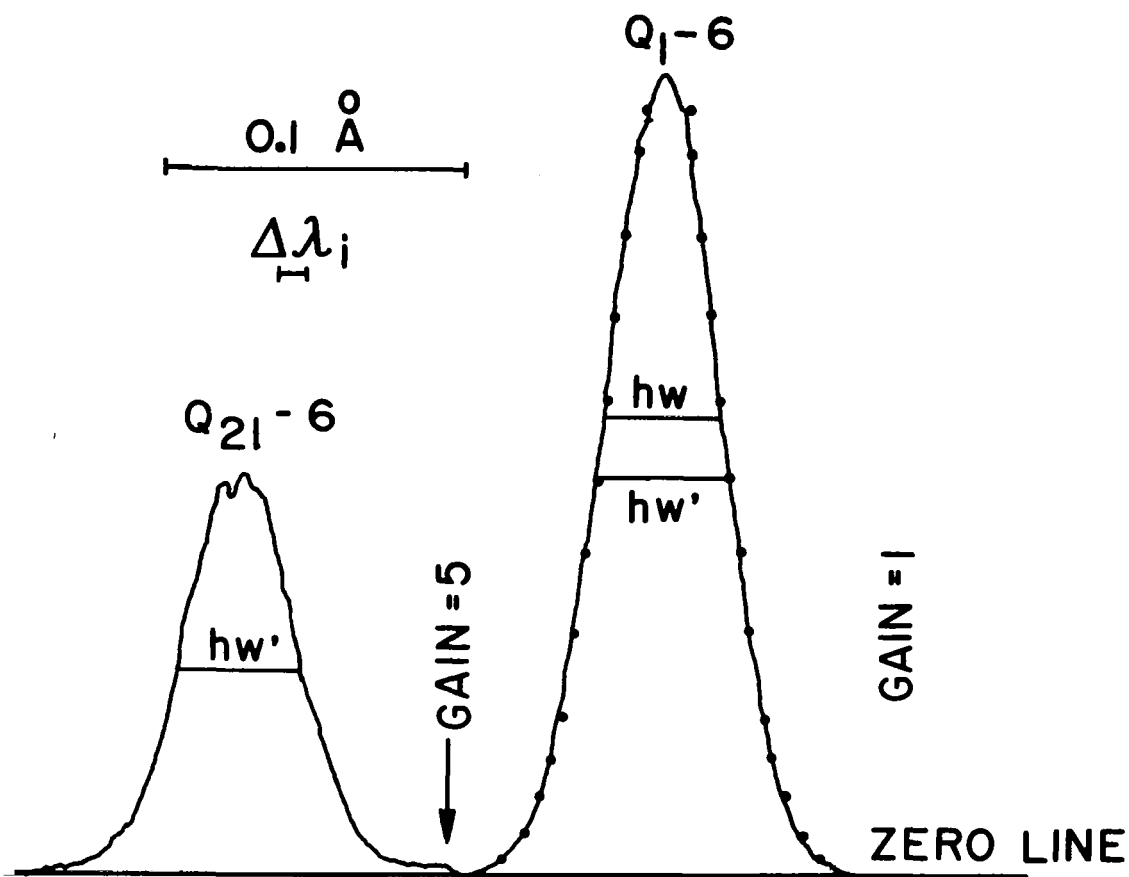
Fig. 16. Photoelectric record of a scan in the 9th grating order of the Q_1-6(0,0) line of OH at 3087 Å and of its satellite, emitted in the end-on mode by an arc in water vapor at 50 Amps. and 20 Torr. The spectrometer was focused on an arc region 1.1 mm off the arc center. Slit widths: 0.025 mm; slit height: 0.25 mm; aperture: f/120.

$\Delta\lambda_i$ is the spectral slit width; hw the half width of the line corrected for self-absorption. The calculated profile for a Gaussian of half width hw' and normalized at the line peak, is indicated by dots.
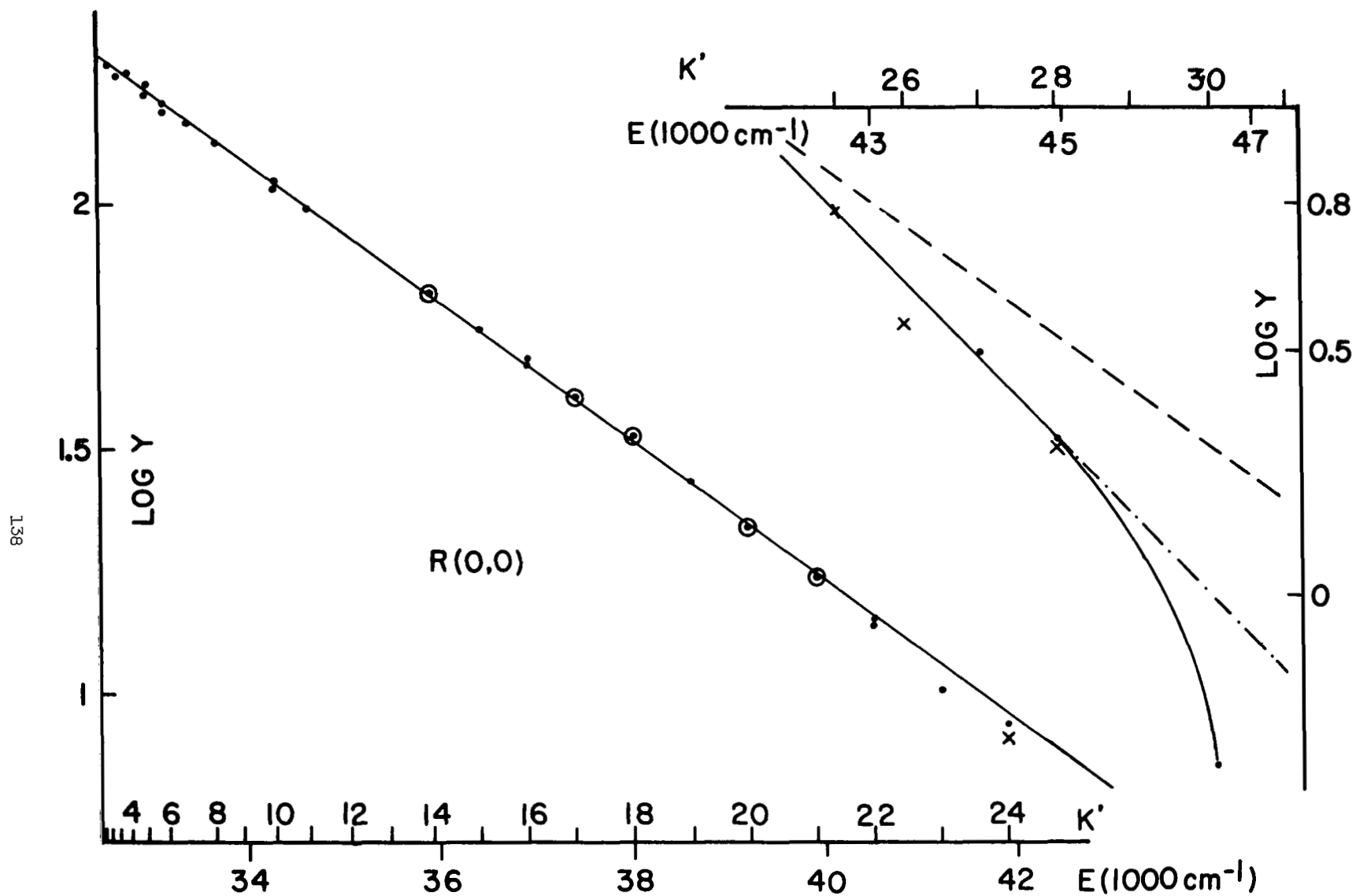
Fig. 17. "Apparent Boltzmann plot" for the R(0,0) branch in run A. Near coincidence for the measured values for the R_1 and R_2 lines is represented by an open circle around the data point. A dot is used for the R_2 lines and a cross for the R_1 lines corresponding to predissociating levels. The extension of the linear portions of the Boltzmann plot is indicated by broken lines. The reduced intensity is denoted by y (see Eq. 6-1).
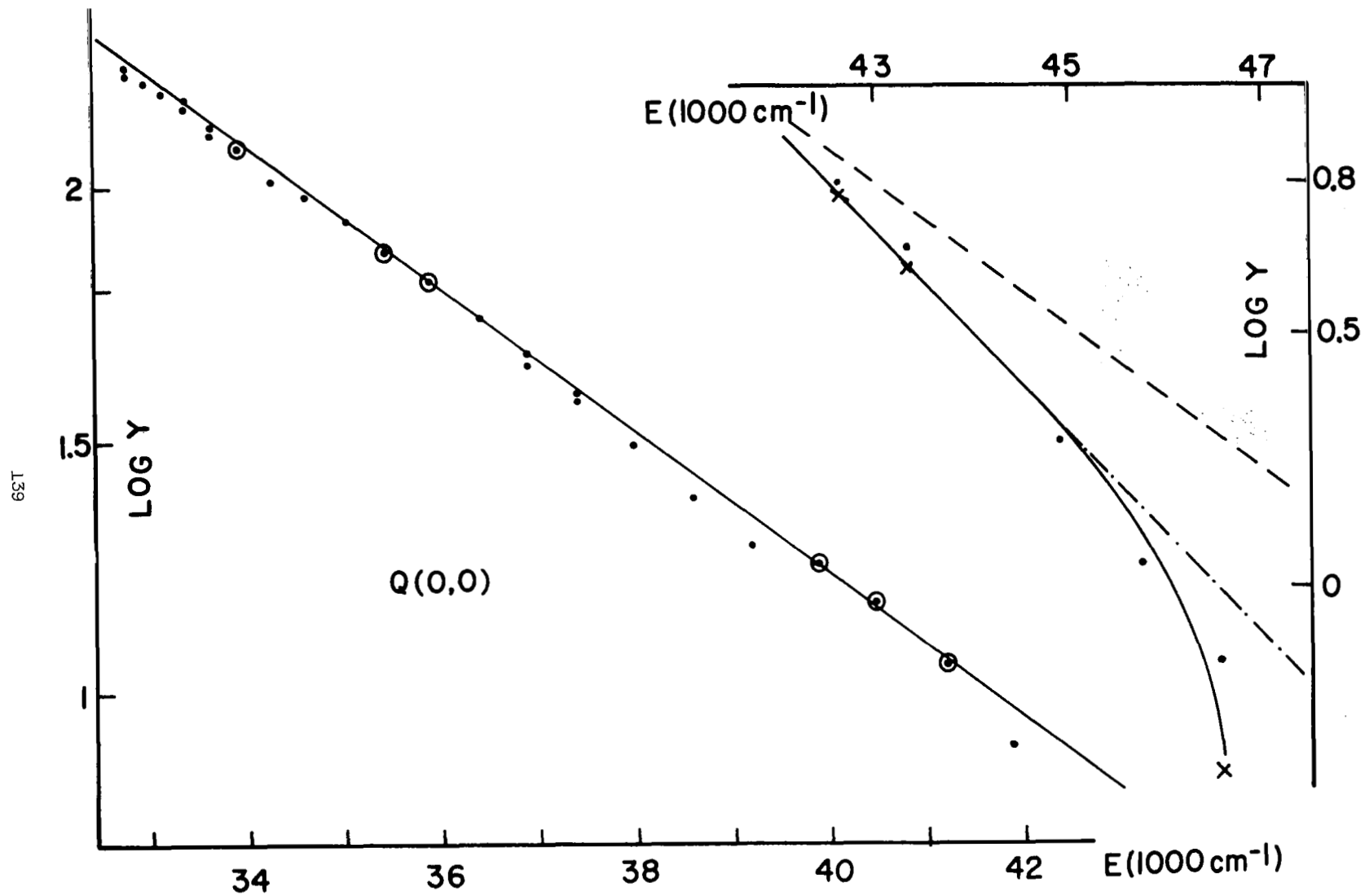
Fig. 18. "Apparent Boltzmann plot" for the Q(0,0) branch in run A. The plot drawn is identical to that for the R(0,0) branch, shown in Fig. 17.
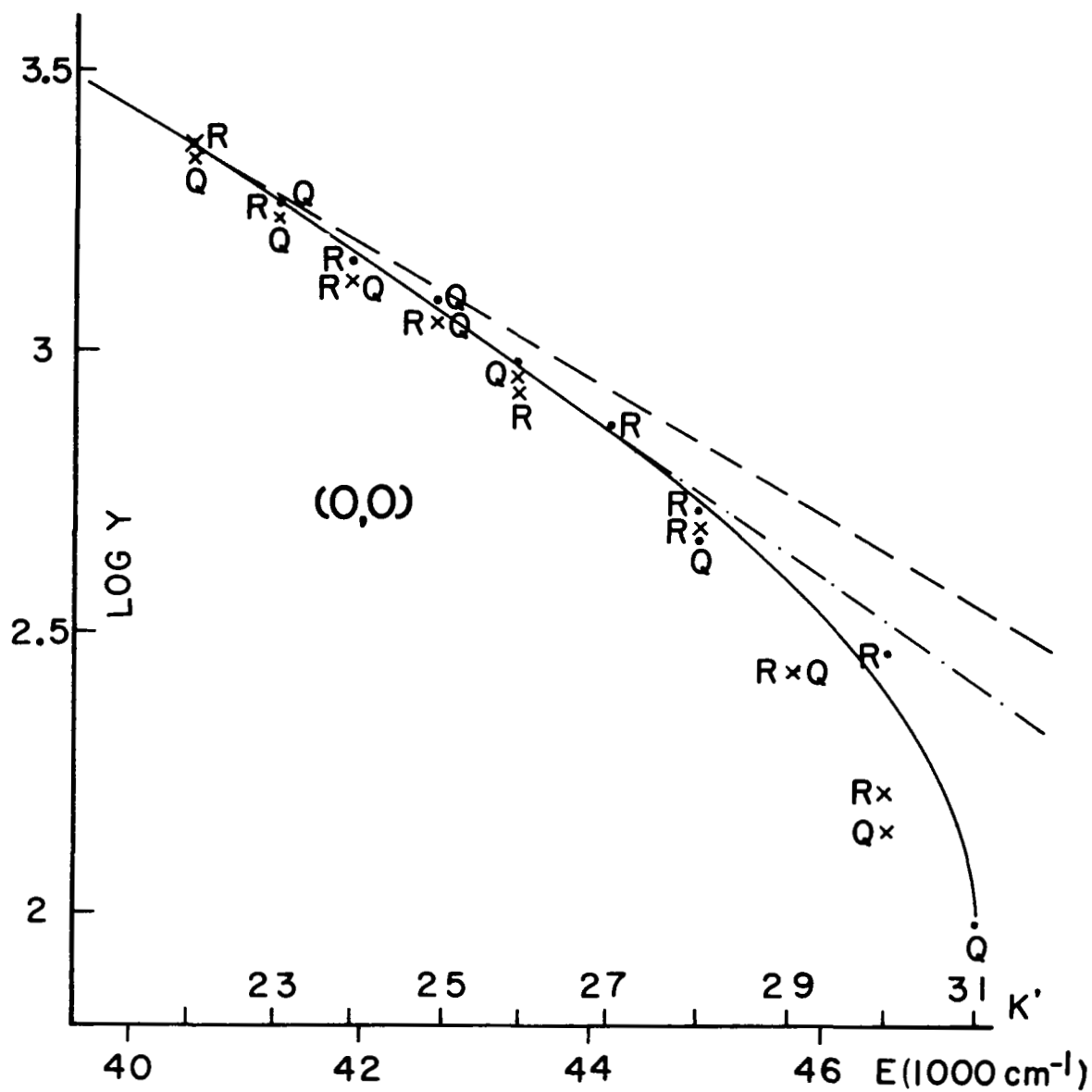
Fig. 19. "Apparent Boltzmann plot" for the higher rotational lines of the (0,0) band in run C-1. A dot is used for lines with an f_2 upper spin state, and a cross for lines with an f_1 upper spin state.
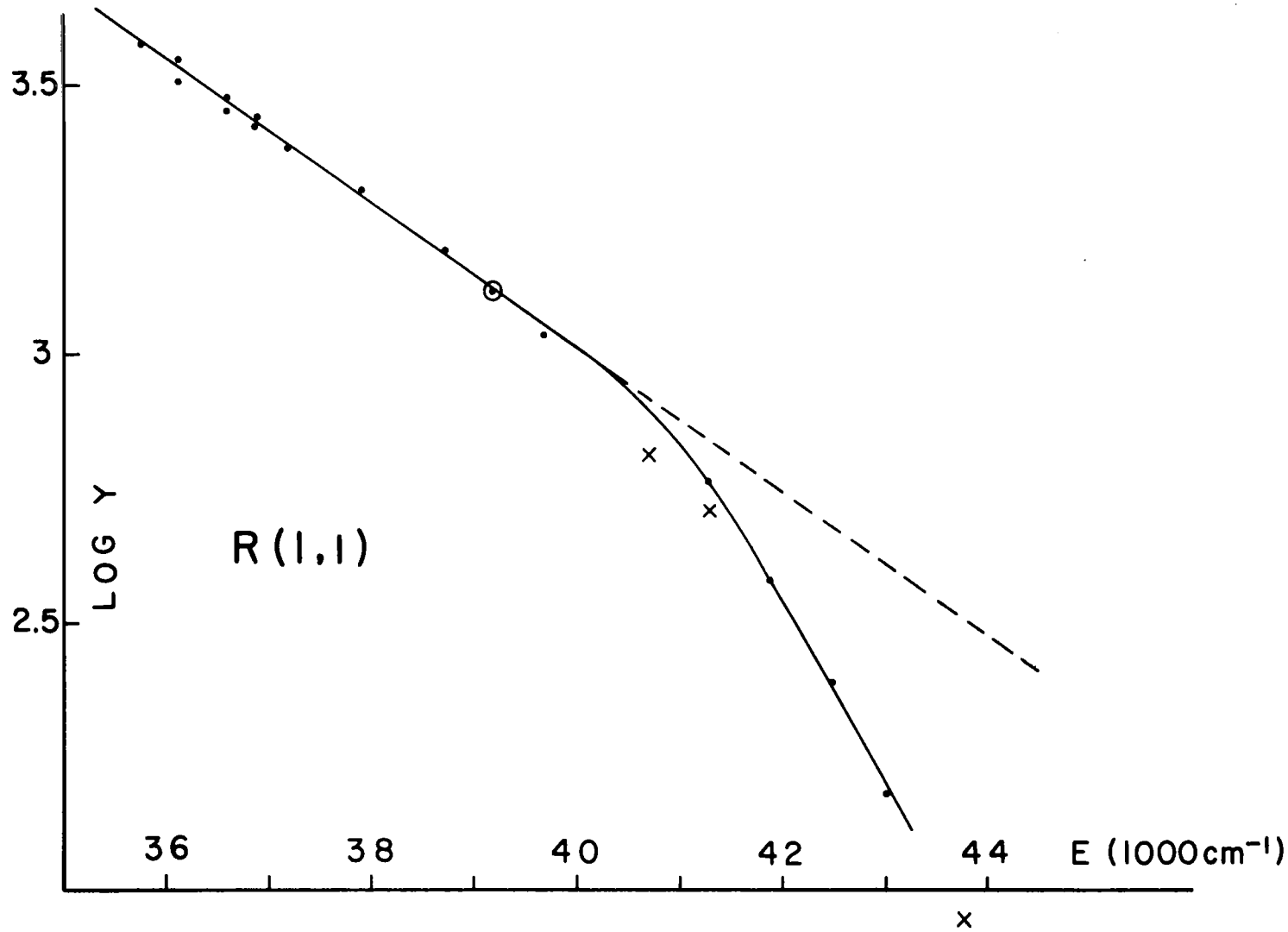
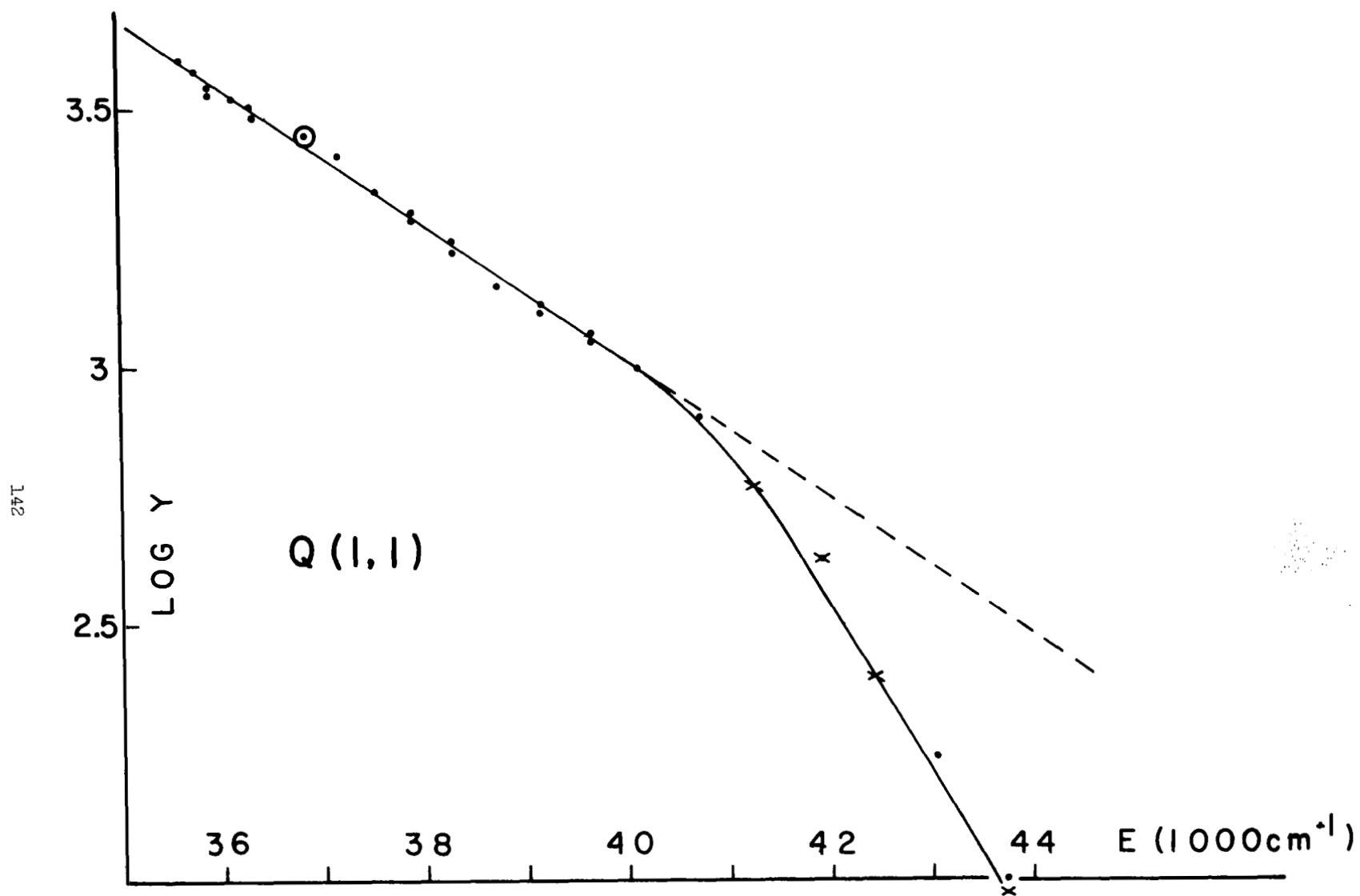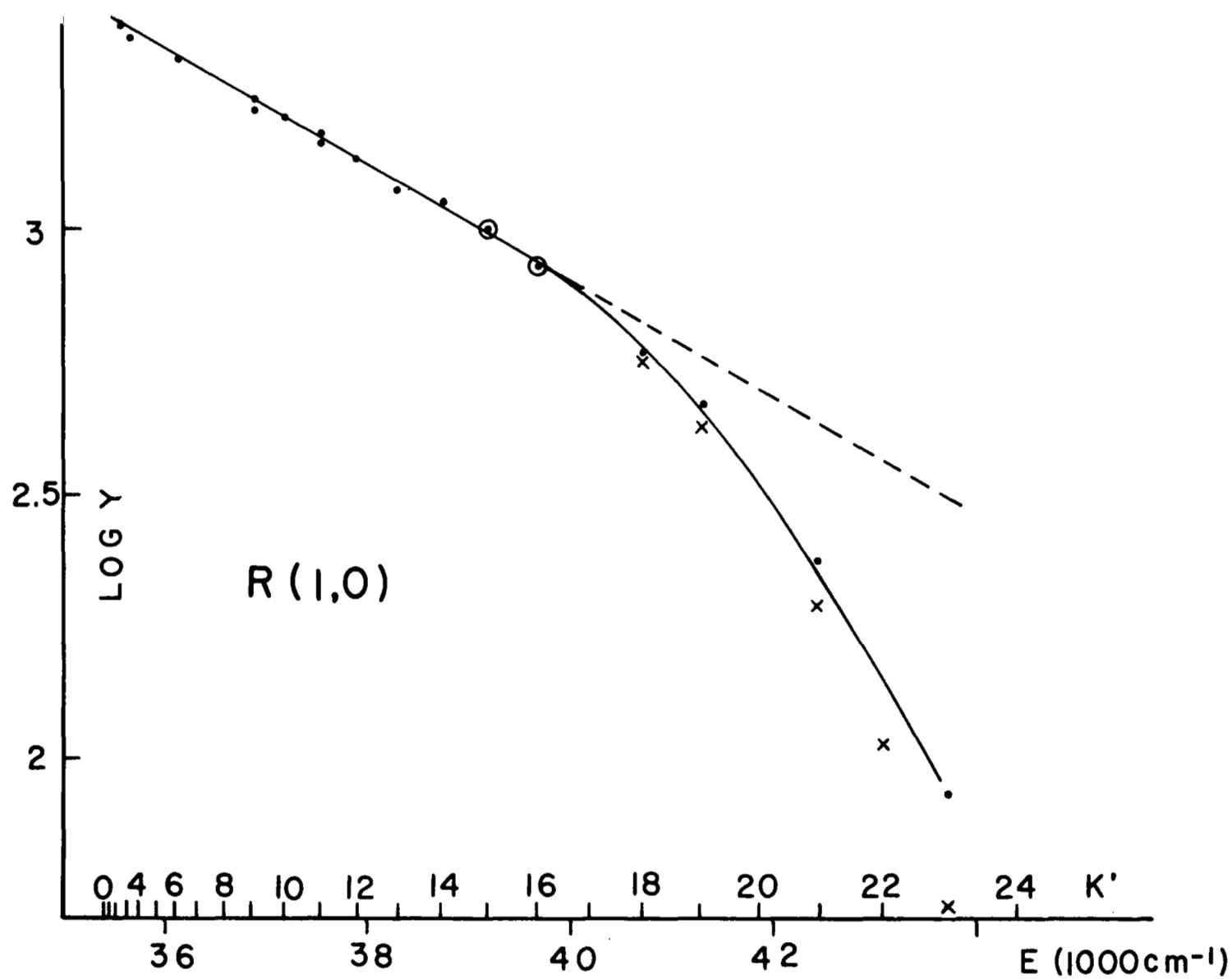Fig. 20. "Apparent Boltzmann plot" for the R(1,1) branch in run C-1.

Fig. 21. "Apparent Boltzmann plot" for the Q(1,1) branch in run C-1. The plot drawn is identical to that for the R(1,1) branch, shown in Fig. 20.

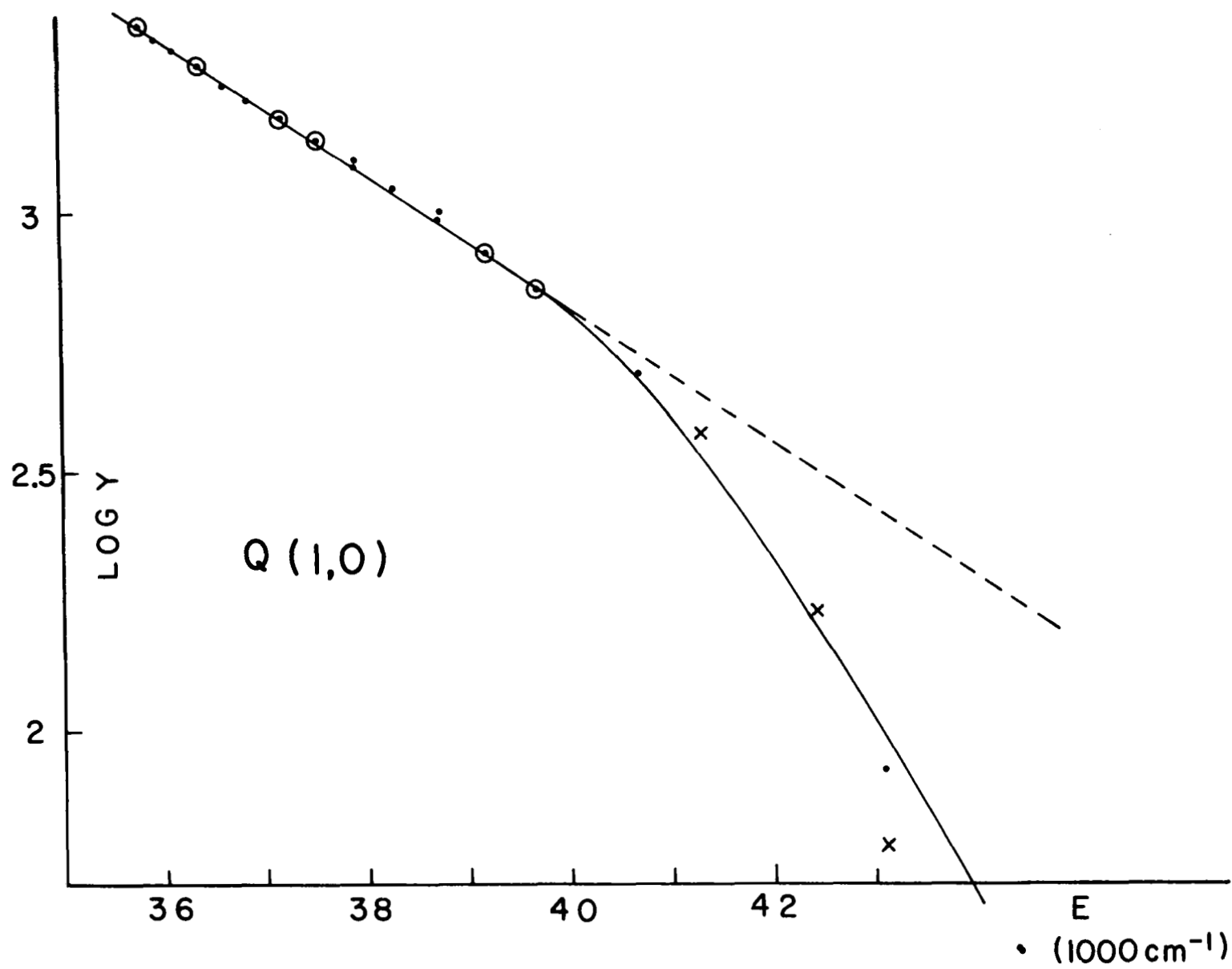Fig. 22. "Apparent Boltzmann plot" for the R(1,0) branch in run B.

Fig. 23.   "Apparent Boltzmann plot" for the Q(1,0) branch in run B.
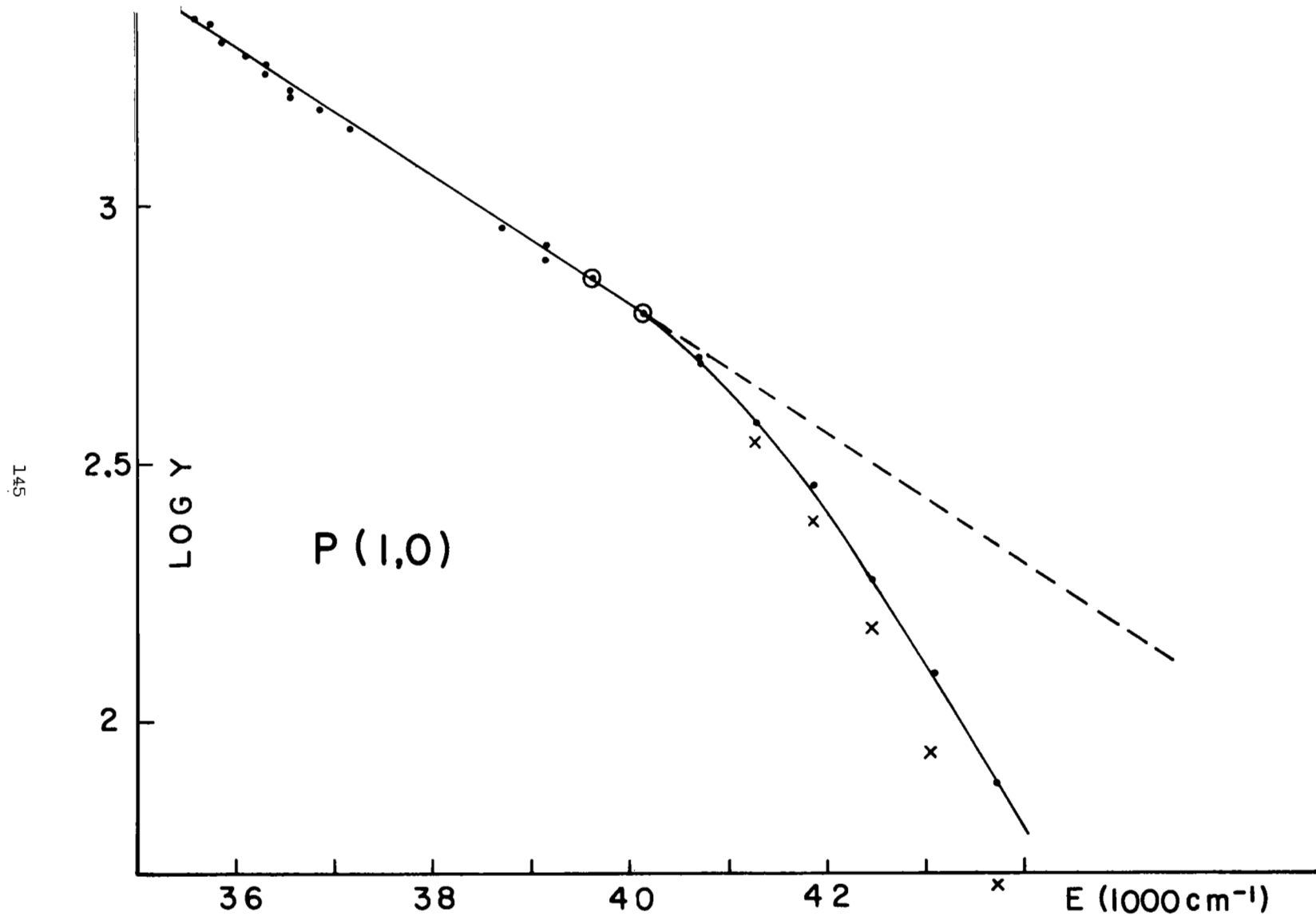
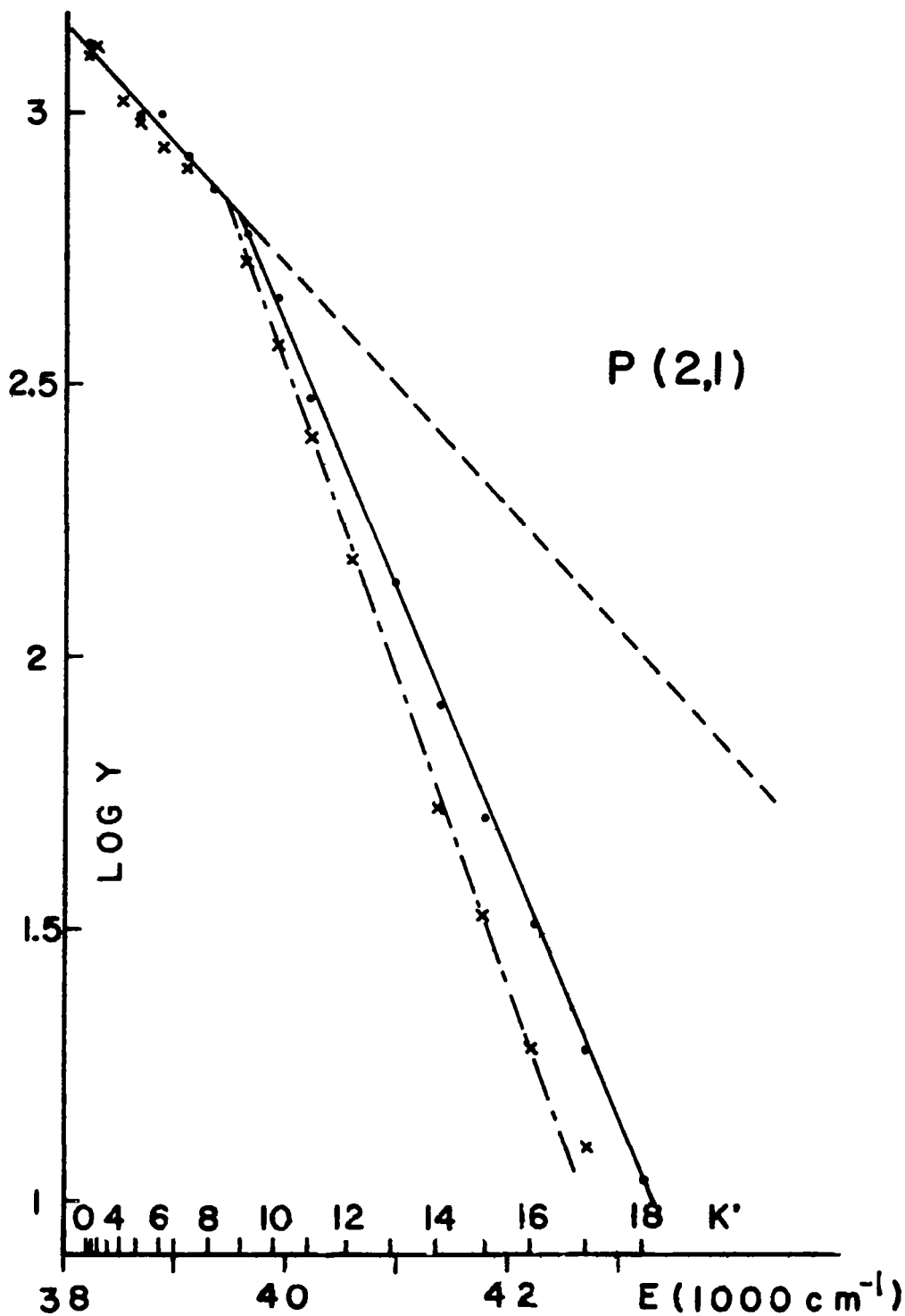Fig. 24. "Apparent Boltzmann plot" for the P(1,0) branch in run B.

Fig. 25. "Apparent Boltzmann plot" for the P(2,1) branch in run B. The splitting of the Boltzmann plots for lines with an f_2 upper spin state (dot), and an f_1 upper spin state (cross) is shown.